

NEI-NO--1067

N09905104

MASTER

Lars Even Torbergsen
Experiments in turbulent pipe flow

RECEIVED

JUL 06 1999

OSTI

DISTRIBUTION OF THIS DOCUMENT IS UNLIMITED
COPIES SALES PROHIBITED

NTNU Trondheim
Norges teknisk-naturvitenskapelige
universitet

Doktor ingeniøravhandling 1998:88
Institutt for mekanikk, termo- og
fluidodynamikk

MTF-rapport 1998:169 (D)



al

Experiments in Turbulent Pipe Flow

Lars Even Torbergsen

October, 1998

DISCLAIMER

**Portions of this document may be illegible
in electronic image products. Images are
produced from the best available original
document.**

Abstract

Experimental results for the mean velocity and turbulence statistics in two straight pipe sections are reported for bulk Reynolds numbers of $Re \epsilon [22.000, 75.000]$. The flow was found consistent with a fully developed state.

Detailed turbulence spectra were obtained for low and moderate R_λ . For the pipe centre line location at $R_\lambda = 112$, a narrow range in the streamwise power spectrum applied to the $-5/3$ inertial subrange. However this range was influenced both by turbulence production and viscous dissipation, and therefore did not reflect a "true" inertial range. The result indicate how the intermediate range between the production and dissipative scales can be misinterpreted as an inertial range for low and moderate R_λ .

To examine the universal behaviour of the inertial range, the inertial scaling of the streamwise power spectrum is compared to the inertial scaling of the second order longitudinal velocity structure function, which relate directly by a Fourier transform. Increasing agreement between the Kolmogorov constant C_K and the second order structure function scaling constant C_2 was observed with increasing R_λ . The result indicate that a "true" inertial range requires several decades of separation between the energy containing and dissipative scales.

A method for examining spectral anisotropy is reported, and applied to turbulence spectra in fully developed pipe flow. In particular the axisymmetric behaviour of the spectra was studied. The results indicate that the spectral redistribution from the streamwise to the two lateral spectra, goes primarily to the circumferential component.

Experimental results are reported for an axisymmetric contraction of a fully developed pipe flow. A rapid redistribution of energy between the normal stresses was found as the flow accelerated. The redistribution was attributed to the effects of secondary production and pressure-strain interaction. The Reynolds stress tensor developed towards a state of "rod-like" turbulence. The flow acceleration mainly affected the largest turbulent scales.

Acknowledgments

This work has been performed at Department of Applied Mechanics, Thermo- and Fluid Dynamics at the Norwegian University of Science and Technology.

I am most grateful to my supervisor Professor Per-Åge Krogstad for his honest interest and valuable criticism, throughout this work. I express my sincerest thanks.

I thank John Krogstad, Arnt Kolstad and Øyvind Andersen for their technical assistance in preparing the experimental equipment.

Finally I express my sincerest thoughts to the very special Lene Mostue for her patience and support during these years.

This thesis will be submitted for the degree:

Doktor Ingeniør (Dr.Ing.)

at the Norwegian University of Science and Technology.

Trondheim, October 1998
Lars Even Torbergsen

Contents

1	Introduction	1
2	Experimental Details and Data Analysis	5
2.1	Pipe Rig Facility I	5
2.2	Pipe Rig Facility II	5
2.3	Experimental Techniques	7
2.3.1	Static pressure	8
2.3.2	Hot-wire anemometry	8
2.3.3	Data acquisition	9
2.3.4	Fast Fourier transform	10
2.4	Experimental procedure	12
3	Theory and Flow Documentation	15
3.1	Coordinate System	15
3.2	Transport Equations	16
3.3	Universality and Scaling	19
3.4	Verification of Fully Developed Pipe Flow	23
3.4.1	Global parameters	24
3.4.2	Homogeneity	26
3.4.3	Mean velocity	27
3.4.4	Reynolds stress tensor	31
3.4.5	Turbulent scales	38
3.4.6	Turbulent kinetic energy budget	38
3.5	Conclusion	42
4	Fourier Representation	45
4.1	Power Spectrum	45
4.1.1	The spectral energy cascade	49

4.1.2	Measured streamwise power spectra	52
4.1.3	Measured lateral power spectra	55
4.2	Cross-correlation Spectrum	60
4.2.1	Measured cross-correlation spectra	61
4.3	Dissipation Spectrum	63
4.3.1	Dissipation rate from inertial subrange	65
4.4	Remarks on the Inertial Range Scaling	67
4.5	Conclusion	67
5	Structure functions	69
5.1	Structure Function Inertial Range Scaling	70
5.2	Measured Structure Functions	74
5.2.1	Experimental details	74
5.2.2	Dissipation rate	75
5.2.3	Second and third order longitudinal structure functions	78
5.3	Conclusions	81
6	Invariant Analysis	85
6.1	Time Mean Invariants	85
6.1.1	Invariants in fully developed pipe flow	90
6.2	Spectral Invariant Analysis	94
6.2.1	Solution algorithm	98
6.3	Measured Spectral Invariants	99
6.3.1	Elements of the spectral anisotropy tensor	100
6.3.2	Spectral axisymmetry	102
6.4	Conclusions	105
7	Quadrant Analysis	107
7.1	Quadrant Decomposition	108
7.2	Results	109
7.2.1	Decomposition of the $\bar{u}_x \bar{u}_r$ -signal	109
7.2.2	Conditional average of \bar{u}_x^2 and \bar{u}_r^2	110
7.3	Conclusions	110
8	Axisymmetric Contraction	117
8.1	Motivation	117
8.2	Contraction Design	118
8.3	Experimental Details	120

CONTENTS

ix

8.4	Results	122
8.4.1	Mean velocity	122
8.4.2	Second order moments	123
8.5	Turbulence Production	128
8.6	Dissipation Rate	131
8.7	Turbulence Spectra	131
8.8	Invariants	133
8.9	Spectral Axisymmetry	138
8.10	Implications on turbulence modelling	140
8.11	Conclusions	141
9	Summary	143

List of symbols

Latin letters

Symbol	Quantity	Si-unit
A	Parameter describing axisymmetry	-
A_{ij}	Advection term in the RST equations	m^2/s^3
B	Constant in "law of the wall"	-
b	Blockage factor	-
b_{ij}	Reynolds stress anisotropy tensor	-
$c_{ij}(k_x)$	Spectral anisotropy tensor	m
C_K	Kolmogorov Constant	-
C_n	Scaling constant for n'th order structure function	-
D	Internal pipe diameter	m
D_{ij}	Diffusion term in the RST equations	m^2/s^3
$E_{ij}(n)$	Power spectral density in frequency space	m^2/s
$E_{ij}(k_l)$	Power spectral density in wave number space	m^3/s^2
F	Anisotropy function	-
f	Darcys friction factor	-
H	Threshold for quadrant decomposition	-
I_i	Invariants of the Reynolds stress anisotropy tensor b_{ij}	-
\hat{I}_i	Invariants of the Spectral anisotropy tensor c_{ij}	m^2
k	Turbulent kinetic energy	m^2/s^2
k_x	Streamwise component of the wave number vector	$1/m$
l	Length	m
L	Pipe length	m
n_c	Filter frequency	Hz
n_s	Sampling frequency	Hz
P	Static pressure	Pa
P_{ij}	Production term in the RST equations	m^2/s^3
Q	Flow rate	m^3/s
$Q_{ij}(\mathbf{r})$	Space correlation tensor	m^2/s^2
r	Radial coordinate in cylinder coordinates	m
R	Pipe radius	m
$R_{ij}(\tau)$	Time correlation tensor	m^2/s^2
Re	Reynolds number based on bulk velocity and pipe diameter	-
R_λ	Turbulent Reynolds number	-
s_w	Cross-wire spacing	m
t	Time	s
T	Temperature	$^{\circ}C$
$\tilde{U}_i(t)$	Instantaneous velocity in x_i system	m/s
U_i	Mean velocity in x_i system	m/s
u^*	Friction velocity	m/s
\bar{U}	Integrated mean velocity	m/s
U_o	Pipe Bulk velocity	m/s

	cont.	
$u_i(t)$	Fluctuating velocity in x_i system	m/s
x	Streamwise direction in cylinder and Cartesian coordinates	m
y	Wall normal direction in Cartesian coordinates	m
z	Transverse direction in Cartesian coordinates	m

Greek letters

δ_{ij}	Kronecker delta	
ε	Dissipation rate of turbulent kinetic energy	m^2/s^3
ε_{ij}	Dissipation term in the RST equations	m^2/s^3
η	Kolmogorov length scale	m
κ	Von Karman constant	-
λ	Taylor length scale	m
Π_{ij}	Pressure-strain term in the RST equations	m^2/s^3
ρ	Fluid density	kg/m^3
τ_{ij}	Reynolds stress tensor	m^2/s^2
v	Kolmogorov velocity scale	m/s
ν	Kinematic viscosity	m^2/s
θ	Circumferencial direction in cylinder coordinates	$1/rad.$
ξ	Area ratio of contraction	-

Superscript

- + Scaling with friction velocity (u^*) and/or kinematic viscosity (ν)
- ' Root Mean Square
- o Isotropic

Subscript

a	Ambient
axi	Axisymmetric
c	Filter
cl	Centre line
i, j, k	General index equal 1,2 or 3
iso	Isotropic
s	Sampling
w	Hot wire

Chapter 1

Introduction

The majority of fluid flows involve turbulence, and smooth laminar flow rarely occurs in practical flow situations.

This thesis focuses on turbulent pipe flow, which has been, and still is, an important subject in turbulence research. In addition to the academic approach, turbulent pipe flow is certainly of great importance in a number of industrial flow problems, such as processing industry or oil and gas transportation.

Today the difficulty of obtaining reliable numerical results for turbulent flows in general, still remains a big challenge. During the past decades, great efforts have been put into development of turbulence models, and a number of different approaches are today available within this field. This variety clearly pictures the difficulty of obtaining universal models, which are applicable to various complex flow situations. The importance of experimental turbulence research, in obtaining direct applicable results and a solid basis for the numerical approach, is still indisputable.

Fully developed pipe flow has been examined by a number of researchers during the past decades, and a large amount of experimental data is available, at least for low and moderate Reynolds number. The applied definitions of "fully developed pipe flow" are rather vague. For an engineer, estimating the pressure loss in straight pipe sections, the main concern is the linearity of the streamwise pressure distribution. The international standard (ISO-5167)[28] for fluid flow measurements by means of pressure differential devices, also puts a restriction on the mean velocity distribution, but still with no comments on turbulence quantities. For the purpose of turbulence research, the definition of fully developed pipe flow also require streamwise homogeneity of

the turbulence statistics. Higher order terms, such as triple correlations, are believed to stabilize more slowly than e.g. the second order moments. Thus it is clear that the different definitions of fully developed pipe flow, lead to different lengths of straight pipe. As early as 1921, Latzko (see Hinze [25]) suggested an empirical relation for the distance from the pipe entrance to the position where the velocity distribution could be described by a 1/7-power law. The classical pipe flow data by Nikuradse (1932) and Laufer (1963) were for a long time believed to be representative for the fully developed situation. These results were obtained with pipe lengths of 40 and 50 diameters, respectively. More recent results by Klein [33], has indicated that these pipe lengths may not be sufficient for a situation of fully developed flow. Lawn [36] reported an experimental study of the dissipation rate in fully developed pipe flow, from experimental results obtained in a 60 diameter fetch of straight pipe.

The majority of classical results are obtained with long hot-wires, that is larger than $O(1\text{mm})$ [14], which yields poor small scale resolution. It is clear however that this does not affect turbulence characteristics dominated by large scales, such as second order moments in the wall-remote region. However, the small scale behaviour, such as the high wave number range of the turbulence spectra, may be attenuated by spatial averaging. Recent results have been reported by Browne and Dinkelacker [14]. These results were obtained in a 100 – 200 diameter pipe rig, for low and moderate Reynolds numbers ($Re \in [8.500, 66.400]$), using a partially etched 3\mu m diameter single hot-wire. These results mainly focused on higher order statistics, and fluctuating wall pressure. Developments in Laser Doppler Velocimetry (LDV) and Particle Image Velocimetry (PIV) have offered new approaches to experimental turbulence research. Near wall fully developed pipe flow measurements, using LDV, have been reported by Durst et al. [19], emphasizing the near wall behaviour of the second order moments. Similar LDV experiments have been reported by Fontaine and Dutch [22] and Toonder and Nieuwstadt [61]. Westerweel et.al [63] reported Digital PIV results for fully developed pipe flow, though at a low Reynolds number($Re = 5300$). This experiment was designed to match the direct numerical simulation (DNS) results of Eggels et al.[21]. This comparison emphasizes interesting aspects of DNS, since the two methods have the same property of producing spatial resolved data, which is crucial e.g. for determining coherent structures. A detailed comparison of pipe flow and channel flow, based on DNS and experiments, was reported by Eggels et al. [21]. The results suggested a difference between the two flow

configurations near the wall, due to the transverse curvature of the pipe wall.

The intention of this work is not to reproduce another set of data for fully developed pipe flow, but rather use some of its characteristic properties to examine some of the classical theories of turbulence. Fully developed pipe flow possesses certain properties which are convenient for the academic approach to the phenomenon of turbulence. First of all it is one of the simplest and most easily controlled turbulent flows. The flow is homogeneous in circumferential and streamwise direction. The direct relation between the linear pressure drop along the pipe and the wall friction, gives an accurate prediction of the friction velocity, which is an essential scaling parameter. The presence of a low turbulence intensity core region, yields high experimental accuracy, and validity of the classical Taylor hypothesis. The confinement of the flow is axisymmetric, which produces a singular axisymmetric point on the symmetry line. A number of theories have been developed for axisymmetric turbulence, which can be considered as an intermediate between homogeneous and isotropic turbulence. Axisymmetric turbulence is the simplest form of turbulence including anisotropy, which implies non-zero pressure-strain interaction. As early as 1946 Batchelor[8] developed a theory for the kinematics of axisymmetric turbulence, followed by Chandreskhar in 1950 [16]. More recent analytical work was reported by George and Hussain [24], presenting an axisymmetric form of the dissipation rate tensor. Ould-Rouis et al. [47] reported an even simpler axisymmetric approximation to the dissipation rate tensor, and deduced an axisymmetric expression for the 3rd order structure functions. The most recent analytical results have been put forward by Lindborg[38]. Of great importance is Lindborg's deduction of the pressure-strain terms, which are presented in a form within reach of the experimentalist.

The following chapter presents the experimental facilities, and the data collection procedure. Chapter three includes some basic concepts, notation, and documentation of the fully developed flow conditions. Experiments are performed in two pipe rigs with different pipe diameters. Some of the characteristic properties, describing the fully developed situation, are presented. Chapter four deals with turbulence spectra, with special focus on the inertial range scaling, and separation of energy containing and dissipative scales, as a function of Reynolds number. In a number of flow situations, the power spectra appear to follow a $-5/3$ inertial range, even for low and moderate turbulent Reynolds number. It is unclear if this is a "true" inertial range, fulfilling the requirements posed by Kolmogorov, or just a range which ap-

pears similar. The power spectra and the second order structure functions are directly related through a Fourier transform. This suggests that there should be a universal relation between the scaling constants and exponents in the inertial scales of the power spectrum and the corresponding structure function, which is discussed in chapter five. Chapter six presents the classical invariant analysis of Lumley [42], applied to the Reynolds stress anisotropy tensor for fully developed pipe flow. A new invariant analysis has been derived for the spectral invariant tensor, to examine deviation from isotropy and axisymmetry at different turbulent scales. Chapter seven deals with coherent structures in fully developed pipe flow, which has been previously examined by e.g. Sabot and Comte-Bellot [52]. This analysis is based on quadrant decomposition of the instantaneous turbulent shear-stress signal. In chapter eight, an axisymmetric contraction is mounted at the end of a straight pipe. The purpose of this experiment was to examine the effect of an axisymmetric contraction of an initially fully developed pipe flow. It is a renowned phenomenon of turbulence that a mean streamwise acceleration reduces the streamwise normal stress, in favour of the two cross-stream components. Changes to the Reynolds stress tensor and the turbulence spectra are reported.

Chapter 2

Experimental Details and Data Analysis

2.1 Pipe Rig Facility I

Pipe rig I, shown in Fig. 2.1 (a), consists of a 92 mm diameter (D) smooth aluminium pipe, where the flow is driven by an upstream mounted fan. Vortices generated by the fan are eliminated in a grid-honeycomb section, followed by a [5 : 1] area ratio reduction to the pipe. The pressure difference ΔP across the contraction gives an accurate reference to the flow rate $Q = U_o \pi R^2$, where U_o is the pipe bulk velocity and R is the pipe radius. 108 diameter of straight pipe follows downstream of the contraction, in which the turbulent flow develops undisturbed. According to previous studies (see Klein [33]), the fetch of straight pipe should be sufficient for a fully developed turbulent flow to develop. The straight pipe is equipped with static pressure tappings, with an equal spacing of approximately $13D$. Air enters and leaves the system at atmospheric condition. Velocity and turbulence profiles were obtained $0.1D$ upstream of the pipe exit.

2.2 Pipe Rig Facility II

The second pipe rig, shown in Fig. 2.1 (b), consists of a 186 mm diameter smooth PVC pipe, with a straight fetch of 83 diameters. The same grid-honeycomb section, used in pipe rig I, was mounted before the pipe entrance. The purpose of making this second rig, was to examine an axisymmetric con-

6 CHAPTER 2. EXPERIMENTAL DETAILS AND DATA ANALYSIS

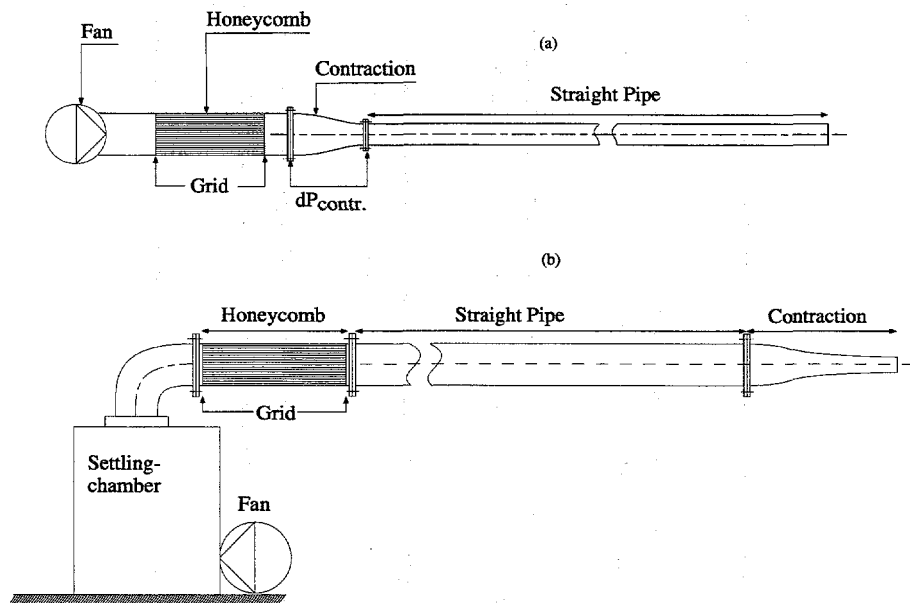


Figure 2.1: Pipe rig facility; Rig I (a) ; Rig II (b).

traction of fully developed pipe flow. A large contraction rate was desired, and to retain suitable dimensions, based on experimental resolution, a larger pipe diameter was needed. The contraction was mounted at the end of the straight pipe, as shown in Fig. 2.1(b). Due to a severe reduction of the streamwise turbulence intensity inside the contraction, noise reduction was offered great attention. Thus a settling chamber was mounted between the fan and the grid-honeycomb section, to reduce pressure fluctuations and mechanical vibrations. The settling chamber was supplied with screens and wall damping material. The straight pipe was equipped with static wall pressure tappings. The flow rate $Q = U_o \pi R^2$ was estimated from the static pressure drop, by assuming validity of Prandtl's friction factor (f). Integration of the mean velocity profiles, measured along a number of diagonals at the pipe exit, compared well with this procedure. Air enters and leaves the system at atmospheric condition.

2.3 Experimental Techniques

All experimental results presented in this thesis are based on Hot Wire Anemometry (HWA) measurements. It should be appropriate to state some arguments for choosing this technique rather than e.g. Laser Doppler Velocimetry (LDV). Maybe the biggest disadvantage of HWA is that it is intrusive, which means that a physical probe must be inserted in the flow. The size of the probe should be small compared to the flow dimensions, which is not possible e.g. near a solid wall. Inaccuracies due to wall effects, direction sensitivity of the wire, and spatial averaging has been a matter of discussion. Accurate calibration techniques are required, and the calibration is sensitive to deposition of pollution on the wire. The use of the hot-wire technique may therefore be tedious. A major advantage of HWA compared to LDV is that it produces a continuous time signal, which makes it easier to measure turbulence spectra. The biggest disadvantage of LDV is the particle seeding process. Particle size and concentration are a compromise between the need of a high acquisition rate, and the attempt to keep the particle fraction to a minimum. In the converging flow experiments, streamwise turbulence intensities are suppressed to values less than $(u_x^2)^{1/2}/U_x = 0.3\%$, which due to background noise would be difficult to resolve with LDV. Due to the discontinuity of the LDV signal, two-point correlations are difficult to obtain. To measure turbulence spectra requires interpolation of the time series, to

8 CHAPTER 2. EXPERIMENTAL DETAILS AND DATA ANALYSIS

generate a continuous signal. Keeping in mind the restrictions related to the technique, hot-wire anemometry was found to be the most appropriate one for the present experiments.

2.3.1 Static pressure

Static and total head pressure were measured by use of a linear response pressure transducer, calibrated towards a hydrostatic manometer. The calibration constant was determined with an accuracy better than 0.25%. The pressure transducer was also used as reference for velocity calibration of the hot-wire system. A 48 port Scanivalve system was used to measure the static pressure distribution along the pipe.

2.3.2 Hot-wire anemometry

The constant temperature hot-wire anemometers and signal conditioners were in-house made. The frequency response of the hot-wire anemometer system, which was checked prior to each experiment, depends on the hot-wire length, diameter and flow velocity, and was always found to be better than 15 kHz . All hot-wire probes were made in-house, with partially etched Platinum-10% Rhodium wires (silver coated). The wire length and spacing should be as small as possible, to avoid spatial averaging. Though, if the wires are made too short, heat loss and aerodynamic disturbance due to the wire supports will attenuate the accuracy. Wire selections were based on the suggested values reported by Browne et al. [13]. They recommended that the wire length to diameter ratio should exceed $l_w/d_w = 140$, and that the ratio of the wire length and Kolmogorov length should be less than $l_w/\eta = 5$. For cross wire probes the wire spacing should be less than $s_w/\eta = 3$. The cross-wire prongs were manufactured to give a nominal wire inclination angle of $\pm 45^\circ$. A yaw calibration in the range of $\pm 20^\circ$ was performed to determine the effective wire-angles, which were used to decompose the wire signals. For all experiments the effective angles were within $45 \pm 3^\circ$. A number of studies on cross-wire calibration has been reported (see e.g. Browne et al. [10]; Lueptow et al. [40]). Selection of inclination angle has been studied by e.g. Tagawa et al. [59], suggesting a best value of $\pm 45^\circ$ for low and moderate turbulence intensities. For high intensity flows, such as the outer edge of a turbulent jet, larger inclination angles have been found to give more accurate results (see Browne et al. [11]). The present experiments are restricted to low and mod-

Table 2.1: Hot-wire probe data

Config.		$d_w [\mu m]$	$l_w [mm]$	$s_w [mm]$
(1)	sw	1.27	0.25	-
(2)	sw	2.5	0.40	-
(3)	xw	2.5	0.50	0.5

erate intensities, and $\pm 45^\circ$ was therefore found to be the best choice. The geometry of the three hot-wire probes used in the present experiments are described in Tab 2.1 and Fig. 2.2. The probe manufacturing was the same as reported by Skåre [56]. The anemometer overheat ratio was 1.5 ± 0.1 . The hot-wire probes were calibrated in situ, that is in the pipe core region. Velocity reference was measured with a total head tube, connected to the pressure transducer. The hot-wire probe and the tube was mounted along one diagonal, equally biassed (5mm) from the centre line. Due to the axisymmetric property of the flow, the velocity at these two positions was near identical. The turbulence level in this region was less than 5%, which should not affect the accuracy of the calibration. The velocity calibration output voltage was fitted to the corresponding velocity values with a fourth order polynomial. For a detailed description of the velocity and probe angle calibration, see Skåre [56]. For each experiment, the density (ρ) and viscosity (ν) of the fluid was calculated from measured ambient pressure and temperature. These properties were assumed constant within the small temperature variations ($T \pm 2^\circ C$) that occurred during the experiment.

The traversing mechanism for the hot-wire probes, shown in Fig. 2.3 was mounted to a ring, which made it possible to measure all diagonals over the cross section. The accuracy of the angular positioning was 1° , and the radial positioning of the probes was better than $10 \mu m$.

2.3.3 Data acquisition

Each anemometer signal was low-pass filtered with second or fourth order analog Butterworth filters, and amplified to optimise the resolution of the computer acquisition unit. The signals were sampled on a Compaq 486 Personal Computer. The data acquisition package consists of a twelve bit R.C Electronics ISC-16 analog to digital plug-in card. The maximum sampling frequency, running on one channel, was 1MHz. Normally the sampling fre-

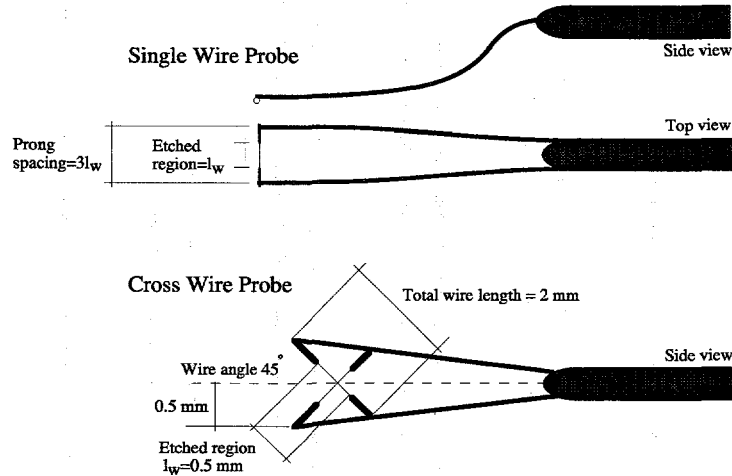


Figure 2.2: Geometry of single and crossed hot-wire probes.

quency (n_s) is taken as twice the value of the cut-off frequency (n_c), according to the Nyquist criteria. Since the Butterworth-filter only suppress signals larger than n_c , there is a chance that frequencies larger than n_c slips through the analog system, even though its amplitude is reduced. To avoid aliasing, test-runs were done by increasing n_s to $n_s = 3n_c$, and also by selecting higher order filters. This change gave no visible effect on the turbulence spectra. Each time series were stored in binary format on a 2 Gb Hard Disk. The binary data were transferred via Ethernet to a Digital Corp. Alpha Station, where all data analysis was performed. The reduced data set are available on CD-Rom for later use.

2.3.4 Fast Fourier transform

A fast Fourier transform (FFT)¹, using a Hanning window, has been applied to obtain turbulence spectra. The number of spectral points were 2^n , where n was varied between 10 and 16, depending on the number of data in the

¹The fast Fourier transform is a copy of the routine listed in "Introduction to digital signal processing", by J.G.Proakis and D.G.Manolakis, Maxwell Macmillian, 1989.

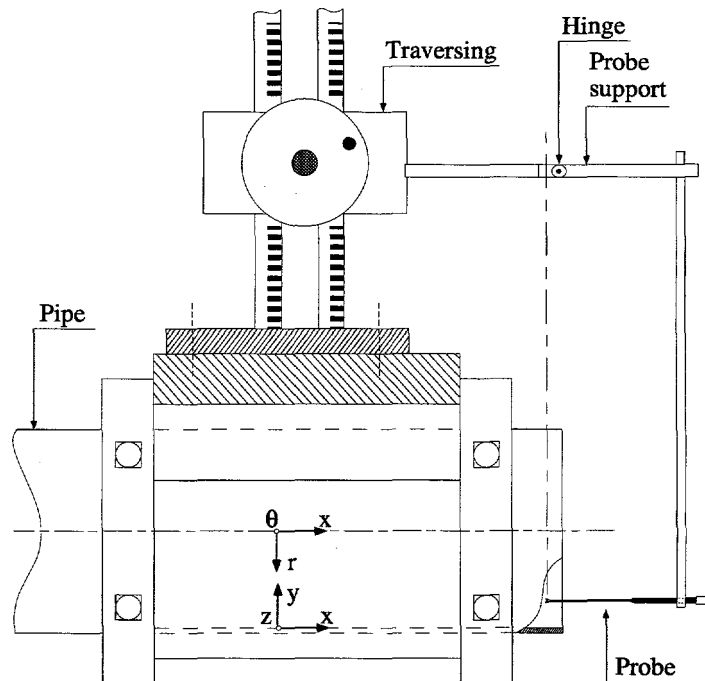


Figure 2.3: Traversing Mechanism and probe installation.

12 CHAPTER 2. EXPERIMENTAL DETAILS AND DATA ANALYSIS

time series. The window overlap was 50%. The number of windows for which the turbulence spectra are averaged is therefore equal to the total number of data divided by the number of spectral points (2^n).

2.4 Experimental procedure

Each experiment was carried out according to the following procedure:

- Probe geometry calibration
- Velocity calibration
- Adjusting the probe to give zero flow angle on the symmetry line
- Zero velocity sampling.
- Adjusting the flow rate to match the selected Reynolds number
- Taking a reference measurement on the pipe centre line
- Positioning the probe close to the pipe wall.
- Traversing the profile, and storing each time-series in binary format.
- Final measurement on the pipe centre line
- Measuring the axial static pressure distribution.

Hot-wire systems are sensitive to temperature variations, due to biasing of the calibration curve. For each time series the flow temperature was measured. Deviation from calibration temperature was compensated for in the data reduction algorithm. Temperature variation within one time-series was less than $\pm 0.5^\circ$, thus assumed constant. Positioning of the hot-wire probes close to the wall was done with aid of a zoom telescope, mounted on a traversing mechanism, as described by Skåre [56]. The center line reference

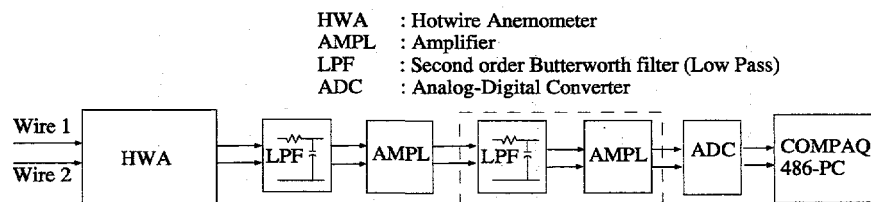


Figure 2.4: Acquisition system.

measurement was obtained to control hot-wire drift. If the mean velocity of the final measurement did not compare with the first reference measurement within the experimental accuracy, the whole experimental series was rejected.

14 CHAPTER 2. EXPERIMENTAL DETAILS AND DATA ANALYSIS

Chapter 3

Theory and Flow Documentation

The main purpose of this chapter, is to introduce the present use of coordinate systems and notation for turbulence quantities. Experimental results, both for the mean flow and for the turbulence statistics, are presented for the two straight pipe sections, described in the previous chapter.

3.1 Coordinate System

When working with axisymmetric problems, it is difficult to find arguments for not using cylindrical coordinates. The simplicity of the Cartesian representation is tempting, due to the convenient index notation. A disadvantage of the cylindrical coordinates is the singularity on the symmetry axis. Experimentally one will never measure exact zero values, even if the theoretical values are zero. This may cause problems for terms divided by the radial distance (r), when $r \rightarrow 0$. For convenience both a Cartesian system (x, y, z) and a cylindrical system (x, r, θ) is defined, where the x-axis is parallel to the symmetry axis. The two other directions are orthogonal, and in a plane normal to the symmetry axis, as shown in Fig. 2.3. The corresponding velocity components are (U, V, W) and (U_x, U_r, U_θ) . The two systems are referred to as cylindrical and Cartesian coordinates, and the reader will be noticed when changing the reference system. When using index notation, $i=1,2$ and 3 refer to (x, y, z) or (x, r, θ) respectively. Repeated indices denote summation.

3.2 Transport Equations

Osborne Reynolds (1895) (see Hinze [25]) introduced the decomposition of the instantaneous velocity-, pressure- and density-field into time averaged and fluctuating components, which forms the basic equations for describing turbulent flows. For a general instantaneous variable $\tilde{\Psi}(t)$, the decomposition writes

$$\tilde{\Psi}(t) = \Psi + \psi(t) = \frac{1}{t} \int_0^t \tilde{\Psi}(t) dt + \psi(t), \quad (3.1)$$

where Ψ is the long time average and $\psi(t)$ is the fluctuating part of $\tilde{\Psi}(t)$. Introduced in the Navier-Stokes equations, the single point Reynolds Averaged Navier-Stokes equations for a turbulent velocity field is obtained. Assuming incompressible-stationary flow, and homogeneity in the circumferential direction, the equations for the mean flow in cylindrical coordinates reduce to (see Hinze [25]):

$$\underbrace{U_r \frac{\partial U_x}{\partial r} + U_x \frac{\partial U_r}{\partial x}}_{Advection} = -\frac{1}{\rho} \frac{\partial P}{\partial x} + \underbrace{\nu \left(\frac{1}{r} \frac{\partial}{\partial r} \left(r \frac{\partial U_x}{\partial r} \right) + \frac{\partial^2 U_x}{\partial x^2} \right)}_{Visc.\text{stress}} - \underbrace{\frac{\partial}{\partial x} \overline{u_x^2} - \frac{1}{r} \frac{\partial}{\partial r} \left(r \overline{u_r u_x} \right)}_{Turb.\text{stress}} \quad (3.2)$$

$$\underbrace{U_r \frac{\partial U_r}{\partial r} + U_x \frac{\partial U_r}{\partial x}}_{Advection} = -\frac{1}{\rho} \frac{\partial P}{\partial r} + \underbrace{\nu \left(\frac{1}{r} \frac{\partial}{\partial r} \left(r \frac{\partial U_r}{\partial r} \right) + \frac{\partial^2 U_r}{\partial x^2} - \frac{U_r}{r^2} \right)}_{Visc.\text{stress}} - \underbrace{\frac{\partial}{\partial r} (\overline{u_r^2}) - \frac{\partial}{\partial x} (\overline{u_r u_x}) + \frac{1}{r} (\overline{u_\theta^2} - \overline{u_r^2})}_{Turb.\text{stress}} \quad (3.3)$$

$$\underbrace{\frac{1}{r} \frac{\partial}{\partial r} (r U_r) + \frac{\partial U_x}{\partial x}}_{Continuity} = 0 \quad (3.4)$$

Balance in the circumferential direction vanish due to homogeneity. The extra turbulent stress terms on the right hand side, form the basic closure problem in turbulent flows. These terms are normally called Reynolds stresses,

and may be expressed in tensorial form as,

$$\tau_{ij} = \rho \begin{pmatrix} \overline{u_x^2} & \overline{u_x u_r} & 0 \\ \overline{u_r u_x} & \overline{u_r^2} & 0 \\ 0 & 0 & \overline{u_\theta^2} \end{pmatrix} = \tau_{ji} \quad (3.5)$$

This is a symmetric tensor, in which the turbulent kinetic energy is conserved in the diagonal elements. The Reynolds Stress Transport (RST) equations, describe the transport mechanisms for each of the individual stress components. Introducing the same assumptions of homogeneity and incompressibility as for the mean flow, the equations for the three normal stresses in cylindrical coordinates reduce to¹:

$$\underbrace{U_r \frac{\partial}{\partial r} \left(\frac{\overline{u_x^2}}{2} \right) + U_x \frac{\partial}{\partial x} \left(\frac{\overline{u_x^2}}{2} \right)}_{A_{xx}} - \underbrace{\frac{\partial U_x}{\partial r} (\overline{u_r u_x}) - \frac{\partial U_x}{\partial x} (\overline{u_x^2})}_{P_{xx}} \\ - \underbrace{\frac{1}{r} \frac{\partial}{\partial r} \left(r \frac{\overline{u_r u_x^2}}{2} \right) - \frac{\partial}{\partial x} \left(\frac{\overline{u_x^3}}{2} \right)}_{D_{t,xx}} - \underbrace{\frac{\partial}{\partial x} \frac{\overline{u_x p}}{\rho}}_{D_{p,xx}} + \underbrace{\frac{p \partial \overline{u_x}}{\rho \partial x}}_{\Pi_{xx}} \\ + D_{v,xx} - \varepsilon_{xx} \quad (3.6)$$

$$\underbrace{U_r \frac{\partial}{\partial r} \left(\frac{\overline{u_r^2}}{2} \right) + U_x \frac{\partial}{\partial x} \left(\frac{\overline{u_r^2}}{2} \right)}_{A_{rr}} - \underbrace{\frac{\partial U_r}{\partial r} (\overline{u_r^2}) + \frac{\partial U_r}{\partial x} (\overline{u_x u_r})}_{P_{rr}} \\ - \underbrace{\frac{1}{r} \frac{\partial}{\partial r} \left(r \frac{\overline{u_r^3}}{2} \right) - \frac{\partial}{\partial x} \left(\frac{\overline{u_r^2 u_x}}{2} \right) + \left(\frac{\overline{u_r u_\theta^2}}{r} \right)}_{D_{t,rr}} - \underbrace{\frac{\partial}{\partial r} \frac{\overline{u_r p}}{\rho}}_{D_{p,rr}} + \underbrace{\frac{p \partial \overline{u_r}}{\rho \partial r}}_{\Pi_{rr}} \\ + D_{v,rr} - \varepsilon_{rr} \quad (3.7)$$

$$\underbrace{U_r \frac{\partial}{\partial r} \left(\frac{\overline{u_\theta^2}}{2} \right) + U_x \frac{\partial}{\partial x} \left(\frac{\overline{u_\theta^2}}{2} \right)}_{A_{\theta\theta}} - \underbrace{\frac{U_r}{r} (\overline{u_\theta^2})}_{P_{\theta\theta}} \\ - \underbrace{\frac{1}{r} \frac{\partial}{\partial r} \left(r \frac{\overline{u_r u_\theta^2}}{2} \right) - \frac{\partial}{\partial x} \left(\frac{\overline{u_x u_\theta^2}}{2} \right) - \frac{\overline{u_r u_\theta^2}}{r}}_{D_{t,\theta\theta}} - \underbrace{\frac{1}{r} \frac{\overline{p u_r}}{\rho}}_{D_{p,\theta\theta}} + \underbrace{\frac{p}{\rho} \left(\frac{1}{r} \frac{\partial \overline{u_\theta}}{\partial \theta} + \frac{\overline{u_r}}{r} \right)}_{\Pi_{\theta\theta}} \\ + D_{v,\theta\theta} - \varepsilon_{\theta\theta} \quad (3.8)$$

¹From the general coordinate representation of Nash & Patel [45]

The different terms have the following meaning: Advection A_{ij} , production P_{ij} , turbulent diffusion $D_{t,ij}$, pressure-diffusion $D_{p,ij}$, pressure-strain Π_{ij} , viscous diffusion $D_{v,ij}$ and dissipation ε_{ij} . Note that the equations are written in a form, where the sum of the pressure strain terms (Π_{kk}) are zero, due to continuity. To obtain this form, a pressure diffusion term has been added and subtracted to the equation for $\bar{u}_\theta^2/2$. A summation of the three equations for the normal stresses, gives the equation for the turbulent kinetic energy $k = (\bar{u}_x^2 + \bar{u}_r^2 + \bar{u}_\theta^2)/2$:

$$\underbrace{U_r \frac{\partial k}{\partial r} + U_x \frac{\partial k}{\partial x}}_{A_k} - \underbrace{\frac{\partial U_x}{\partial r}(\bar{u}_r u_x) - \frac{\partial U_x}{\partial x}(\bar{u}_x^2) - \frac{\partial U_r}{\partial r}(\bar{u}_r^2) + \frac{\partial U_r}{\partial x}(\bar{u}_x \bar{u}_r) - \frac{U_r}{r}(\bar{u}_\theta^2)}_{P_k} - \underbrace{\frac{1}{r} \frac{\partial}{\partial r}(r \bar{u}_r k) - \frac{\partial}{\partial x}(\bar{u}_x k)}_{D_{t,k}} - \underbrace{\frac{\partial}{\partial x}\left(\frac{\bar{u}_x p}{\rho}\right) - \frac{\partial}{\partial r}\left(\frac{\bar{u}_r p}{\rho}\right) - \frac{1}{r} \frac{\bar{p} \bar{u}_r}{\rho}}_{D_{p,k}} + D_{v,k} - \varepsilon_k \quad (3.9)$$

When presenting experimental results, it should be fair to report limitations, difficulties and assumptions which are constrained to the experimental procedure and results. Considering the RST equations, the difficulty of obtaining each term experimentally, may be divided into different categories. Advection, production, and turbulent diffusion, are dominated by the large energy containing scales. The experimental accuracy is limited by probe directional sensitivity and integration time, rather than small scale resolution. The single point time-averaged n'th order moments are represented by:

$$\bar{u}_i \bar{u}_j \dots \bar{u}_n = \frac{1}{t_s} \int_0^{t_s} [\tilde{U}_i(t) - U_i] \cdot [\tilde{U}_j(t) - U_j] \dots [\tilde{U}_n(t) - U_n] dt \quad (3.10)$$

The integration time (t_s) should be long enough to capture a sufficient number of the largest turbulent scales. Due to probe sensitivity it is more difficult to obtain accurate cross-stream velocities, than streamwise velocities.

The second category involves correlations between fluctuating pressure and velocity. Browne and Dinkelacker [14] measured wall pressure fluctuations in fully developed pipe flow, by use of miniature microphones. At the

present time no adequate equipment exists for measuring pressure fluctuations at the small level and high frequencies present inside a turbulent field. This means that the pressure-diffusion and pressure-strain terms are experimentally unobtainable by direct measurements. For the balance of total turbulent kinetic energy (k), the pressure-strain vanishes, and the problem is left to the pressure-diffusion. Recent analytical work, put forward by Lindborg [38], suggests a method for estimating the pressure-strain. The method is restricted to homogeneous axisymmetric turbulence, but should provide an important experimental verification of the redistribution process, which until now has been available only through direct numerical simulations.

The final category includes the viscous diffusion and dissipation. The first term is found to be negligible except near the wall[21]. The second term is the only sink term in the RST equations, and its accuracy is therefore of great importance. Common to these two terms are that they are both described by the small scale turbulence. Experimentally this requires a smallest possible measuring-volume, and sufficiently high frequency response to capture the Kolmogorov micro scales. This was one of the main motivations for choosing hot-wire anemometry.

3.3 Universality and Scaling

One of the basic challenges of turbulence research, is to determine the universality of theoretical, empirical and experimental results, since universality is of utmost importance for advances in turbulence modelling. It is clear however that universality must relate to proper scalings.

One of the essential scaling parameters is the dissipation rate, since it describes the amount of energy which is extracted from the turbulence. The exact expression for the dissipation rate reads (see Hinze [25]),

$$\varepsilon = \nu \overline{\left(\frac{\partial u_i}{\partial x_j} + \frac{\partial u_j}{\partial x_i} \right) \frac{\partial u_i}{\partial x_j}} \quad (3.11)$$

Assuming homogeneity in the small-scale motions, the dissipation rate reduces to the simpler form:

$$\varepsilon = \nu \overline{\frac{\partial u_i}{\partial x_j} \frac{\partial u_i}{\partial x_j}} \quad (3.12)$$

For homogeneous turbulence all off-diagonal elements of the dissipation rate tensor vanish, which means that Eq. 3.12 can be determined by nine different derivative terms. In classical turbulence theory, the dissipative scales are assumed isotropic. In this case Eq. 3.11 reduces to the simple form:

$$\varepsilon_{iso} = 15\nu \overline{(\frac{\partial u_x}{\partial x})^2} \quad (3.13)$$

To measure spatial derivatives, it is necessary to measure the velocity at two points in the flow. Since the dissipation is dominated by small scale motions, the spacing of the two probes must be very small. When using e.g. hot-wire anemometry, interference between the two probes will attenuate the accuracy. The usual method of estimating the dissipation rate is to apply the Taylor "Frozen Flow" approximation,

$$\frac{\partial}{\partial x} = \frac{-1}{U_x} \frac{\partial}{\partial t}, \quad (3.14)$$

where U_x is the local mean streamwise velocity. The Taylor hypothesis simply states that the turbulent fluctuations are convected with the local mean streamwise velocity. This means that the hypothesis is restricted to low turbulence intensity. A detailed description of convection velocity associated with different scales has been reported by Lumley [41]. The isotropic relation for the dissipation rate may then be written in the well known form:

$$\varepsilon_{iso} = \frac{15\nu}{U_x^2} \overline{(\frac{\partial u_x}{\partial t})^2} \quad (3.15)$$

Equation 3.15 may seem a naive measure of the total 27 different terms, but is still believed to be a good approximation if:

- The turbulence intensity is sufficiently low for application of the Taylor hypothesis.
- The anisotropy of the energy containing scales is moderate, such that the dissipative scales may be assumed isotropic.
- The experimental resolution of the smallest scales is sufficient.
- Absence of high frequency signal noise.

From an experimental point of view, the main disadvantage of Eq. 3.15, is that even the smallest turbulent scales must be resolved. In many experimental situations, the lack of small-scale resolution is likely to cause a larger

error than the deviation from small scale isotropy. It is also important to note that the entire range of scales for which dissipation occurs, must be isotropic. It will be shown that this requires the large energy containing scales being sufficiently separated from the dissipative scales. The assumption of isotropy, means that the small scale turbulence is invariant to reflections and rotations about all axes. If the large scales are highly anisotropic, this is not obviously the case. The main argument for using the isotropic expression for the dissipation rate, is the inaccuracy associated with measuring additional terms of the dissipation rate tensor. George and Hussein [24] deduced the corresponding relation, assuming invariant reflection about only one axis, that is for axisymmetric turbulence,

$$\varepsilon_{axi} = \nu \left\{ -\overline{\left(\frac{\partial u_x}{\partial x}\right)^2} + 2\overline{\left(\frac{\partial u_x}{\partial r}\right)^2} + 2\overline{\left(\frac{\partial u_r}{\partial x}\right)^2} + 8\overline{\left(\frac{\partial u_r}{\partial r}\right)^2} \right\} \quad (3.16)$$

They clearly emphasised the difficulty of obtaining the cross-stream derivatives when multiple cross-wires were used. Ould-Rouis et al. [47] reported an even simpler estimate for axisymmetric dissipation rate, as

$$\varepsilon_{axi} = (3 + \frac{12}{K_1})\nu \overline{\left(\frac{\partial u_x}{\partial x}\right)^2} : \quad K_1 = 2\overline{\left(\frac{\partial u_x}{\partial x}\right)^2}/\overline{\left(\frac{\partial u_r}{\partial x}\right)^2} \quad (3.17)$$

For isotropic turbulence, $K_1 = 1$, and the axisymmetric expression reduces to Eq. 3.15. If K_1 is larger than unity, then $\varepsilon_{axi} < \varepsilon_{iso}$, similarly if K_1 is smaller than unity, then $\varepsilon_{axi} > \varepsilon_{iso}$. Additional terms which are added to the expression for the isotropic dissipation rate, must therefore be considered as correction terms, caused by lack of small scale isotropy.

A parameter describing the "degree of turbulence", is the turbulent Reynolds number, defined as:

$$R_\lambda = \frac{\overline{(u_x^2)^{1/2}}}{\nu}, \quad (3.18)$$

where the longitudinal Taylor length scale (λ) is normally expressed as:

$$\lambda = \left\{ 15\nu \frac{\overline{u_x^2}}{\varepsilon} \right\}^{1/2} \quad (3.19)$$

A number of theoretical results are limited to high and infinite R_λ . The ability of producing high R_λ is different for different flow geometries. E.g.

a turbulent jet produces a significantly higher R_λ than e.g. a fully developed pipe flow. Thus most high R_λ results are reported for jet flow or atmospheric boundary layers. Due to the realisability constraint, turbulence models should apply to the limit of infinite R_λ , although this might be far beyond the range of practical flow problems. In the case of fully developed pipe flow, Eq. 3.18 may be written in terms of proper scalings, which results in approximately constant values of the non-dimensional dissipation rate and normal stress in the outer region, that is independent of the Reynolds number. Introducing the wall friction velocity $u^* = (\tau_w/\rho)^{1/2}$, where τ_w is the total wall shear stress and ρ is the fluid density, R_λ may be rewritten in the convenient form:

$$R_\lambda = \left\{ \frac{15}{4} (u_x^+)^4 (\varepsilon^*)^{-1} \left[\frac{f}{2} \right]^{1/2} Re \right\}^{1/2} \quad (3.20)$$

where

$$u_x^+ = \left[\frac{(\overline{u_x^2})^{1/2}}{u^*} \right] ; \quad \varepsilon^* = \left[\frac{R\varepsilon}{(u^*)^3} \right] ; \quad f = f(Re) \quad (3.21)$$

This result follows directly by introducing Eq. 3.19 into Eq. 3.18, together with the relation between the friction velocity and the Prandtl friction factor: $u^* = [f/8]^{1/2} U_o$. The parameters u_x^+ and ε^* are the non-dimensional streamwise normal stress and dissipation rate, which are functions of the radial coordinate. Assuming that the Reynolds number variation of u_x^+ and ε^* is small, the turbulent Reynolds number for each location in the pipe cross section, becomes only a function of the bulk Reynolds number ($Re = U_o D / \nu$). The minimum value of R_λ (except very close to the pipe wall) appears on the pipe centre line. A number of pipe flow experiments supports $u_x^+(y/R = 1) = 0.9$ (See e.g. Toonder et al. [61]; Browne et al. [14]), which is also confirmed by the present results. Lawn reported $\varepsilon^*(y/R = 1) = 1.7$, and the present results indicate $\varepsilon^*(y/R = 1) \in [1.45, 1.6]$. A value of 1.5 is chosen as an estimate. The maximum of R_λ appears near the half radius. The present results indicate that $u_x^+(y/R = 1/2) = 1.5$ and $\varepsilon^*(y/R = 1/2) = 3.6$ can be taken as appropriate values. Figure 3.1 shows a tentative extrapolation of R_λ for the pipe centre line and the half radius location. The figure gives an idea of the magnitude of R_λ that is achievable in fully developed pipe flow. It is clear that the flow does not generate high R_λ at laboratory scale experiments. For

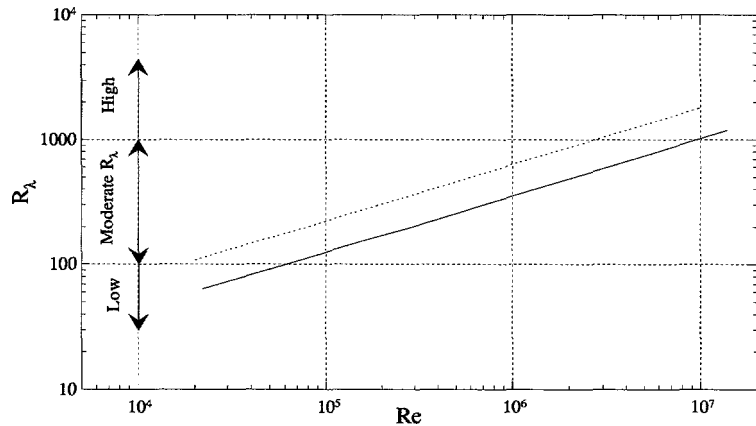


Figure 3.1: Estimated centre line and half radius variation of the turbulent Reynolds number, $R_\lambda(Re)$, in fully developed pipe flow. $y/R=1$ (solid); $y/R=1/2$ (dashed).

a bulk Reynolds number of $Re = 1 \times 10^6$, which is considered a high value for laboratory scales, the estimated centre line and half radius R_λ values are 340 and 630, respectively. The importance of R_λ , in context of universal scaling, will be discussed in further detail in the following chapters.

For the smallest turbulent scales, the Kolmogorov length,

$$\eta = \{\nu^3/\varepsilon\}^{1/4}, \quad (3.22)$$

and velocity

$$v = \{\nu\varepsilon\}^{1/4}, \quad (3.23)$$

is normally introduced as proper scaling parameters.

3.4 Verification of Fully Developed Pipe Flow

A large number of experimental data are available for the situation of fully developed pipe flow, both for smooth and for rough pipes. Thus the need for additional results can only be argued on basis of advances in experimental techniques and computer technology. The intention of the results presented in this section is mainly to confirm the flow situation, which forms the basis for

the following chapters, and not to report an additional set of data. However, the reader may find some of the data interesting, due to improvement in experimental time-space resolution, since the time of more classical results.

The pipe rig facilities and experimental procedure are described in detail in Chapter 2. The results presented in this section are obtained at approximate bulk Reynolds numbers of $Re = 22.000$ and $Re = 75.000$ in pipe rig I, and $Re = 35.000$ and $Re = 75.000$ in pipe rig II. The essential parameters are assembled in Table 3.1

3.4.1 Global parameters

For pipe rig I, the bulk velocity U_o , was calculated from the measured pressure difference over the entrance contraction, and for pipe rig II from the streamwise static pressure drop along the pipe. The integrated mean velocity was also estimated from the measured streamwise velocity distribution in different quadrants of the cross section, such that

$$\bar{U} = \frac{1}{\pi R^2} \int_0^R 2\pi r U_x(r) dr \quad (3.24)$$

and compared to the bulk velocity in Tab. 3.1. The integration was based on the trapezium rule, and differences between U_o and \bar{U} were found to be less than 0.4%. This indicates accurate velocity calibrations, and also reflects the circumferential homogeneity of the flow. Tab. 3.1 also shows the streamwise velocity at the location $r = \frac{3}{4}R$, which compares within 1.5% of the bulk velocity U_o . This is in agreement with classical theory, and recent results obtained by Zagarola et al. [67] for high Reynolds number pipe flow. From Fig. 3.2 it is clear that the streamwise pressure drop is linear beyond $(x/D) \approx 15$. This yields an accurate measure of the friction velocity,

$$u^* = \left[\frac{D}{4\rho} \left| \frac{dP}{dx} \right| \right]^{1/2} ; \quad \frac{4(u^*)^2}{D} = -\frac{1}{\rho} \frac{dP}{dx} \quad (3.25)$$

Prandtl's friction factor (f) for fully developed pipe flow in smooth pipes may be expressed by the semi-empirical relation [64],

$$\frac{1}{f^{1/2}} = 2.0 \log(Re f^{1/2}) - 0.8 ; \quad Re = \frac{U_o D}{\nu} \quad (3.26)$$

Table 3.1: Experimental parameters.

Re	Pipe rig I		Pipe rig II	
	A 22.223	B 74.447	C 35.608	D 75.405
$n_c [kHz]$	2.5	10	4	4
$n_s [kHz]$	7.5	20	10	10
$t_s [s]$	112	40	120	120
$T [^{\circ}C]$	24	22	18	18
$\rho [kg/m^3]$	1.18	1.19	1.21	1.20
$\nu \times 10^5 [m^2/s]$	1.54	1.52	1.48	1.48
$U_o [m/s]$	3.72	12.30	2.82	6.00
$\bar{U} [m/s]$	3.71	12.30	2.83	6.01
$U_{3/4} [m/s]$	3.72	12.25	2.85	6.09
b	0.194	0.181	0.210	0.185
$u^* [m/s]$	0.210	0.600	0.153	0.293
$u_{Prandtl}^* [m/s]$	0.209	0.602	0.150	0.293
$u_{x,max}^+$	2.69	2.69	2.61	2.60
$y^+(u_{x,max}^+)$	14.7	14.8	15.2	15.0
$u_{r,max}^+$	1.05	1.05	1.10	1.08
$y^+(u_{r,max}^+)$	~100	~100	~100	~100
$R\varepsilon/(u^*)^3$	1.45	1.51	1.48	1.47
$\lambda_{cl} [mm]$	4.69	3.10	7.3	5.64
$\eta_{cl} [mm]$	0.329	0.148	0.46	0.29
$Re_{\lambda,cl}$	52	113	64.55	95.15
$K_{1,cl}$	1.26	1.27	1.01	1.04

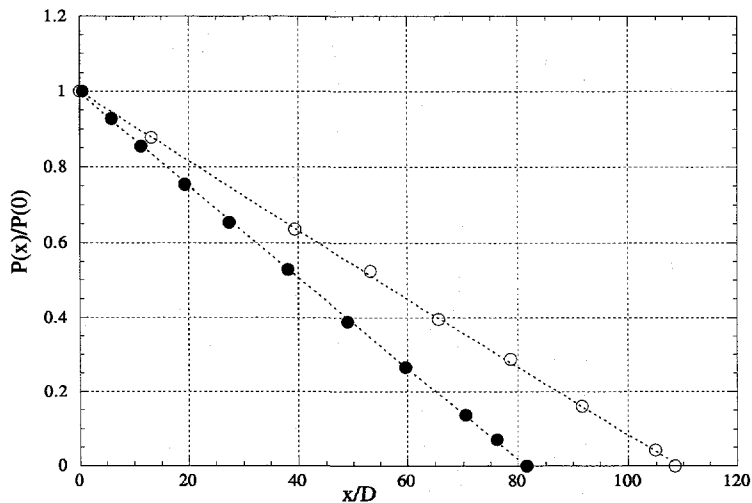


Figure 3.2: Streamwise pressure drop. Rig I (○) ; Rig II (●)

where Re is the bulk Reynolds number. This gives a second estimate of the friction velocity,

$$u^* = \left[\frac{f}{8} U_o^2 \right]^{1/2}, \quad (3.27)$$

which agreed with Eq. 3.25 within the experimental accuracy.

3.4.2 Homogeneity

Fully developed pipe flow implies homogeneity in the circumferential and streamwise direction. A review of sufficient pipe lengths required for fully developed pipe flow conditions, has been reported by Klein [33]. The flow development was discussed on basis of the shape of the mean streamwise velocity profile, using Sovran and Klopp's [57] blockage factor,

$$b = \left(1 - \frac{U_o}{U_{x,cl}} \right). \quad (3.28)$$

Klein reported an increase in the blockage factor from the pipe entrance (uniform profile ; $b = 0$) up to approximately $x/D = 40$, followed by a

slight decrease and stabilisation further downstream. Klein also emphasised a significant effect of the entrance conditions, and reported possible oscillations during the stabilisation process. Figure 3.3 shows a review of the blockage factor Reynolds number variation. The analytical value for laminar flow is $b = 0.5$. The high Reynolds number results of Zagarola et al. [67] indicates a limiting value of $b \simeq 0.1$ for infinite Re . The present results closely follows the results of Browne and Dinkelacker [14]. A peak in the blockage factor is observed near $Re \simeq 35.000$. Klein reported a decrease in b , with increasing Reynolds number, which is confirmed by the present result for $Re > 35.000$. It is clear however that for the purpose of turbulence research, the blockage factor is a naive measure of flow development. Stabilisation of higher order turbulence statistics is likely to be more sensitive to pipe length and entrance conditions. The "true" definition of fully developed pipe flow is therefore a complex matter. Selection of pipe lengths are normally based on convenience, which is a compromise between pipe diameter, Reynolds number and spatial resolution of the measuring equipment.

Figure 3.4 shows the mean streamwise velocity defect ($U_{x,cl}^+ - U_x^+$) for the two pipe rig configurations, measured in different quadrants of the cross section. The subscript (cl) denotes centre line, and the superscript denotes normalisation with the friction velocity. Local variations were found to be within the experimental accuracy, thus no significant circumferential inhomogeneity was present. Figure 3.5 pictures the streamwise normal stress $u_x^+ = (\overline{u_x^2})^{1/2}/u^*$ for the same diagonals. Also here the circumferential variation was within the experimental accuracy. This check on homogeneity was performed at $Re = 75.000$ for both pipe rigs.

3.4.3 Mean velocity

Figure 3.6 shows the mean streamwise velocity, normalised with the friction velocity (u^*) and the fluid viscosity (ν), such that $U_x^+ = U_x/u^*$ and $y^+ = yu^*/\nu$. The friction velocity was obtained from the streamwise pressure drop, and y refers to the wall normal coordinate, with its origin on the pipe wall. The region closest to the wall is normally called the viscous sublayer, which from classical theory is described by the linear behaviour,

$$U_x^+ = (y^+) + \dots ; \quad y^+ < 5 \quad (3.29)$$

However, it will be shown in the following text that higher order corrections are needed, to achieve the correct behaviour of the near wall turbulent

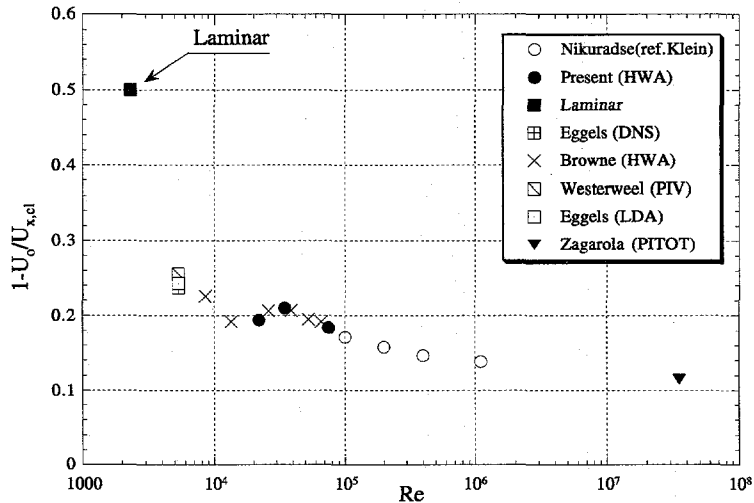


Figure 3.3: Review of blockage factor, $b = (1 - \frac{U_o}{U_{x,cl}})$, in fully developed pipe flow.

shear stress. Present results do not cover the viscous subrange, and further comments will be based on reported experimental and numerical results.

For the region outside $y^+ \simeq 30$, the data follow the logarithmic region, described by,

$$U_x^+ = \frac{1}{\kappa} \ln(y^+) + B \quad ; \quad y^+ > 30 \quad (3.30)$$

In the literature there seems to be a general agreement of the von Karman constant $\kappa = 0.41$, both for external boundary layer flows and for internal flows, such as pipe flow. Reported values of the constant B are more scattered, and some previously applied values are assembled in Tab. 3.2. For the present experiments, $\kappa = 0.41$ and $B = 5.5$ gave the best fit to the measured data. Figure 3.6 shows $U_x^+(y^+)$ for two different Reynolds numbers in each pipe rig, described in Tab. 3.1. For $Re = 75.000$ in both pipe rigs, the data are seen to collapse. It can easily be shown that the non-dimensional radius R^+ is only a function of the bulk Reynolds number, independent of the difference in pipe diameters. Thus these two curves should be identical within the experimental accuracy.

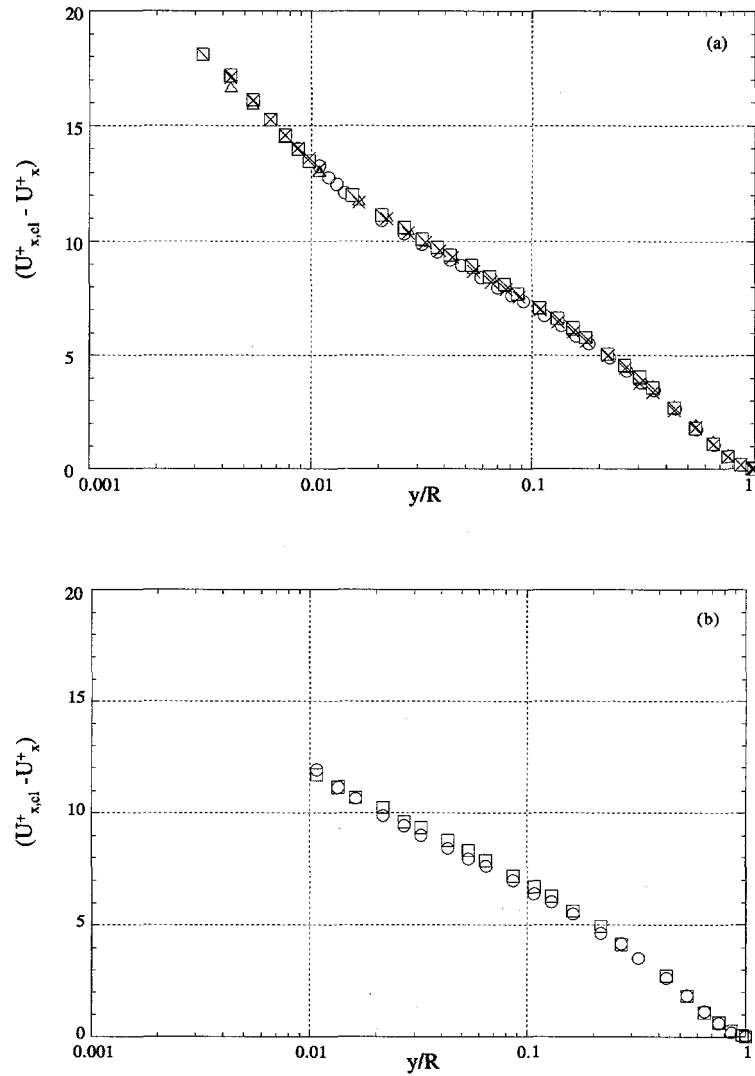


Figure 3.4: Circumferential homogeneity of the mean streamwise velocity, measured along different diagonals at $Re = 75.000$. Fig.(a) shows four radii in pipe rig I(single-wire), and Fig.(b) shows two radii in pipe rig II(cross-wire).

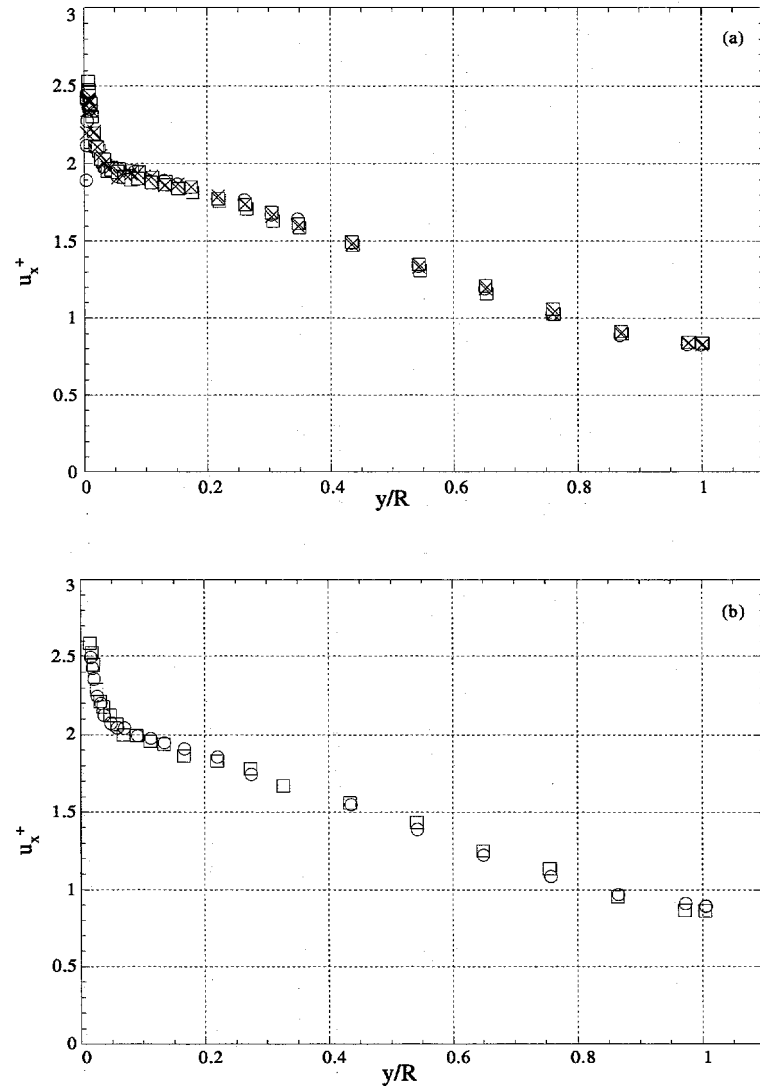


Figure 3.5: Circumferential homogeneity of the streamwise intensity $u_x^+ = (\bar{u}_x^2)^{1/2}/u^*$, measured along different diagonals at $Re = 75.000$. Fig.(a) shows four radii in pipe rig I, and Fig.(b) shows two radii in pipe rig II.

Table 3.2: Different values of κ and B for fully developed pipe flow.

Authors	Year	Instr.	$Re \times 10^{-4}$	κ	B
Lawn	1971	HWA	3.6 – 24.9	0.42	5.45
Chevrin et al.	1992	LDV	0.893	0.41	5.5
Browne & Dinkelacker	1995	HWA	> 2.60	0.41	5.1
Fontaine & Deutch	1995	LDV	1.01	0.4	5.5

3.4.4 Reynolds stress tensor

Time averaged Reynolds stresses were obtained with single and crossed hot-wire probes. Due to the homogeneity in axial and circumferential direction, the Reynolds stress tensor for fully developed pipe flow reads:

$$\tau_{ij} = \begin{pmatrix} \tau_{xx} & \tau_{xr} & 0 \\ \tau_{rx} & \tau_{rr} & 0 \\ 0 & 0 & \tau_{\theta\theta} \end{pmatrix} = \rho \bar{u}_i u_j \quad (3.31)$$

It is possible to obtain all non-zero elements of the Reynolds stress tensor with a cross-wire probe, oriented in the (x, r) and (x, θ) plane respectively. The only shear stress component is (τ_{xr}) , in direction of the mean flow gradient. Figure 3.7 and Fig. 3.8 present Reynolds normal stresses for the two pipe rig configurations, rendered non-dimensional with the friction velocity (u^*). A Reynolds number effect can be seen for both pipe rigs. The lower Reynolds numbers also offer better near wall hot-wire resolution. The maximum values, with the corresponding distances from the pipe wall, are presented in Tab. 3.1. The peak value of u_x^+ compares well with the empirical relation,

$$u_{x,max}^+ = -0.0000024R^+ + 2.70 \quad ; \quad y^+ = 0.00020R^+ + 14.6 \quad (3.32)$$

reported by Mochizuki and Nieuwstadt [44]. This result was based on a large number of internal pipe- and channel-flow experiments. It is possible to show that the turbulence intensity $Tu_i = u_i^+/U_x^+$ must take a finite value at the pipe wall. Applying a series expansion of the turbulent fluctuations very near the wall ($y^+ < 2$), keeping only the first order term in the expansion gives:

$$\begin{aligned} u_x^+ &= a_1 y^+ + \dots \\ u_r^+ &= \dots + \dots \\ u_\theta^+ &= c_1 y^+ + \dots \end{aligned} \quad (3.33)$$

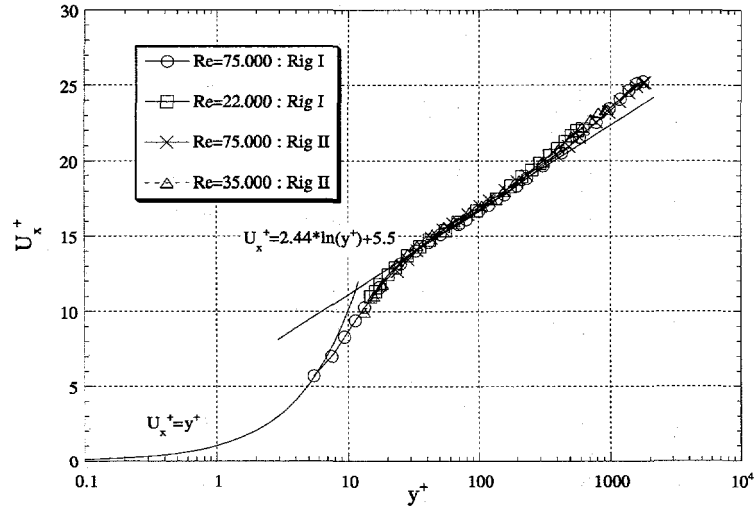


Figure 3.6: Mean streamwise velocity $U_x^+(y^+)$ for the two pipe rigs at various Reynolds numbers.

The limit of $u_r^+ \sim (y^+)^2$ due to continuity. The two remaining components reduce to:

$$\begin{aligned} Tu_{x,wall} &= \lim_{y^+ \rightarrow 0} \frac{u_x^+}{U_x^+} = \frac{a_1 y^+ + \dots}{y^+} = a_1 \\ Tu_{\theta,wall} &= \lim_{y^+ \rightarrow 0} \frac{u_\theta^+}{U_x^+} = \frac{c_1 y^+ + \dots}{y^+} = c_1 \end{aligned} \quad (3.34)$$

Different values of a_1 and c_1 have been reported. Direct numerical simulation data from channel flow by Kim et al. [32] suggests $a_1 = 0.36$ and $c_1 = 0.20$, thus

$$\begin{aligned} Tu_{x,wall} &= 36\% \\ Tu_{\theta,wall} &= 20\% \end{aligned} \quad (3.35)$$

Close to the wall, Durst et al. [19] suggested that the streamwise and lateral turbulence intensity approached constant values of $Tu_x = (\overline{u_x^2})^{1/2}/U_x = 37\%$ and $Tu_\theta = (\overline{u_\theta^2})^{1/2}/U_x = 21\%$. They also confirmed that there was no visible Reynolds number effect. The present results, obtained with cross-wire probes, do not supply data sufficiently close to the wall. However, detailed

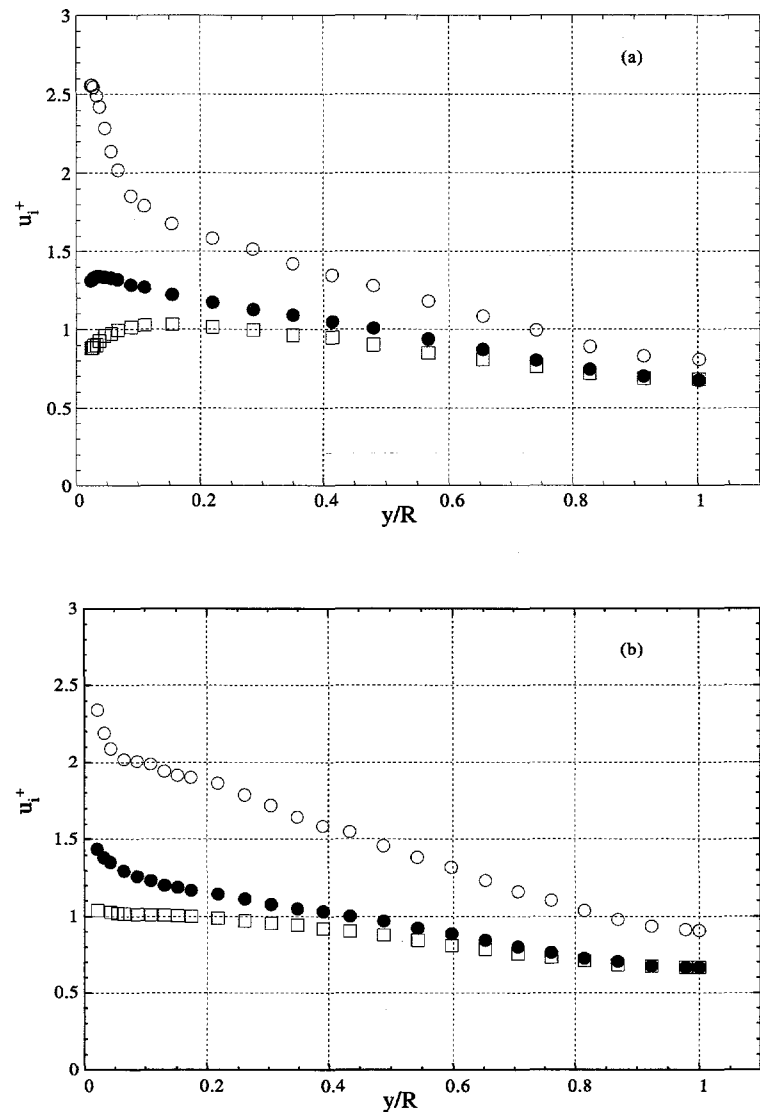


Figure 3.7: Reynolds normal stresses in pipe rig I, scaled with the friction velocity: u_x^+ (\circ) ; u_r^+ (\square) ; u_θ^+ (\bullet). Fig.(a) ($Re=22.000$) ; Fig.(b) ($Re=75.000$).

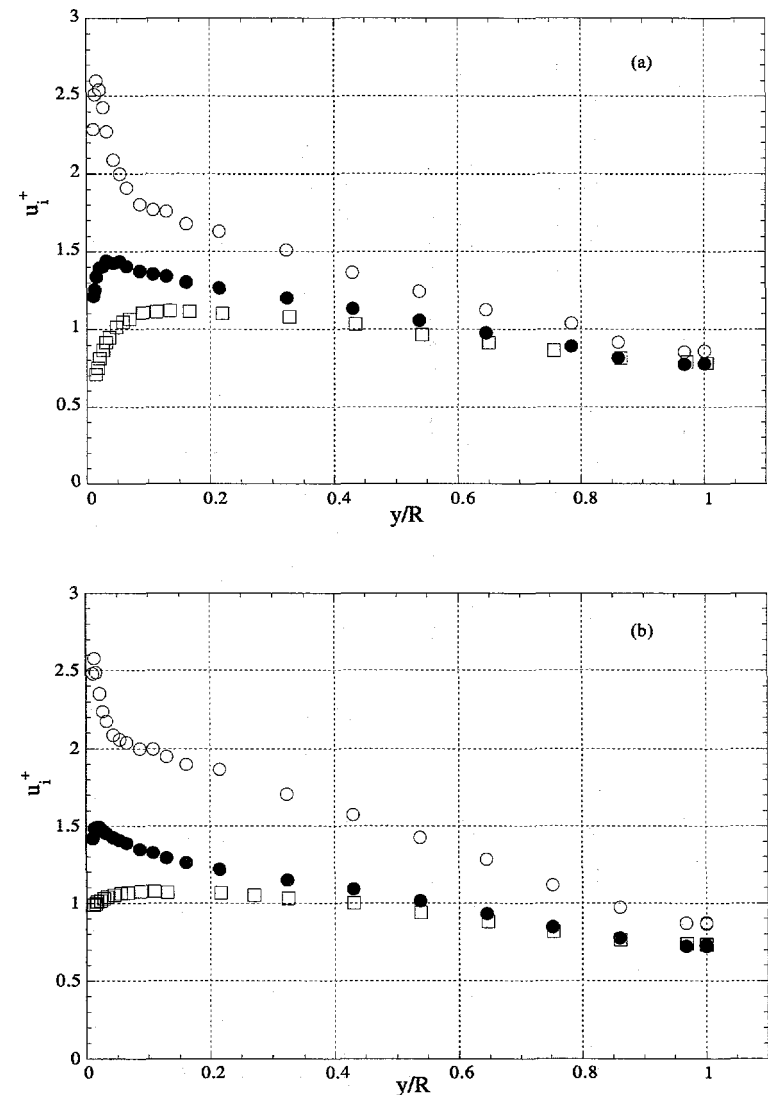


Figure 3.8: Reynolds normal stresses in pipe rig II, scaled with the friction velocity: $+\bar{u}_x^+$ (\circ) ; $+\bar{u}_r^+$ (\square) ; $+\bar{u}_\theta^+$ (\bullet). Fig.(a) ($Re=35.000$) ; Fig.(b) ($Re=75.000$). For caption see Fig 3.7.

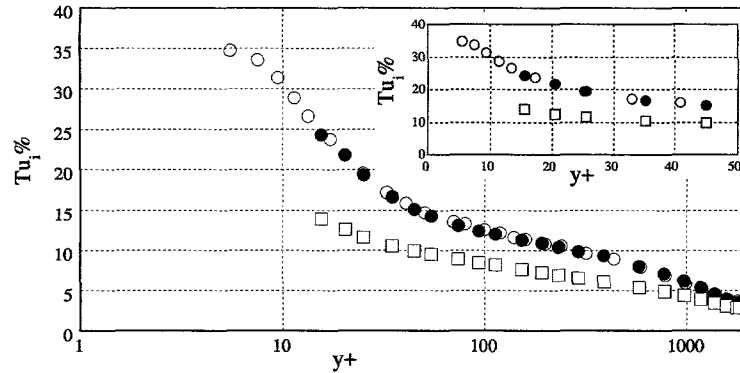


Figure 3.9: streamwise and circumferential turbulence intensity: $Tu_x\%$ (single-wire) (\circ) ; $Tu_x\%$ (cross-wire) (\bullet) ; $Tu_\theta\%$ (cross-wire) (\square). $Re = 75.000$

measurements with a $1.27 \mu m$ diameter single-wire (Fig. 3.9), indicates an extrapolation to $Tu_{x,wall} \simeq 36\%$, which supports the findings of Kim et al. Figure 3.9 also indicates a close correspondence between the single-wire and cross-wire data, in the range for which cross-wire results are available. The centre line streamwise intensity remains constant at $Tu_x \simeq 3.5\%$, for the present range of Reynolds numbers. Figure 3.10 shows the total turbulent kinetic energy $k = (u_x^2 + u_r^2 + u_\theta^2)/2$, normalised with the friction velocity. The results indicate an increasing level of k^+ with increasing Reynolds number in the outer region.

The turbulent shear stress $\overline{u_x u_r}$ may be expressed in terms of the mean streamwise velocity gradient. The momentum equation in the streamwise direction (Eq.3.2) simplifies to:

$$0 = -\frac{1}{\rho} \frac{\partial P}{\partial x} + \frac{1}{r} \frac{\partial}{\partial r} \left\{ r \left(\nu \frac{\partial U_x}{\partial r} - \overline{u_x u_r} \right) \right\}. \quad (3.36)$$

The pressure gradient term may be exchanged with the friction velocity,

$$-\frac{1}{\rho} \frac{\partial P}{\partial x} = \frac{2(u^*)^2}{R}, \quad (3.37)$$

such that the inner scaling of Eq. 3.36 may be written as:

$$0 = \frac{2}{R^+} + \frac{1}{r^+} \frac{\partial}{\partial r^+} \left\{ r^+ \left(\nu \frac{\partial U_x}{\partial r^+} - \overline{u_x u_r}^+ \right) \right\} \quad (3.38)$$

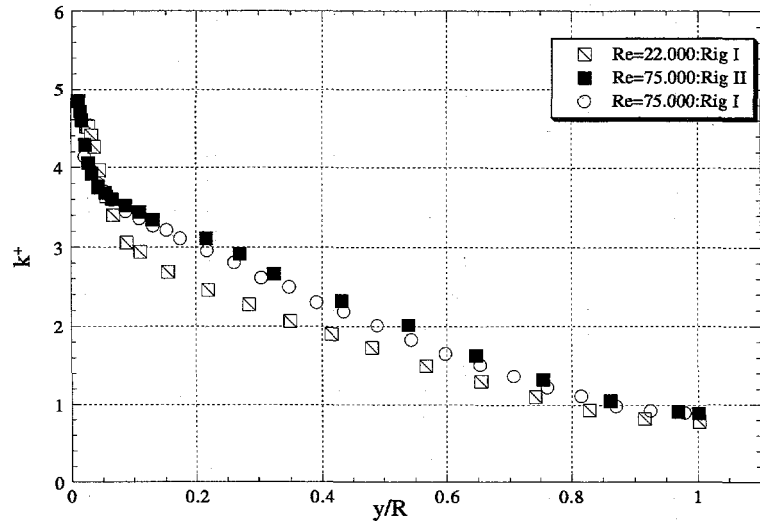


Figure 3.10: Turbulent kinetic energy, $k^+ = [(u^+)_x^2 + (u_r^+)^2 + (u_\theta^+)^2]/2$, in fully developed pipe flow.

Integrating with respect to r^+ , and introducing the boundary condition at $r^+ = 0$, the analytical expression for the shear stress becomes:

$$\frac{\overline{u_x u_r}^+}{\text{Tot.stress}} = \underbrace{\frac{r^+}{R^+}}_{\text{Visc.stress}} + \underbrace{\frac{\partial U_x^+}{\partial r^+}}_{\text{Tot.stress}} = 1 - \underbrace{\frac{y^+}{R^+}}_{\text{Visc.stress}} - \underbrace{\frac{\partial U^+}{\partial y^+}}_{\text{Visc.stress}} = -\overline{uv}^+ \quad (3.39)$$

The shear stress has here been expressed both in cylindrical coordinates ($\overline{u_x u_r}^+$) and Cartesian coordinates (\overline{uv}^+). In classical theory of turbulence, the linear behaviour of U_x^+ in the viscous sublayer ($y^+ < 5$), has been a well accepted truth. In disfavour of this well founded result, Durst et al. [20] reported nonlinear variations of U_x^+ in the vicinity of a wall. The conclusions were drawn from near wall LDV measurements and DNS results. A strong support for this result, is the near wall behaviour of $\overline{u_x u_r}^+$. If U_x^+ was truly linear, then

$$\overline{u_x u_r}^+ = \frac{r^+}{R^+} - 1 = -\frac{y^+}{R^+} = -\overline{uv}^+, \quad (3.40)$$

which forces $\overline{u_x u_r}$ to become negative in the viscous sublayer. All experimental evidence shows that this is not possible. Applying a series expansion of

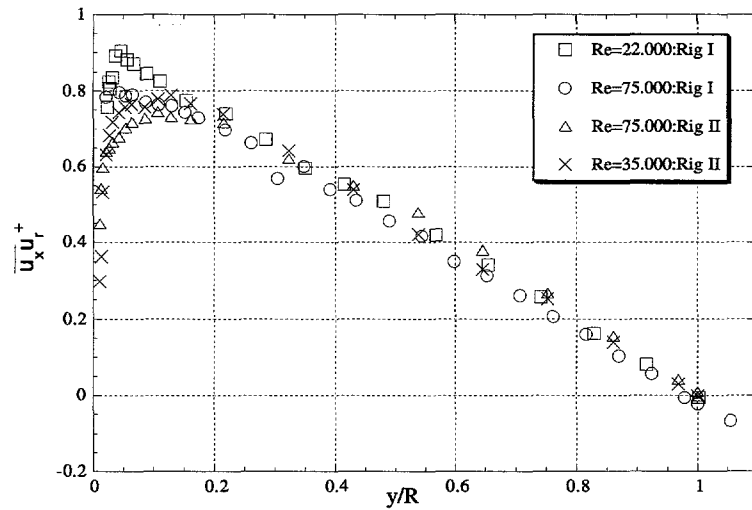


Figure 3.11: Turbulent shear stress, $\bar{u}_x \bar{u}_r^+$ for both pipe rigs at various Reynolds numbers.

the near wall shear stress,

$$uv^+ = d_3 y^{+3} + d_4 y^{+4} + \dots \quad (3.41)$$

results in a higher order correction for the sublayer mean velocity,

$$U_x^+ = y^+ - \frac{1}{2R^+} y^{+2} + d_3 y^{+4} + d_4 y^{+5} + \dots \quad (3.42)$$

For high Reynolds numbers $R^+ \rightarrow \infty$, the second term on the right hand side vanishes. The correction to the linear behaviour is then $O(y^{+4})$. Present results are not available inside the buffer region, and no attempt is therefore made to confirm this argument. It is left as an important observation.

Figure 3.11 shows the measured turbulent shear stress, scaled with the friction velocity, for both pipe rigs at various Reynolds numbers. In the outer region the data follow the linear trend as expected. Close to the pipe wall the peak in the shear stress distribution should theoretically be shifted towards the wall and increase with increasing Reynolds number. This is not reflected in the present results, which is probably due to insufficient cross-wire probe resolution.

3.4.5 Turbulent scales

Figure 3.12 pictures the radial variation of the Kolmogorov length scale, the Taylor micro scale, and the turbulent Reynolds number. The data are obtained at $Re = 75.000$ in rig I, with a $1.27 \mu\text{m}$ diameter single-wire. The length scales are made non-dimensional with the friction velocity and the viscosity, such that $\eta^+ = \eta u^*/\nu$ and $\lambda^+ = \lambda u^*/\nu$, thus represents the number of viscous units. The Kolmogorov length scale varies from $\eta^+ \simeq 6$ on the pipe centre line to $\eta^+ \simeq 2$ when approaching the wall. The Taylor micro scale obtains a value of $\lambda^+ \simeq 125$ on the pipe centre line, and has a maximum of $\lambda^+ \simeq 130$ near $y^+ = 1200$. The turbulent Reynolds number is $R_\lambda = 112$ on the centre line, and increases to its maximum value of $R_\lambda \simeq 200$ near the half radius. A second peak appears near $y^+ = 15$, which corresponds to the maximum of the streamwise intensity. Inside $y^+ = 15$, R_λ decreases rapidly towards the wall.

3.4.6 Turbulent kinetic energy budget

From the present experimental basis, it is not possible to obtain a balance for the individual components, since the pressure-strain terms and the different elements of the dissipation tensor are not available. The following analysis will focus only on the balance for the total turbulent kinetic energy, based on experimental results at $Re = 75.000$ in pipe rig I. The transport equation for the turbulent kinetic energy in fully developed pipe flow reduces to,

$$0 = \underbrace{-\frac{\partial U_x}{\partial r}(\overline{u_r u_x})}_{P_k} - \underbrace{\frac{1}{r} \frac{\partial}{\partial r}(\overline{r u_r k})}_{D_{t,k}} - \underbrace{\frac{\partial}{\partial r}\left(\frac{\overline{u_r p}}{\rho}\right)}_{D_{p,k}} - \underbrace{\frac{1}{r} \frac{\overline{p u_r}}{\rho}}_{D_{p,k}} + \underbrace{\nu \frac{1}{2r} \frac{\partial}{\partial r}\left(r \frac{\partial k}{\partial r}\right)}_{D_{v,k}} - \varepsilon_k \quad (3.43)$$

The only production term (P_k) is related to the streamwise velocity component. Energy redistribution to the two lateral components is due to the pressure-strain interaction (Π_{ij}), defined in Eq. 3.6 to 3.8. The measured production term is presented in Fig. 3.13. For comparison, the theoretical

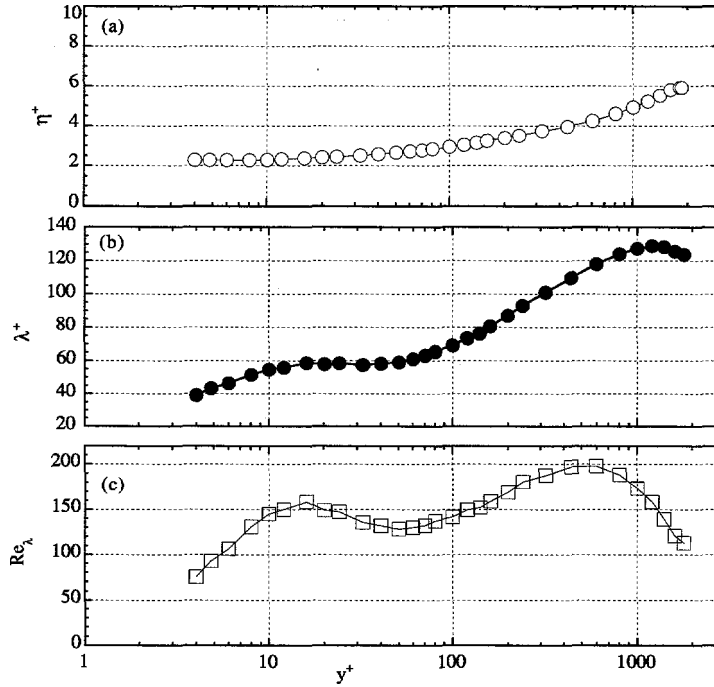


Figure 3.12: Kolmogorov micro scale η^+ (a), Taylor micro scale λ^+ (b), turbulent Reynolds number R_λ (c).

expression for the production rate,

$$P_k^+ = \left\{ \frac{r^+}{R^+} + \frac{\partial U_x^+}{\partial r^+} \right\} \frac{\partial U_x^+}{\partial r^+}, \quad (3.44)$$

is included. This expression is deduced from the analytical expression for the shear stress (Eq. 3.39), and $\partial U_x^+ / \partial r^+$ is calculated from the measured streamwise velocity distribution. The measured production rate compares well with the theoretical result, for $y/R > 0.1$. Near the wall the production rate seems to be underestimated, due to experimental error in the shear stress measurements. The theoretical curve produces a maximum at $y/R = 0.994$, which corresponds to $y^+ = 11$. This differs slightly from the position of maximum streamwise intensity ($y^+ = 14.7$). Since the production term enters

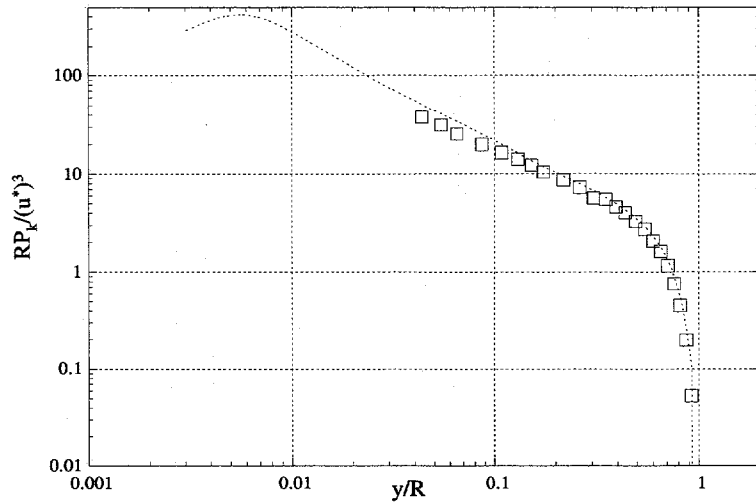


Figure 3.13: Production of turbulent kinetic energy, $RP_k/(u^*)^3$: Theoretical-Eq. 3.44 (dashed) : Measured (\square).

directly into the streamwise component, one would expect these two points to collapse.

Accurate determination of the dissipation rate was offered great attention. Based on measurements with a $1.27 \mu\text{m}$ diameter single-wire, detailed streamwise power spectra were obtained². The dissipation rate was estimated by the following three methods:

I

$$\varepsilon = \frac{15\nu}{U_x^2} \overline{\left(\frac{\partial u_x}{\partial t}\right)^2} \quad (3.45)$$

II

$$\varepsilon = 15\nu \int_0^\infty k_x^2 E_{xx}(k_x) dk_x \quad (3.46)$$

²The theory of turbulence spectra is described in chapter 4.

III

$$\varepsilon = \left[\frac{E_{xx}(k_x)(k_x)^{5/3}}{C_K} \right]^{3/2}, \quad (3.47)$$

where the Kolmogorov constant was taken as $C_K = 0.53$. The first and second method should theoretically give the same result, since they are separated only by a Fourier transform. Differences may be explained by numerical error, when differentiating, integrating or performing the Fourier transform of the time series. The results, presented in Fig. 3.14, show that the three methods compare well for $y/R > 0.1$. Close to the wall, the method of obtaining the dissipation rate from the inertial range gives higher values than the isotropic approach. These results must be questioned, since an inertial range is not obvious in the vicinity of the wall. The turbulent Reynolds number R_λ may be sufficiently high, but the separation between the energy containing and dissipative scales is clearly not sufficient. Method III is included in the budget for the kinetic energy, since it is believed to give the best overall accuracy. Looking at Fig. 3.15 it appears that Eq. 3.45 and 3.46 must be even more wrong, since the imbalance for $y/R \in [0.2, 0.8]$ indicates that ε is too small. In this range the influence of pressure- and viscous diffusion is assumed to be small.

The turbulent diffusion term, $(D_{t,k})$, involves gradients in the radial direction only, and must integrate to zero over the cross section. This term has the complete form:

$$-\frac{1}{r} \frac{\partial}{\partial r} \left[r(\overline{u_r u_x^2} + \overline{u_r^3} + \overline{u_r u_\theta^2}) \right] \quad (3.48)$$

The last term on the right hand side is not possible to obtain with the present experimental technique, since it only involves transverse velocity components. The most common way to estimate this triple correlation is

$$\overline{u_r u_\theta^2} = A \left[\overline{u_r^3} + \overline{u_r u_x^2} \right], \quad (3.49)$$

where $A = 1/2$, since the second order moment $\overline{u_\theta^2}$ is normally less than $\overline{u_x^2}$ and larger than $\overline{u_r^2}$. Inserted into Eq. 3.48, this gives the approximate relation for the turbulent diffusion as:

$$D_{t,k} = - \left\{ \frac{3}{4} \frac{1}{r} \frac{\partial}{\partial r} \left(r(\overline{u_r^3} + \overline{u_r u_x^2}) \right) \right\} \quad (3.50)$$

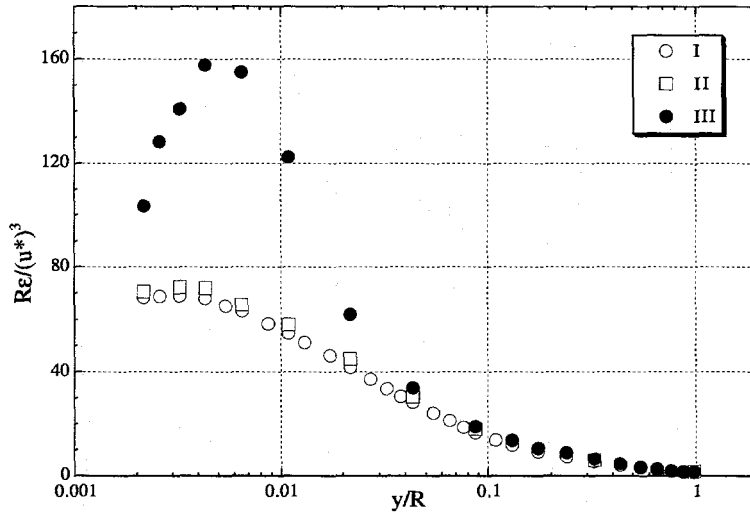


Figure 3.14: Dissipation of turbulent kinetic energy, $Re/(u^*)^3$, obtained from the three different methods described in the text.

The remaining terms which have not been discussed, are the viscous and pressure diffusion. DNS results [32] indicate that these terms are negligible outside the viscous sublayer. These terms are therefore not included in the budget.

Due to experimental uncertainty near the wall, the energy budget is presented in Fig 3.15 only for $y/R > 0.1$, corresponding to $y^+ > 180$. Each term is scaled with $(u^*)^3/R$. On the pipe centre line, the production term vanishes, due to the zero gradient of the streamwise velocity and the zero intersection of the shear stress. At this position the non-zero dissipation rate is balanced by the turbulent diffusion. The imbalance is negligible on the pipe centre line, and slightly positive throughout the layer. Close to the wall the imbalance increases, which is probably due to an underestimation of the dissipation rate.

3.5 Conclusion

Experimental results are reported for the two straight pipe sections, for $Re \in [22.000, 75.000]$. The static pressure drop along the pipe was linear

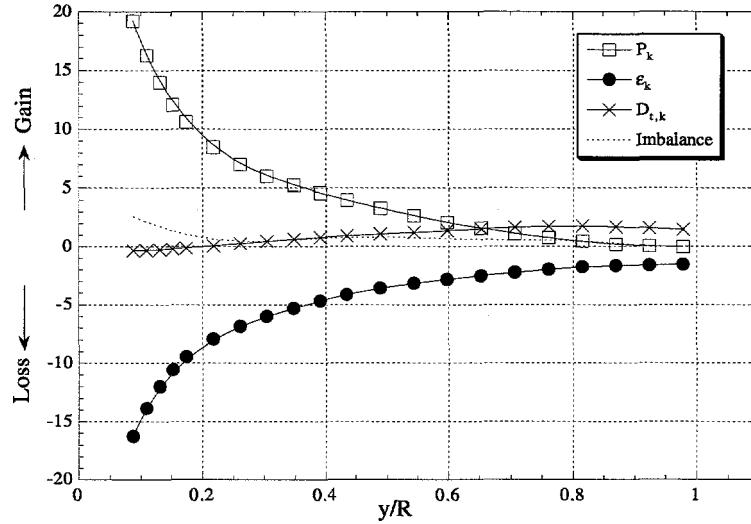


Figure 3.15: Balance of turbulent kinetic energy, made non-dimensional with the pipe radius and the friction velocity. $Re = 75.000$ in rig I. Pressure diffusion and viscous diffusion are not included.

beyond $x/D \simeq 15$. The pipe friction factor agreed with the classical relation of Prandtl for smooth pipes.

Circumferential homogeneity in the mean streamwise velocity and streamwise turbulence intensity is confirmed for both pipe rigs, independent of Reynolds number. The mean streamwise velocity was found to have a logarithmic wall region, with $\kappa = 0.41$ and $B = 5.5$.

The complete Reynolds stress tensor is reported for the different Reynolds numbers, and found consistent with previous results. Balance of the turbulent kinetic energy is reported for rig I, at $Re = 75.000$.

The intention of this verification, was to confirm that both pipe rigs produced a state of fully developed pipe flow. No evidence was found, which indicated a deviation from this state.

Chapter 4

Fourier Representation

This chapter presents the basic theory of power and cross-correlation spectra. Results are reported for the fully developed pipe flow described in the previous chapter ¹.

4.1 Power Spectrum

A general continuous time signal $f(t)$, may be expressed in terms of infinite series of sine and cosine functions, by use of the Fourier transform,

$$F(n) = \mathcal{F}\{f(t)\} = \frac{1}{T} \int_{-T/2}^{T/2} f(t) \exp(-int) dt, \quad (4.1)$$

where $\mathcal{F}\{\}$ denotes Fourier transform. The Fourier transform, $F(n) = \frac{1}{2}(a_n - ib_n)$, is a complex function of the frequency n , which may be represented by an amplitude spectrum,

$$|F(n)| = \frac{1}{2}(a_n^2 + b_n^2)^{1/2}, \quad (4.2)$$

and a corresponding phase spectrum,

$$\Theta(n) = \tan^{-1}\left(\frac{-b_n}{a_n}\right) \quad (4.3)$$

¹The theoretical background for turbulence spectra is taken from Frost and Moulden [23].

The amplitude spectrum represents the signal amplitude associated with the nth order harmonic. Introducing the autocorrelation function

$$R(\tau) = \frac{1}{T} \int_{-T/2}^{T/2} f(t)f(t+\tau) dt, \quad (4.4)$$

and the complex conjugate $F^*(n) = \frac{1}{2}(a_n + ib_n)$, the corresponding Fourier transform reads:

$$\mathcal{F}\{R(\tau)\} = F^*(n)F(n) = |F(n)|^2 \quad (4.5)$$

This is normally called the power spectral density of the signal $f(t)$, since it describes the energy associated with the nth harmonic.

If $f(t)$ is the instantaneous time signal for the fluctuating velocity component $u_i(t)$, such that

$$F_i(n) = \mathcal{F}\{u_i(t)\} = \frac{1}{T} \int_{-T/2}^{T/2} u_i(t) \exp(-int) dt, \quad (4.6)$$

the power spectrum reads,

$$E_{ii}(n) = F_i(n)F_i^*(n) = |F_i(n)|^2. \quad (4.7)$$

The indices $i=1,2$ or 3 represent the x , r and θ directions respectively, without summation over repeated indices. The single point time averaged velocity correlation tensor $R_{ij}(\tau)$ and the power spectrum $E_{ij}(n)$, then forms the Fourier transform pair,

$$E_{ij}(n) = \mathcal{F}\{R_{ij}(\tau)\} = \frac{1}{T} \int_{-T/2}^{T/2} R_{ij}(\tau) \exp(-i\tau n) d\tau, \quad (4.8)$$

where $R_{ij}(\tau)$ is the single point correlation tensor:

$$R_{ij}(\tau) = \frac{1}{T} \int_{-T/2}^{T/2} u_i(t, \mathbf{X}) u_j(t + \tau, \mathbf{X}) dt. \quad (4.9)$$

An important property of the power spectrum, is that its phase spectrum is always zero by definition. Equation 4.7 represents the energy contained in the $u_i(t)$ signal, such that

$$\int_0^\infty E_{ii}(n) dn = \overline{u_i^2}, \quad (4.10)$$

where repeated indices does not imply summation. The total turbulent kinetic energy $k = (\overline{u_i u_i})/2$ may be expressed as

$$k = \frac{1}{2} \int_0^\infty [E_{xx}(n) + E_{rr}(n) + E_{\theta\theta}(n)] dn = \frac{1}{2}(\overline{u_x^2} + \overline{u_r^2} + \overline{u_\theta^2}), \quad (4.11)$$

which means that all the turbulence energy is conserved into the three normal spectra. In the following text we will therefore denote E_{ij} for $i = j$ as power spectrum, and for $i \neq j$ as cross-correlation spectrum, described in section 4.2.

Since turbulence is three-dimensional, it is obvious that the spatial power spectrum must have a three-dimensional character. To obtain the complete form of this 3rd order (27 element) tensor, two-point space-time correlations of all three velocity components, in the three spatial directions are required. Experimentally, this is an almost impossible task. By assuming validity of the Taylor hypothesis, which is commonly called the “frozen flow” approximation, it is possible to measure the elements involving the streamwise wave number (k_x). Referring to the spatial separation vector (\mathbf{r}), visualized in Fig. 4.1, the component in direction of the unit vector \mathbf{e}_x may be expressed as,

$$r_x = \mathbf{e}_x \cdot \mathbf{r} \quad (4.12)$$

with the corresponding wave number component

$$k_x = \mathbf{e}_x \cdot \mathbf{k} \quad (4.13)$$

The streamwise one-dimensional spatial power spectra can then be expressed as:

$$E_{ij}(k_x) = \mathcal{F}\{Q_{ij}(r_x)\} = \frac{1}{L} \int_{-L/2}^{L/2} Q_{ij}(r_x) \exp(-ir_x k_x) dr_x, \quad (4.14)$$

where the spatial correlation tensor reads:

$$Q_{ij}(r_x) = \overline{u_i(t, \mathbf{X}) u_j(t, \mathbf{X} + r_x \mathbf{e}_x)}. \quad (4.15)$$

Lai et al. [35] measured the wave number spectra in fully developed pipe flow from space-time correlations. The results were found to be consistent with Taylor hypothesis. Applied to the streamwise spectrum, the hypothesis gives

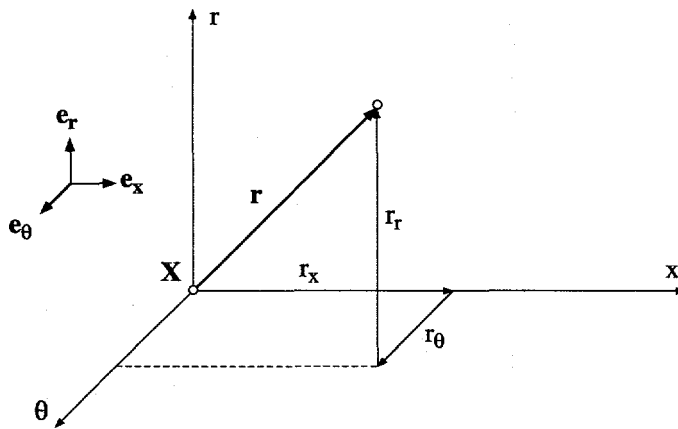


Figure 4.1: Spatial separation

the relation between the frequency spectra and the one-dimensional spatial power spectra:

$$E_{ij}(k_x) = \frac{U_x}{2\pi} E_{ij}(n) \quad ; \quad k_x = \frac{2\pi}{U_x} n \quad (4.16)$$

where k_x is the streamwise wave number, and U_x is the local mean streamwise velocity. This classical Taylor hypothesis suggests that the convection velocity (U_c) is equal to U_x , and constant for all scales. This may seem like a crude approximation, since it is not obvious that the large and the small scales are convected at the same rate. A detailed study of the convection velocity in a low Reynolds number turbulent boundary layer was reported by Krogstad et al. [34]. They found the convection velocity for the smaller scales to be lower than for the larger scales. In general the convection velocity deduced from two-point correlations was lower than the local mean velocity (U_x). A modified Taylor hypothesis (see e.g. Browne et al. [12] ; Kahalerras et al. [29]) has been formulated as a function of the instantaneous streamwise

velocity ($\tilde{U}_x(t)$), such that

$$\delta x = -\tilde{U}_x(t)\delta t \quad (4.17)$$

Browne et al. found no significant difference when applying this alternative form of space-time conversion to temperature derivatives. Deviation between the classical and modified hypothesis, is closely related to the turbulence intensity. If the intensity is low, the instantaneous streamwise velocity is approximately equal to the mean streamwise velocity, thus both time-space conversions should give the same result. In the present work the convection velocity is consequently taken as the local mean streamwise velocity, which is based on the findings of Lai et al. mentioned earlier.

The spectra may be made non-dimensional with a characteristic length scale (ℓ) and velocity scale (ϑ) such that,

$$\frac{\Phi_{ij}(\ell k_x)}{\vartheta^2} = \frac{U_x}{2\pi\ell} E_{ij}(n) \quad ; \quad \ell k_x = \frac{2\pi\ell}{U_x} n \quad (4.18)$$

Selection of the scaling parameters will emphasize certain similarity properties of the spectra. Often the velocity scale is taken as the integral of $E_{ij}(k_x)$, such that $\Phi_{ij}(\ell k_x)$ integrates to unity. The length scale is normally taken as the pipe radius (R), the distance from the pipe wall (y), the Taylor micro scale (λ) or the Kolmogorov length (η).

4.1.1 The spectral energy cascade

The classical picture of turbulence is described by cascades of eddies of different size, where energy is injected from the mean flow into the largest scales, and drained by viscous strain in the smallest scales.

The first hypothesis of Kolmogorov postulated that the smallest turbulent scales, called the dissipative scales, are statistically steady, isotropic and independent of the large scale characteristics. This means that the smallest scales are solely determined by the fluid viscosity (ν) and the dissipation rate (ε). Kolmogorov restricted the postulate to "large" turbulent Reynolds number (R_λ), such that the large energy containing scales are widely separated from the dissipative scales. The hypothesis implies that the smallest scales of the power spectrum must scale universally with the viscosity (ν) and the Kolmogorov length scale ($\eta = (\nu^3/\varepsilon)^{1/4}$), independent of the flow geometry and degree of large scale anisotropy. In the following sections this

will be described as Kolmogorov scaling. The hypothesis has been confirmed experimentally by several authors, for a number of laboratory and geophysical flows (see Champagne [15]). Kim and Antonia [31] also found support for small scale isotropy in direct numerical simulations of fully developed channel flow, at turbulent Reynolds numbers as low as $R_\lambda = 53$. They concluded that even in the absence of an inertial subrange, described in the following text, the dissipative scales were close to isotropic. On the channel centre line ($R_\lambda = 53$), agreement with isotropy was found for the wave number range $0.03 < \eta k_x < 1$. Small scale isotropy is commonly referred to as local isotropy, where "local" refers to the high wave number range, not to be confused with local in space. Local isotropy is one of the corner stones in turbulence modelling, such as two-equation models ($k\text{-}\varepsilon$), Reynolds Stress Models and Sub-Grid Scale models. Experimental verification has been, and still is of utmost importance.

In 1941 Kolmogorov posed the following hypothesis for the intermediate range between the large energy containing scales and the small dissipative scales:

"If the Reynolds number is infinitely high, the power spectrum in the inertial range is only a function of the dissipation rate and the local wave number"

This has been regarded as one of the well founded theories of turbulence. Simply from dimensional analysis, Kolmogorov obtained the inertial form of the power spectrum, which for the streamwise component reads:

$$E_{xx}(k_x) = C_K \varepsilon^{2/3} k_x^{-5/3} \quad (4.19)$$

The Kolmogorov constant, C_K , is assumed universal, which will be discussed later. The inertial hypothesis suggests that there is a range in the power spectrum which is unaffected by turbulent production and viscous dissipation. That is a wave number range where both the production spectrum and the dissipation spectrum are small. The energy is transferred through the inertial range, and dissipated at higher wave numbers. This requires that the interaction between scales is local in wave number space. Energy is not allowed to be transferred directly from the energy containing scales to the inertial scales, and the inertial scales must be too large for viscous dissipation to occur. Thus existence of an inertial range requires sufficient separation of energy containing ($k_{x,e}$) and dissipative ($k_{x,d}$) scales, such that $k_{x,e} \ll k_{x,d}$. The wave numbers $k_{x,e}$ and $k_{x,d}$ may be taken as the wave numbers of the

maximum in the streamwise power spectrum and dissipation spectrum respectively.

By visual inspection of the streamwise spectrum one can easily find a range in the power spectrum which applies to the (-5/3) slope, even for $R_\lambda < 100$. However for low R_λ this range is very narrow. The question is whether this is a "true" inertial range, or just a range which appears similar. It should therefore be of interest to examine the separation of $k_{x,e}$ and $k_{x,d}$ as function of the turbulent Reynolds number, to determine if an inertial range is possible or not.

The peak of the dissipation spectrum $D(k_x) = k_x^2 E_{xx}(k_x)$ is for a number of experiments found to be located within $\eta k_{x,d} = 0.1 - 0.2$ [15], irrespective of R_λ . The energy containing wave number may be estimated by [25]:

$$\eta k_{x,e} = \frac{15^{3/4}}{A(R_\lambda)^{3/2}} \quad (4.20)$$

Hinze [25] suggested that the scaling constant A was of order unity. Present results gave an average value of $A = 1.7$, for $R_\lambda \in [54, 198]$, which is consistent with Hinze. The number of decades of separation can then be expressed as,

$$N = \log \left(\frac{k_{x,d}}{k_{x,e}} \right) \quad (4.21)$$

Figure 4.2 shows a tentative extrapolation of $N(R_\lambda)$, based on $A = 1.7$ and $\eta k_{x,d} = 0.1$. To achieve $N = 1, 2$ or 3 , this requires approximate values of $R_\lambda \simeq 55, 270$ and 1250 respectively. Obviously the inertial range is allowed to span only a small partition of this separation. If $k_{x,e}$ is only one decade lower than $k_{x,d}$, existence of an inertial range does seem possible, which was also supported by DNS results of Kim and Antonia [31] for $R_\lambda = 53$. Lawn [36] suggested that $R_\lambda = 140$ should be sufficient for appearance of an inertial range. Bradshaw (see Lawn) suggested $R_\lambda = 100$ as a sufficient value. According to Fig. 4.2 this gives $N = 1.6$ and 1.3 respectively, which means that a possible inertial range is allowed to span only a very narrow region. In contradiction to these statements, recent analytical work by Bowman [9], suggests that many decades of separation are needed for a "true" inertial range to exist. This conclusion was drawn from numerical experiments. Sadoughi [53] reported one decade of isotropic inertial range for $R_\lambda = 2000$, in a non-equilibrium shear layer.

Perry and Abell [49] investigated the spectral energy cascade in fully developed smooth and rough pipe flow, and found that the spectral behaviour

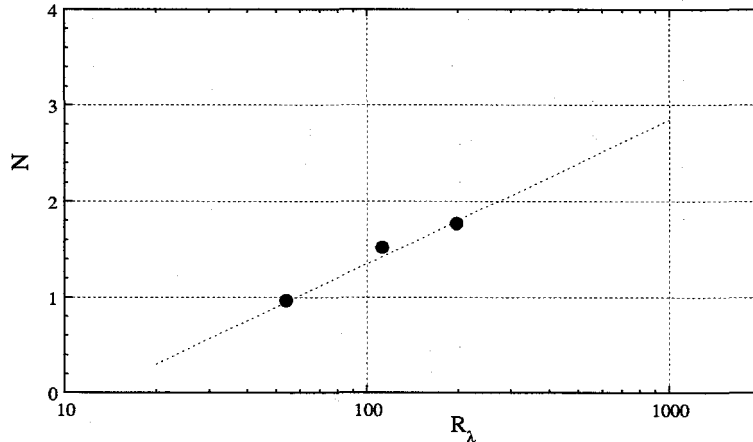


Figure 4.2: Separation energy containing and dissipative scales; $N = \log\left(\frac{k_{x,d}}{k_{x,c}}\right)$. Present Results(●).

of the large scales in a narrow wall region, was proportional to k_x^{-1} . This was called the hypothesis of universal wall structure. They suggested this range to be limited by $y^+ > 100$ and $y/R < 0.1$, which coincide with the logarithmic wall region. The appearance of a -1 range was related to the local (in space) balance between the turbulence production and the dissipation rate.

4.1.2 Measured streamwise power spectra

Detailed streamwise power spectra were measured in pipe rig I, at a bulk Reynolds number of $Re = 75.000$. Time series were obtained with a $1.27\mu\text{m}$ diameter single hot-wire probe. A partially etched Platinum-10% Rhodium wire, with an active length to diameter ratio of $l_w/d_w = 200$, was used. The cut-off frequency was decided from the power spectrum of an unfiltered signal, and set to $n_c = 15$ kHz. The sampling frequency was set to $n_s = 33$ kHz, according to the Nyquist criteria. The sampling time was $t_s = 25$ s, which gives a continuous time series of $N = 825.000$ data. The number of spectral points in the fast Fourier transform was 2^{12} , which means that the spectra are calculated from an average of 200 windows. The turbulence spectra were transformed from frequency to wave number space by use of Eq. 4.16.

Figure 4.3 shows the measured streamwise power spectrum, for different

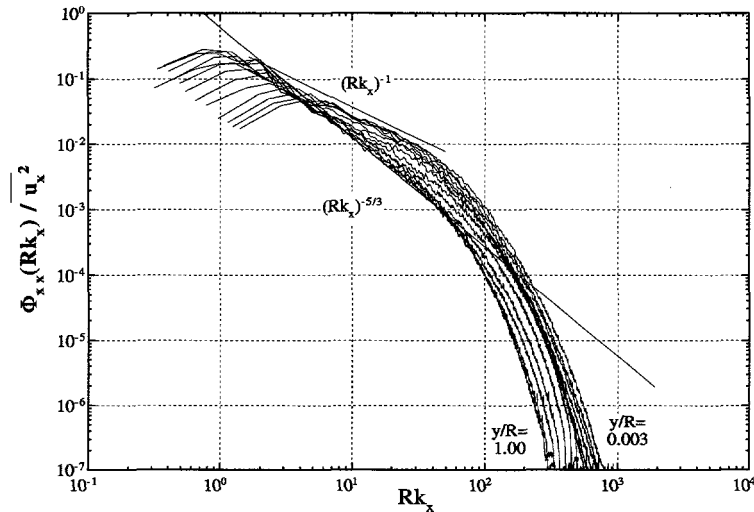


Figure 4.3: Streamwise power spectra, $\Phi_{xx}(Rk_x)/\bar{u}_x^2$, in fully developed pipe flow; $0.003 \leq y/R \leq 1$; $Re = 75.000$.

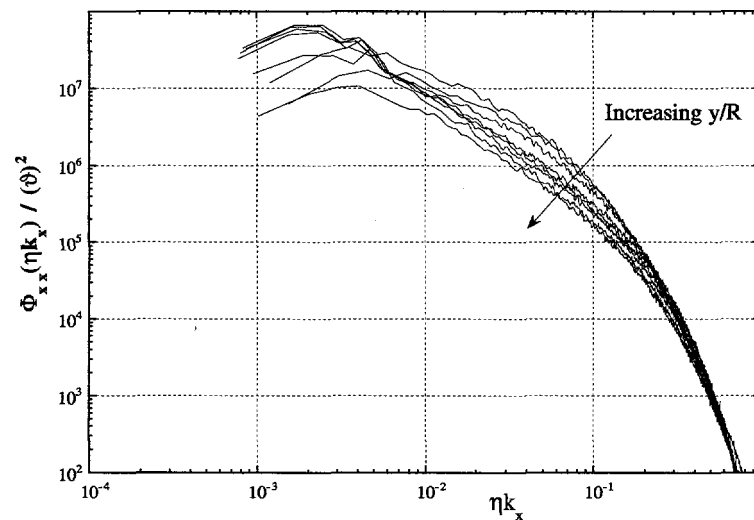


Figure 4.4: Streamwise power spectra, $\Phi_{xx}(k_x \eta)/\theta^2$, in fully developed pipe flow; $0.003 \leq y/R \leq 1$; $Re = 75.000$.

locations restricted by $y^+ > 5$ ($y/R = 0.003$) and $y/R = 1$, that is from the pipe wall towards the centre line. The spectra are presented on the non-dimensional form: $\Phi_{xx}(Rk_x)/\bar{u}_x^2 = E_{xx}(k_x)/(Ru_x^2)$, as a function of the non-dimensional wave number Rk_x . The integral of the spectra relates as

$$\frac{1}{\bar{u}_x^2} \int_0^\infty \Phi_{xx}(Rk_x) d(Rk_x) = 1, \quad (4.22)$$

thus represents the relative spectral distribution. The spectral energy distribution is shifted towards higher wave numbers, when approaching the wall. The $-5/3$ inertial subrange is included for comparison. Only the locations near the centre line has a narrow region which applies to this range. The turbulent Reynolds number on the centre line was $R_\lambda = 112$. The corresponding separation of $k_{x,e}$ and $k_{x,d}$ was approximately 1.5 decades. "By best intention" the spectra may be said to follow the inertial range for half a decade. However it will be shown later that several of the basic restrictions for an inertial range are violated.

Figure 4.4 shows a selection of the same spectra, scaled with the Kolmogorov length (η) and velocity (ϑ), such that $\Phi_{xx}(\eta k_x)/\vartheta^2 = E_{xx}(k_x)/(\eta \vartheta^2)$. The integral of the spectra then relates as

$$\frac{1}{\vartheta^2} \int_0^\infty \Phi_{xx}(\eta k_x) d(\eta k_x) = \frac{\bar{u}_x^2}{\vartheta^2}. \quad (4.23)$$

The spectra now collapse in the very high wave number range, when approaching $\eta k_x = 1$. This supports that the high wave number range is solely determined by the viscosity (ν) and the dissipation rate (ε), which is consistent with the first hypothesis of Komogorov. It should be kept in mind that the high wave number range is the most difficult to obtain accurately, due to signal noise and spatial averaging. On the pipe centre line the ratio of the active wire length to the Kolmogorov length was $l_w/\eta = 1.7$, and at $y/R = 0.1$ the corresponding ratio was 2.8. The size of the measuring volume should therefore be sufficiently small to capture even the highest wave numbers. As can be seen from Fig. 4.3, more than six decades of energy level is obtained, without contamination of electronic noise. The signal was sampled by use of a twelve bit analog to digital converter, which supports 4096 different discrete values. The only way to achieve sufficient resolution of the smallest scales, was to maximize the amplification for each time series. The high wave number range is therefore believed to be very accurate. No corrections have been applied to the spectra.

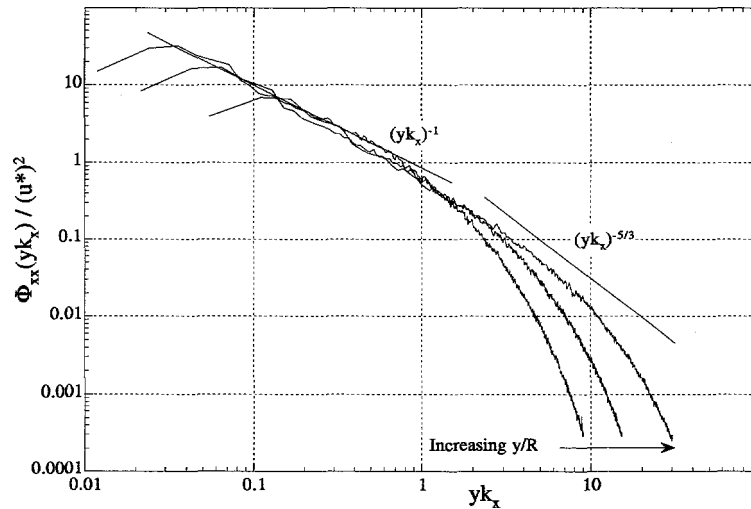


Figure 4.5: Streamwise power spectra, $\Phi_{xx}(yk_x)/(u^*)^2$ in fully developed pipe flow; $40 < y^+ < 240$; $Re = 75.000$.

To examine what Perry and Abell [49] described as the hypothesis of universal wall structure, Fig. 4.5 shows the streamwise spectra normalized with the local distance from the wall and the wall friction velocity: $\Phi_{xx}(yk_x)/(u^*)^2 = E_{xx}(k_x)/[y(u^*)^2]$. The locations of the spectra are $y^+ = 40, 80$ and 240 , which corresponds to the inner part of the logarithmic wall region. Only the spectra presented in the figure corresponded to some extent with the k_x^{-1} range. However more than one decade of wave numbers followed this range. The result supports the findings of Browne and Dinkelacker [14], who obtained a similar range for $y^+ = 100$ at $Re = 66.400$.

4.1.3 Measured lateral power spectra

Lateral power spectra were obtained with a $2.5 \mu\text{m}$ diameter cross-wire, for the same experimental condition as for the streamwise spectra described in the previous section. The active wire length to diameter ratio was $l_w/d_w = 200$. The cut-off frequency was $n_c = 10 \text{ kHz}$, and the sampling frequency $n_s = 20 \text{ kHz}$.

Figure 4.6 shows the radial spectra, and Fig. 4.7 the circumferential spec-

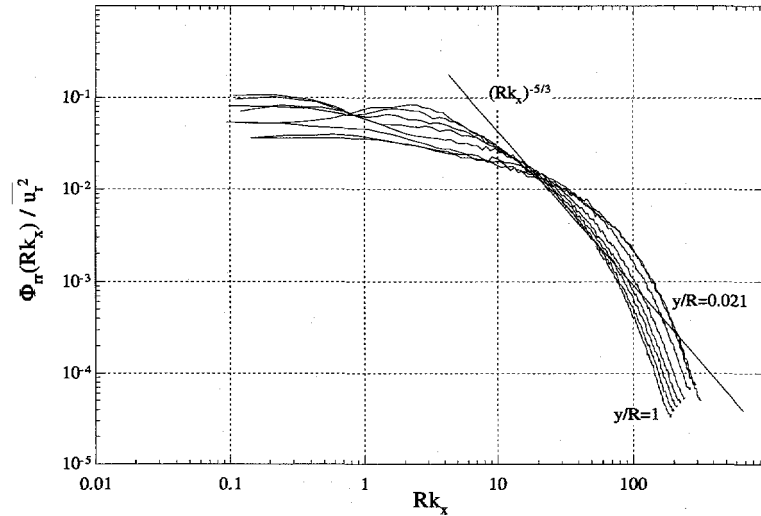


Figure 4.6: Radial power spectra in fully developed pipe flow; $Re = 75.000$: Outer scaling: $\Phi_{rr}(Rk_x)/\bar{u}_r^2$. $0.021 \leq y/R \leq 1$.

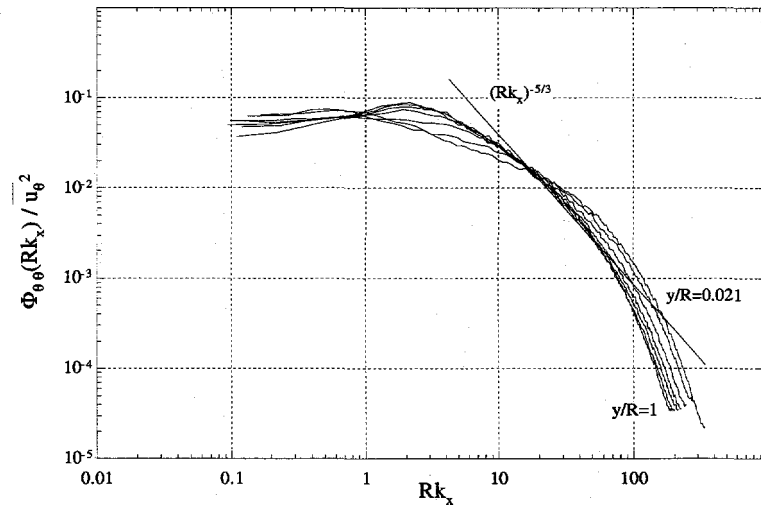


Figure 4.7: Circumferential power spectra in fully developed pipe flow; $Re = 75.000$: Outer scaling: $\Phi_{θθ}(Rk_x)/\bar{u}_θ^2$. $0.021 \leq y/R \leq 1$.

tra, in the non-dimensional form: $\Phi_{rr}(Rk_x)/\bar{u}_r^2$ and $\Phi_{\theta\theta}(Rk_x)/\bar{u}_{\theta}^2$, such that

$$\frac{1}{\bar{u}_r^2} \int_0^\infty \Phi_{rr}(Rk_x) d(Rk_x) = \frac{1}{\bar{u}_{\theta}^2} \int_0^\infty \Phi_{\theta\theta}(Rk_x) d(Rk_x) = 1 \quad (4.24)$$

The locations of the spectra are limited to $0.021 \leq y/R \leq 1$. Both the circumferential and radial spectra obtain a crest near $Rk_x = 2$, when moving towards the centre line. However this crest persist in the circumferential spectra at distances closer to the wall than the radial spectra. On the centre line the two radial spectra must collapse. Since no production of turbulence enter directly into the lateral components, the difference in the two lateral spectra must be related to differences in the pressure-strain interaction. The spectra are also compared to the inertial $-5/3$ range of Kolmogorov. The presence of an inertial range in the streamwise spectrum does not require an inertial range in the lateral spectra. However, if the lateral spectra relate to such a range, the inertial scales are bound to be isotropic. By introducing Eq.4.19 into Eq.4.26, it is straight forward to obtain:

$$E_{rr}^o(k_x) = E_{\theta\theta}^o(k_x) = \frac{4}{3} C_K \varepsilon^{2/3} k_x^{-5/3} \quad (4.25)$$

Existence of a lateral inertial range is expected to coincide with the same inertial scales obtained in the streamwise spectra. Looking at Fig. 4.8, this does not seem to be the case. It will be shown in the following text that for the present Reynolds number, what appears as an inertial range is not sufficiently separated from the production scales. Since the production is not isotropic, it is reasonable to assume that all scales which are influenced by production can not be isotropic. This is in disfavour of a lateral inertial range. Figure 4.8 and 4.9 show the three power spectra at the pipe centre line and at $y/R = 0.3$. The spectra are made non-dimensional with the friction velocity, thus the spectra do integrate to $\bar{u}_i \bar{u}_j^+$. For comparison in the high wave number range, the isotropic lateral spectrum $E_{rr}^o(k_x)$ calculated from the isotropic relation [25]:

$$E_{rr}^o(k_x) = E_{\theta\theta}^o(k_x) = \frac{1}{2} \left[E_{xx}(k_x) - k_x \frac{\partial E_{xx}(k_x)}{\partial k_x} \right], \quad (4.26)$$

has been included in the figure. To reduce scatter, $E_{xx}(k_x)$ was fitted to a n 'th order polynomial (see Kim and Antonia [31]),

$$\ln [E_{xx}(k_x)] = c_0 + c_1(\ln k_x) + c_2(\ln k_x)^2 + \dots + c_n(\ln k_x)^n \quad (4.27)$$

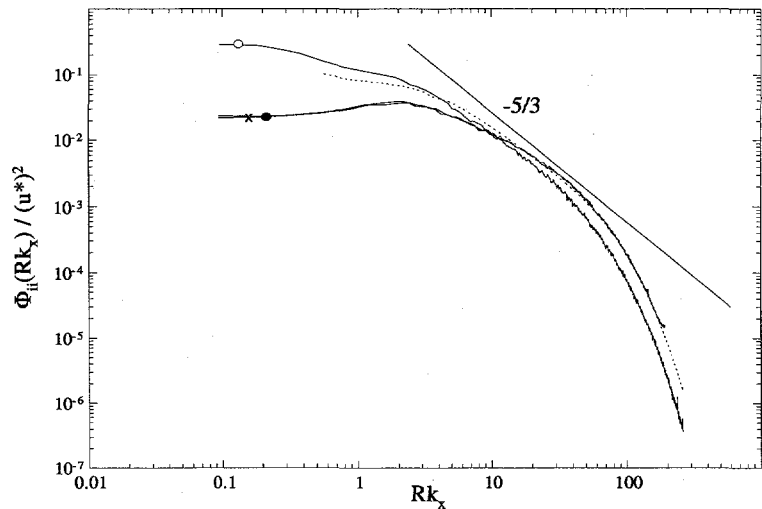


Figure 4.8: Power spectra for the streamwise (\circ), radial (\bullet) and circumferential (\times) component, in fully developed pipe flow; $Re = 75.000$; $y/R = 1$; Isotropic lateral spectra (dotted).

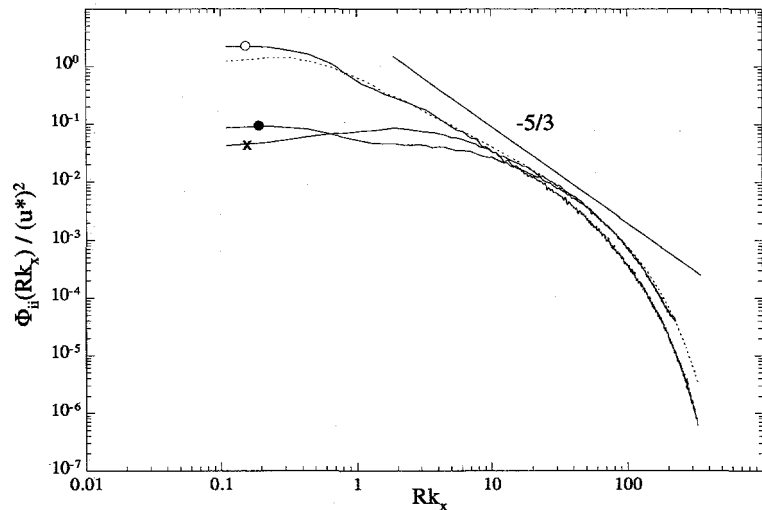


Figure 4.9: Power spectra for the streamwise (\circ), radial (\bullet) and circumferential (\times) component, in fully developed pipe flow; $Re = 75.000$; $y/R = 0.3$; Isotropic lateral spectra (dotted).

before differentiating. On the centre line the two lateral spectra must be identical for all wave numbers, due to the axisymmetry, which is seen to correspond well with the measured spectra. For both locations, the two lateral spectra closely follow the isotropic spectral distribution in the high wave number range. This indicates that the small scales tend towards isotropy. It should be noted that Eq. 4.26 requires that the streamwise spectrum is isotropic. One should therefore be careful to conclude that all scales which correspond to $E_{rr}^o(k_x) = E_{rr}(k_x)$ are isotropic. Figure 4.9 indicates that the crest in the circumferential spectrum persist closer to the wall compared to the radial spectrum. This indicates that the redistribution from the streamwise to the lateral spectra is preferred towards the circumferential component when approaching the wall. Saddoughi [53] suggested that the inertial range was first established in the streamwise component, followed by the circumferential component, and finally the wall-normal component. This result was obtained in a rough surface boundary layer, in a large scale wind tunnel. The conclusions are supported by the present results.

Spectral corrections due to high turbulence intensity, causing deviation from the Taylor hypothesis, has been described by Champagne [15]. The correction was initially suggested by Lumley [41], formulated as a differential equation for the spectra, including the individual normal components of the Reynolds stress tensor. Wyngaard and Clifford [65] suggested an extended version of the Lumley correction. For the pipe centre line, the streamwise intensity was as low as $(\overline{u_x^2})^{1/2}/U_x = 0.035$, and the lateral intensities were $(\overline{u_r^2})^{1/2}/U_x = 0.027$. Thus the above corrections had no visible effect on the spectra. A more relevant question is the experimental resolution, causing misinterpretation of the high wave number range. As described in section 4.1.2, the streamwise spectra, which are measured with a miniature single-wire, are assumed to be very accurate. For the cross-wire experiments the wire length and spacing were approximately three times the Kolmogorov length. This may cause spatial averaging for $\eta k_x > 0.3$, which is beyond the wave number of maximum dissipation rate. Referring to Fig. 4.6 and Fig. 4.7, this corresponds to $Rk_x > 100$. A possible error will cause an attenuation of the highest wave numbers, due to spatial averaging. However for the lower wave numbers the lateral spectra are assumed to be accurate.

4.2 Cross-correlation Spectrum

If u_i and u_j are velocity fluctuations in two different directions, the cross correlation, which applies to Eq. 4.9, has the corresponding Fourier transform pair given by Eq. 4.8. If $F(n) = a_n - ib_n$ is the complex Fourier transform of $u_i(t)$ and $G(n) = c_n - id_n$ is the corresponding transform of $u_j(t)$, the cross-correlation spectrum may be expressed as the real part of the product

$$G^*(n)F(n) = \underbrace{a_n c_n + b_n d_n}_{Re} + i \underbrace{(a_n d_n - b_n c_n)}_{Im}, \quad (4.28)$$

such that

$$E_{ij} = Re [G^*(n)F(n)], \quad (4.29)$$

for $i \neq j$, and Re denotes the real part of the complex product. The cross-correlation spectra represent spectral correlations, rather than spectral energy distribution. In fully developed pipe flow, the only non-zero cross-correlation spectrum is $E_{xr}(k_x)$, which relates to the Reynolds shear stress as

$$\overline{u_x u_r} = \int_0^\infty E_{xr}(k_x) dk_x \quad (4.30)$$

The only production term which enter the transport equations for fully developed pipe flow is

$$P_{xr} = -\overline{u_x u_r} \frac{\partial U_x}{\partial r}, \quad (4.31)$$

such that the corresponding production spectrum may be expressed as:

$$P_{xx}(k_x) = -\frac{\partial U_x}{\partial r} E_{xr}(k_x) \quad (4.32)$$

Tennekes and Lumley [60] suggested that the production spectrum may be expressed in terms of the streamwise power spectrum as

$$P_{xx}(k_x) = -A \frac{S^2}{\varepsilon^{1/3}} k_x^{-2/3} E_{xx}(k_x), \quad (4.33)$$

where A is a constant and $S = (\partial U_x / \partial r)$. This means that the cross correlation spectra must decrease at a faster rate than the streamwise power spectra with increasing wave number. It follows from Eq. 4.33 and Eq. 4.19 that the inertial range behaviour of the production spectra must be proportional to $k_x^{-7/3}$. It is clear however that the value of the production spectrum must be small in this range, since the effect of production should be negligible here.

4.2.1 Measured cross-correlation spectra

Cross-correlation spectra are calculated from the same set of data as the lateral spectra. Figure 4.10 presents $E_{xr}(k_x)$, scaled with the pipe radius (R), and the local Reynolds shear stress $\overline{u_x u_r}$, such that $\Phi_{xr}(Rk_x)/\overline{u_x u_r}$ integrates to unity. The locations of the spectra are limited to $0.021 < y/R < 0.44$. When approaching the centre line, the shear stress $\overline{u_x u_r}$ drops to zero, which is reflected by a decrease in the spectral correlation. On the centre line $E_{xr}(k_x)$ should theoretically be zero. The measured spectrum showed large scatter. Spectral values of both sign were obtained, which is possible since the real part of Eq. 4.28 may be both positive and negative. Since the spectral correlation should be practically zero, the near centre line locations are not included. The presented spectra are compared to the $-7/3$ inertial range, suggested by Tennekes and Lumley [60]. Only the locations far from the pipe wall exhibits in some extent such a range. It is clear however that the spectral correlation level must stay small, to avoid violation of the basic assumptions for an inertial range.

Saddoughi and Veeravalli [53] suggested $\varepsilon^{1/2} S^{-3/2}$ and $\varepsilon^{1/2} S^{-1}$ as proper length and velocity scales for the cross correlation spectra. This scaling has been successfully applied to the present results, shown in Fig. 4.11. The locations of the spectra are restricted to $0.087 < y/R < 0.44$, where the spectra are seen to collapse for almost the entire wave number region. For the locations closer to the wall, the spectra deviated from this scaling, which is possibly related to error in the dissipation rate (ε). Different methods for determining ε gave the same result outside $y/R = 0.1$, which supports an accurate scaling in this region. The cross-correlation spectra follow only "by best intention" the $-7/3$ range suggested by Tennekes and Lumley. This is possibly due to insufficient R_λ .

Figure 4.12 shows the integral function of the production spectrum,

$$\Upsilon_p(k_x) = \frac{1}{\overline{u_x u_r}} \int_0^{k_x} E_{xr}(k_x) dk_x \quad (4.34)$$

normalized with the total production rate. When approaching the wall a larger portion of the turbulence production is shifted towards the dissipative range. For $y/R = 0.44$ the production is negligible beyond $\eta k_x \simeq 0.1$, which corresponds to the maximum of the dissipation rate spectrum. Note that the core region ($y/R > 0.44$) is not presented. However when moving towards the centre line the turbulence production is shifted towards larger scales,

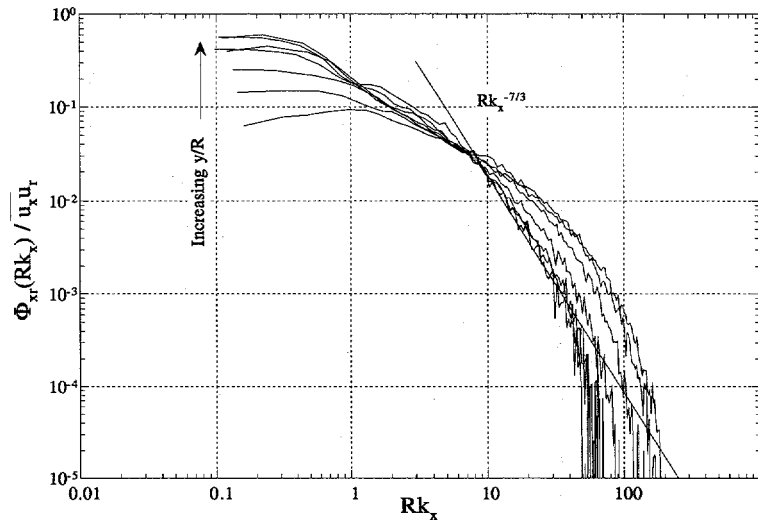


Figure 4.10: Cross-correlation spectra in fully developed pipe flow; $Re = 75.000$;
 $\Phi_{xr}(Rk_x)/\bar{u}_x \bar{u}_r$; $0.021 < y/R < 0.44$.

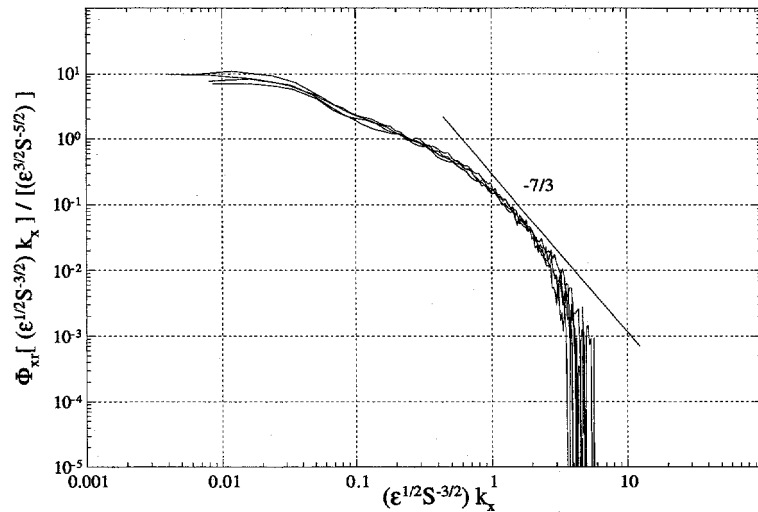


Figure 4.11: Cross-correlation spectra in fully developed pipe flow; $Re = 75.000$;
 $\Phi_{xr} ([\varepsilon^{1/2} S^{-3/2}] k_x) / [\varepsilon^{3/2} S^{-5/2}]$; $0.021 < y/R < 0.44$.

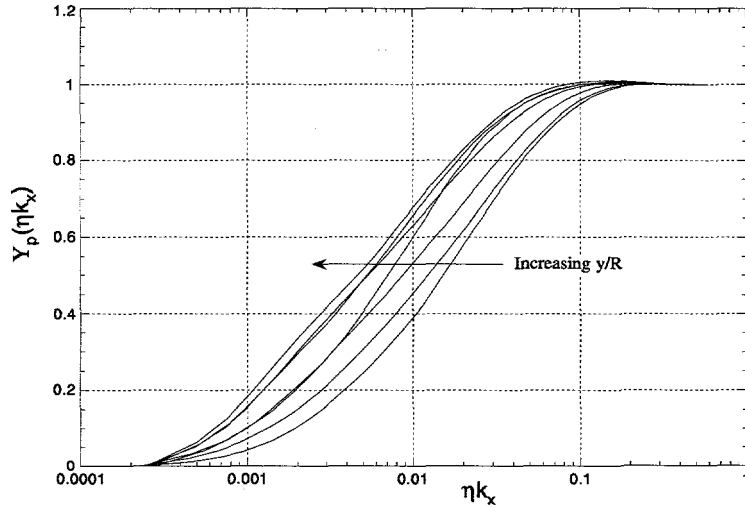


Figure 4.12: Integral function of the production spectrum in fully developed pipe flow, at the locations $0.021 < y/R < 0.44$; $\Upsilon_p(\eta k_x) = \frac{1}{\bar{u}_x \bar{u}_r} \int_0^{k_x} E_{xr}(k_x) dk_x$.

which supports the presence of an inertial range in this region.

4.3 Dissipation Spectrum

The isotropic expression for the dissipation rate,

$$\varepsilon_{iso} = 15\nu \overline{\left(\frac{\partial u_x}{\partial x} \right)^2}, \quad (4.35)$$

can be expressed in terms of the one-dimensional dissipation spectrum:

$$D_{xx}(k_x) = 15\nu k_x^2 E_{xx}(k_x), \quad (4.36)$$

such that:

$$\int_0^\infty D_{xx}(k_x) dk_x = \varepsilon_{iso} \quad (4.37)$$

The measured dissipation spectra are shown in Fig. 4.13, scaled with the Kolmogorov length (η) and velocity (ϑ) which gives the non-dimensional

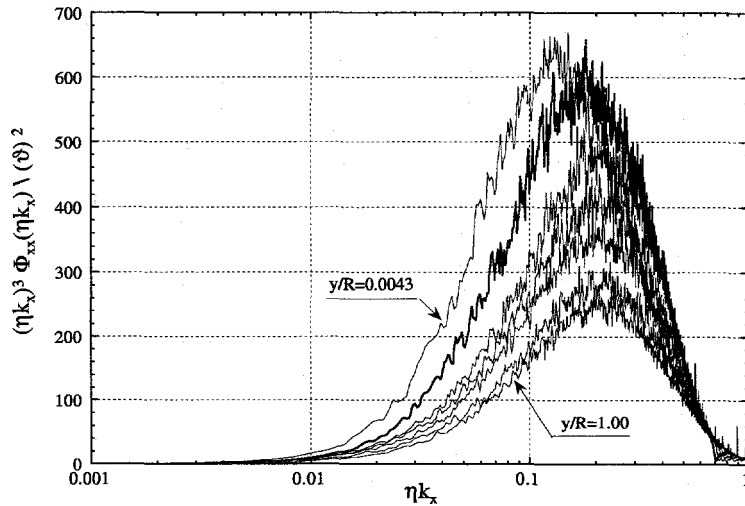


Figure 4.13: Dissipation rate spectrum in fully developed pipe flow ; $(\eta k_x)^3 \Phi_{xx}(\eta k_x) / \vartheta^2$; $Re = 75.000$

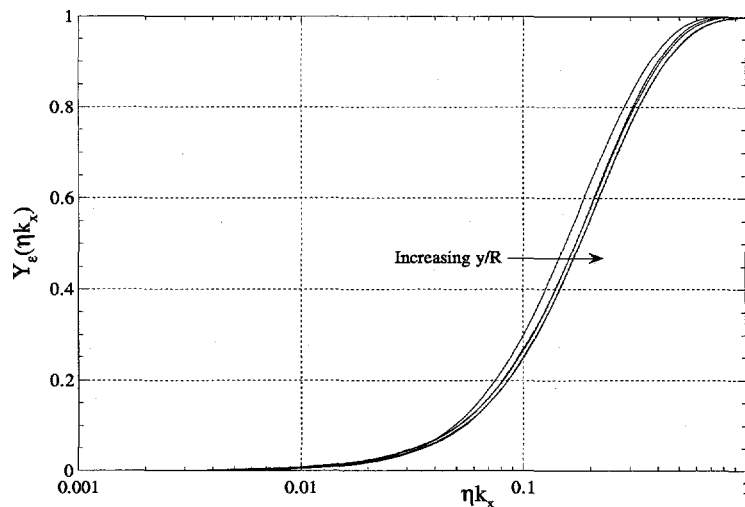


Figure 4.14: Integral function of dissipation rate spectrum in fully developed pipe flow, $\Upsilon_\varepsilon(k_x) = \left\{ 15\nu \int_0^{k_x} k_x^2 E_{xx}(k_x) dk_x \right\} / \varepsilon$, for $0.022 < y/R < 1$; $Re = 75.000$.

form: $(\eta k_x)^3 \Phi_{xx}(\eta k_x) / \theta^2$. Thus the area under each graph indicates the total dissipation rate. The peak of the dissipation spectra occur in the range $\eta k_x \in [0.1, 0.2]$, with a slight shift in ηk_x towards smaller wave numbers when approaching the wall. The location closest to the wall represents $y/R = 0.0043$ ($y^+ = 8$). This is inside the region where large discrepancies were found between the different methods for obtaining the dissipation rate. The dissipation rate in the inner region is likely to be underpredicted.

Figure 4.14 shows the integral function of Eq. 4.36,

$$\Upsilon_\varepsilon(k_x) = \frac{1}{\varepsilon} \left\{ 15\nu \int_0^{k_x} k_x^2 E_{xx}(k_x) dk_x \right\}, \quad (4.38)$$

normalized with the total dissipation rate. The result is plotted against ηk_x , and the variation with y/R is seen to be small. The effect of dissipation is insignificant for $\eta k_x < 0.01$. At $\eta k_x = 0.1$, more than 20% of the total dissipation has occurred.

4.3.1 Dissipation rate from inertial subrange

One of the features of the Kolmogorov hypothesis, is that it offer an alternative method of obtaining the dissipation rate from the measured turbulence spectrum. The major advantage of determining the dissipation rate from the inertial range, is that only moderate wave numbers need to be accurately measured. Lack of small scale resolution is therefore less crucial. Rearranging Eq 4.19, the dissipation rate reads:

$$\varepsilon = \left(\frac{k_x^{5/3} E_{xx}(k_x)}{C_K} \right)^{3/2} \quad (4.39)$$

Universality of the Kolmogorov constant (C_K) has been a subject of discussion. Praskovsky and Oncley [50] stated that variation in C_K was due to small scale intermittency. This conclusion was based on experiments in a large wind tunnel. Different values of the Kolmogorov constant (C_K) are reviewed by Sreenivasan [58], who reported values of $C_K = 0.53 \pm 0.055$, for a wide range of experiments and Reynolds numbers. A detailed study of the dissipation rate in fully developed pipe flow was reported by Lawn [36], suggesting $C_K = 0.53$. The Kolmogorov constant for the three-dimensional power spectrum has been examined on basis of numerical experiments, such

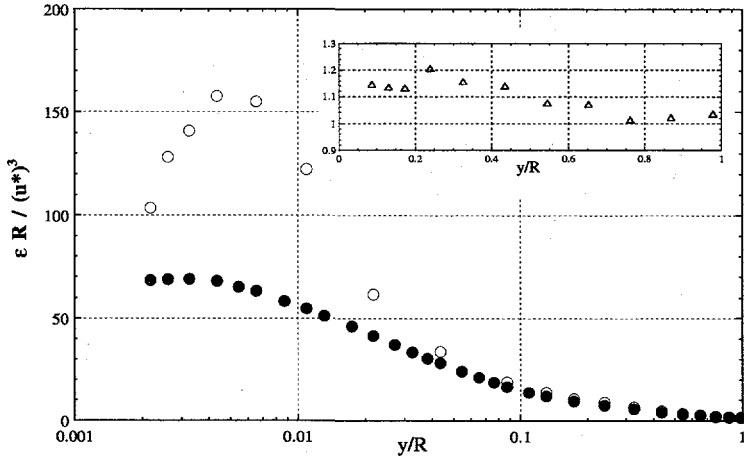


Figure 4.15: Dissipation rate in fully developed pipe flow; $Re = 75.000$: $R\varepsilon/(u^*)^3$; $15\nu(\partial u_x/\partial x)^2$ (●); Inertial subrange (○). Inserted: $\varepsilon_{-5/3}/\varepsilon_{iso}$ (Δ).

as direct numerical simulations and large eddy simulations. Chasnov [17] concluded that on average the numerically obtained values of the Kolmogorov constant was approximately 30% higher than values obtained in high turbulent Reynolds number atmospheric boundary layers. The large scatter in the reported values of C_K can be explained by the different methods for obtaining the dissipation rate, and also the different methods for deciding the location and level of the inertial plateau. Unfortunately Eq. 4.39 does not apply to near wall turbulence, since the turbulent Reynolds number drops inside $y^+ \simeq 15$. This was pointed out by Gibson (see Azad [7]). In this region Eq. 3.15 is also a crude approximation, due to the large degree of anisotropy and increasing turbulence intensity. Near wall data for the dissipation rate has been reported from several direct numerical simulations, although these are restricted to low Reynolds numbers.

Figure 4.15 compares the dissipation rate obtained from Eq. 4.39 and Eq. 3.15, scaled with the pipe radius and the friction velocity. The Kolmogorov constant is taken as $C_K = 0.53$, and the "inertial plateau" is taken as the maximum of the compensated streamwise spectrum: $k_x^{5/3} E_{xx}(k_x)$. This corresponds to the wave number range which Saddoughi and Veeravalli [54] described as an intermediate range between the inertial scales and the dissipation scale.

pative scales. For $y/R > 0.1$ the two methods for obtaining the dissipation rate compared within 20%, and the best correspondence is found near the centre line.

4.4 Remarks on the Inertial Range Scaling

The inertial subrange was derived assuming absence of production and dissipation in this range, which means that

$$\Upsilon_p(k_x) \simeq 1 ; \quad \Upsilon_\epsilon(k_x) \simeq 0 \quad (4.40)$$

The interesting aspect is the sensitivity of a -5/3 range to deviations from this criterium. Figure 4.14 shows the integral function of the dissipation spectrum for $0.02 < y/R < 1$, corresponding to $R_\lambda \epsilon [112, 200]$. The results are obtained from the previously reported dissipation spectra for $Re = 75.000$. The wave number is scaled with the Kolmogorov micro scale. At $\eta k_x = 0.03$, approximately 4% of the total dissipation rate has occurred. Figure 4.12 shows the corresponding integral function of the production spectrum for $0.021 \leq y/R \leq 0.44$. The result indicate that production occurs up to $\eta k_x = 0.2$, which corresponds to the maximum of the dissipation spectrum. The important observation, is that there is no range which satisfies Eq. 4.40. This means that there is an overlap between wave numbers of production and dissipation scales, which suggests that the energy containing and dissipative scales are not sufficiently separated. What appears as an inertial range is rather what Saddoughi and Veravalli described as the intermediate crest. This will be examined in further detail in the following chapter.

4.5 Conclusion

Streamwise, lateral and cross-correlation spectra are reported for different y/R positions in fully developed pipe flow at $Re = 75.000$. The purpose of the investigation was to examine the extent of a -5/3 inertial subrange at moderate values of R_λ . Away from the pipe wall only a narrow range of wave numbers applied to the -5/3 range.

The lateral spectra were found to collapse with the calculated isotropic spectrum only for $\eta k_x > 0.2$. This suggests that only the scales smaller than the maximum in the dissipation spectra are isotropic. At $\eta k_x = 0.2$, 60% of

the total dissipation has occurred. Contribution to the dissipation rate spans the wave number range $0.03 < \eta k_x < 1$. This result also indicates that a possible inertial range can not be isotropic, which is why the lateral spectra do not show an extensive $-5/3$ range.

The cross correlation spectra did not show a clear $-7/3$ inertial range, as suggested by Tennekes and Lumley.

The integral function of the dissipation rate spectrum showed little variation with the y/R position. Variation in the integral function for the production spectrum was found to be much more pronounced, and when approaching the pipe wall the turbulence production persisted far into the dissipative scales.

Even if streamwise power spectra showed a narrow $-5/3$ range in the pipe core region, this region was not consistent with absence of turbulence production and dissipation.

The essential result is therefore that what appears as an inertial range, violates several of the basic restrictions posed by Kolmogorov. The conclusion is in favour of the results reported by Bowman [9], suggesting that the turbulent Reynolds number must be significantly higher than the values reported by Lawn ($R_\lambda = 140$) [36]. The large energy containing and dissipative scales must be separated by several decades for the existence of a "true" inertial range.

The results indicate how the intermediate range between the "true" inertial range and the dissipative range can be misinterpreted for low and moderate R_λ .

Further evidence for these conclusions will be presented in the following chapter, based on the non-universal inertial scaling of the second- and third order longitudinal structure functions.

Chapter 5

Structure functions

The intention of the present investigation was to examine the universality of the relation between the inertial scaling of the streamwise power spectra and the second order longitudinal structure function, which relate analytically through a Fourier transform. Results presented in the previous chapter indicated that the appearance of a $-5/3$ inertial range in the streamwise power spectrum was not convincing for turbulent Reynolds numbers as low as $R_\lambda = 112$. Only by "best intention", could a $-5/3$ range be fitted to the spectra. It was also shown that several of the basic restrictions posed by Kolmogorov, such as separation of energy containing and dissipative scales and absence of production and dissipation in this range, were violated. A preliminary check on the inertial range behaviour of the structure functions, indicated a discrepancy between the inertial scaling constants for the streamwise power spectrum and the second order longitudinal structure function. Antonia et al. [4] stated that there is no strong evidence for R_λ being responsible for the discrepancies in the scaling constants for the structure functions. However, most results reported on structure functions, are obtained from experiments in free turbulent jets (see Noullez et al. [46]; Pearson and Antonia [48]; Anselmet et al. [2]), or in atmospheric boundary layers. Free turbulent jets have the capability of producing high R_λ , and also offer convenient experimental resolution. Unfortunately, the high values of R_λ , is obtained at the expense of high turbulence intensity. At laboratory scales, it is difficult to obtain high values of R_λ , and still retain low turbulence intensity. For high intensity flows, the validity of the Taylor "frozen flow" approximation, the accuracy of the measured dissipation rate and the accuracy of the power spectra must be considered. Antonia et al. [5] reported structure function

results in a turbulent wake behind a circular cylinder. The experiment was selected on basis of its low turbulence intensity. For the present work, the low turbulence intensity core region of fully developed pipe flow was considered convenient for a similar study.

In the following sections, structure function results are reported for the pipe centre line and the half radius. The local streamwise turbulence intensity at these two locations were $Tu_x < 3.6\%$ and $Tu_x < 6\%$ respectively. This justifies the application of the "frozen flow" approximation, which is the "corner stone" for determining structure functions from single point measurements. The results provide important information regarding the universal scaling of the inertial range at low and moderate R_λ .

5.1 Structure Function Inertial Range Scaling

Introducing the velocity increments, pictured in Fig. 5.1, the second order longitudinal structure function (B_{ll}) can be defined as,

$$B_{ll}(r_x) = (\delta u_x)^2 = \overline{[u_x(\mathbf{X} + r_x \mathbf{e}_x) - u_x(\mathbf{X})]^2}, \quad (5.1)$$

where r_x is the streamwise component of the separation vector \mathbf{r} . Expanding the right hand side, and assuming homogeneity in the streamwise direction, Eq. 5.1 can be rewritten as:

$$B_{ll}(r_x) = 2\overline{u_x^2} - 2Q_{xx}(r_x) \quad (5.2)$$

where $Q_{xx}(r_x) = \overline{[u_x(\mathbf{X})u_x(\mathbf{X} + r_x \mathbf{e}_x)]}$ is the two-point streamwise correlation function. Equation 5.1 relates to the inertial range of the streamwise power spectrum $\{E_{xx}(k_x)\}$ by a fourier transform, such that

$$E_{xx}(k_x) = \mathcal{F}\{B_{ll}(r_x)\} \quad (5.3)$$

Kolmogorov's expression for the inertial range of the one-dimensional power spectrum was previously expressed as:

$$E_{xx}(k_x) = C_K \varepsilon^{2/3} k_x^{-5/3} \quad (5.4)$$

It can be shown (see e.g. Lindborg [38]) that the corresponding second order structure function must have the inertial range form:

$$B_{ll}(r_x) = C_2 \varepsilon^{2/3} r_x^{2/3}, \quad (5.5)$$

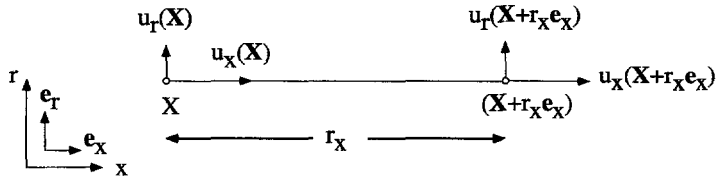


Figure 5.1: Velocity increments for structure functions.

where the $2/3$ scaling exponent corresponds to a $-5/3$ exponent in the power spectrum, and C_2 relates analytically to C_K . This may be deduced by introducing Eq. 5.5 in Eq. 5.2. Using the following fourier transform pairs¹:

$$\mathcal{F}\left\{\overline{u_x^2}1\right\} = \overline{u_x^2}\delta(k_x) \quad (5.6)$$

$$\mathcal{F}\{Q_{xx}(r_x)\} = \frac{1}{\pi} \int_{-\infty}^{\infty} Q_{xx}(r_x) \exp(-ik_x r_x) dr_x = E_{xx}(k_x) \quad (5.7)$$

$$\mathcal{F}\left\{\frac{B_{ll}(r_x)}{2}\right\} = \frac{1}{2\pi} \int_{-\infty}^{\infty} B_{ll}(r_x) \exp(-ik_x r_x) dr_x \quad (5.8)$$

$$= \frac{C_2 \varepsilon^{2/3}}{2\pi} \int_{-\infty}^{\infty} (r_x)^{2/3} \exp(-ik_x r_x) dr_x \quad (5.9)$$

$$= \frac{\Gamma(5/3)}{\pi} \cos(\frac{5\pi}{6}) C_2 \varepsilon^{2/3} k_x^{-5/3} \quad (5.10)$$

where $\delta(k_x)$ is the Dirac delta function, which is zero, except at $k_x = 0$. Since $k_x = 0$ represents an infinite length scale, this term vanishes. Thus Eq. 5.2 may be written in wave number space as,

$$\frac{-\Gamma(5/3)}{\pi} \cos(\frac{5\pi}{6}) C_2 (\varepsilon^{2/3} k_x^{-5/3}) = C_K (\varepsilon^{2/3} k_x^{-5/3}), \quad (5.11)$$

where the gamma function is defined as:

$$\Gamma_{(\alpha)} = \int_0^{\infty} \exp(-t) t^{\alpha-1} dt \quad (5.12)$$

¹Private communication with E.Lindborg, Royal Institute of Technology, Department of Mechanics, Sweeden

The correlation between the Kolmogorov constant and the second order structure function constant then reduces to,

$$C_K = -\frac{\Gamma_{(5/3)}}{\pi} \cos\left(\frac{5\pi}{6}\right) C_2 \quad (5.13)$$

Introducing the numerical values of $\Gamma_{(5/3)} = 0.9017$ and $\cos\left(\frac{5\pi}{6}\right) = -0.867$, the analytical relation between the scaling constants gives:

$$C_2 = 4.02 C_K. \quad (5.14)$$

Different values of the Kolmogorov constant was discussed in the previous chapter. A review by Sreenivasan [58], suggested $C_K = 0.53 \pm 0.055$, which gives $C_2 = 2.13 \pm 0.22$. Due to the direct relation between C_2 and C_K , one would expect C_2 to display a similar universality, for the same R_λ -range. A number of experiments has confirmed the 2/3 scaling exponent, both for moderate and high R_λ . However, the values of the scaling constant C_2 are more scattered, and in general underestimated compared to Eq. 5.14. The author believes that different methods for obtaining the dissipation rate, may be partly responsible for the variation in C_2 . However, if the dissipation rate is extracted from the inertial range of the power spectrum (Eq. 4.39), the two scaling constants C_K and C_2 are expected to relate by Eq. 5.14. In other words, if $E_{xx}(k_x)$ has a "true" inertial range which scales with ε and C_K , the second order structure function should scale with the same ε and the corresponding value of C_2 . Thus the two scaling constants should relate directly by the inertial plateau of the compensated power spectrum and structure function as,

$$C_2 = C_K \left\{ \frac{B_u(r_x) r_x^{2/3}}{E_{xx}(k_x) k_x^{5/3}} \right\}, \quad (5.15)$$

independent of the accuracy of the dissipation rate. To be able to compare structure functions with power spectra, it is convenient to transform the spatial separation to wave number. The Taylor time-space conversion gives $k_x = 2\pi/(U_x \delta t)$ and $r_x = U_x \delta t$, such that the wave number k_x that corresponds to the spatial separation r_x is:

$$k_x = \frac{2\pi}{r_x} \quad (5.16)$$

The appearance of a power spectral inertial range should in this way coincide with the same range of scales in the structure functions.

Assuming isotropy in the inertial range, it can easily be shown that the transverse structure function,

$$B_{tt}(r_x) = \overline{[u_r(\mathbf{X} + r_x \mathbf{e}_x) - u_r(\mathbf{X})]^2}, \quad (5.17)$$

must relate to B_{ll} as:

$$B_{tt}(r_x) = \frac{4}{3} B_{ll}(r_x), \quad (5.18)$$

corresponding to the spectral relation:

$$E_{rr}(k_x) = \frac{4}{3} E_{xx}(k_x) \quad (5.19)$$

These two relations may be used as a measure of inertial range isotropy.

One of the few analytical expressions in turbulence theory, is Kolmogorov's third order longitudinal structure function law,

$$B_{lll}(r_x) = (\delta u_x)^3 = -C_3(r_x \varepsilon) ; \quad C_3 \equiv \frac{4}{5}, \quad (5.20)$$

for r_x in the inertial range. Kolmogorov assumed isotropy in the dissipative range. Anselmet et al. [2], reported different values of C_3 from experiments in a duct ($R_\lambda = 515$) and a free jet ($R_\lambda \leq 852$), indicating that the higher R_λ jet flow was closer to the isotropic value of $C_3 = 4/5$, than the duct flow.

Lindborg derived an analytical expression for the "longitudinal-transverse-transverse" structure function:

$$B_{ltt} = \overline{[u_x(\mathbf{X} + r_x) - u_x(\mathbf{X})][u_r(\mathbf{X} + r_x) - u_r(\mathbf{X})]^2}, \quad (5.21)$$

and found for the inertial range behaviour :

$$B_{ltt} = -\frac{4}{15} (r_x \varepsilon) \quad (5.22)$$

Combined with the expression of Kolmogorov (Eq. 5.20), this resulted in the convenient relation,

$$\frac{B_{lll}(r_x)}{B_{ltt}(r_x)} = 3. \quad (5.23)$$

Lindborg proposed this to be a better measure of isotropy than Eq. 5.20, since it does not rely on the accuracy of the determination of the dissipation rate.

5.2 Measured Structure Functions

A separate experiment was designed to obtain structure functions for a larger range of turbulent Reynolds numbers from $R_\lambda = 126$ to $R_\lambda = 320$ in the fully developed pipe flow. According to previous experiments the lower R_λ represents the lower limit for existence of an inertial range, and the highest R_λ should be sufficient for a clear inertial range to appear. The experiment was performed in pipe rig II, using a larger fan to increase the bulk velocity. For each bulk velocity, structure functions were measured on the symmetry axis, and on the half radius.

5.2.1 Experimental details

Time series used for structure function calculations were obtained with a $2.5 \mu\text{m}$ single hot-wire, with a length to diameter ratio of $l_w/d_w = 160$. The experimental procedure was the same as for the previous experiments, described in chapter 2. Accurate determination of structure functions, requires a large number of data, to properly capture the tails of the probability density functions. The purpose of the investigation was to examine 2nd and 3rd order longitudinal structure functions. The number of data sampled for each time series was $N = 10^7$, which is more than sufficient to capture the tales of the probability density function for the 3rd order moments. The reason for acquiring such large number of data was to obtain smooth power spectra and structure functions. The filter frequency (n_c) and the sampling frequency (n_s) were adjusted according to the Kolmogorov frequency (n_K), such that $n_c \simeq n_K$ and $n_s = 2 \times n_c$. Since the number of data in each time series was kept constant, the integration time (t_s) was adjusted according to n_s . Some characteristic properties are presented in Tab. 5.1, where R and $R/2$ refers to the centre line and the half radius respectively. The Fourier spectra were obtained using a Hanning window function, and the number of spectral points were 2^{12} . This means that the spectra are calculated from an average of 2441 windows.

Table 5.1: Characteristic parameters for structure function experiments

Exp. Location	(a) R	(b) R	(c) R	(d) R/2	(e) R/2
$R_\lambda = \left\{ \lambda \overline{(u_x^2)}^{1/2} / \nu \right\}$	126	153	204	245	320
$\varepsilon = \left\{ 15\nu \overline{(\partial u_x / \partial x)^2} \right\} [m^2/s^3]$	1.89	4.61	19.6	10.23	38.5
$\varepsilon = \left\{ k_x^{5/3} E_{xx}(k_x) / C_K \right\}^{3/2} [m^2/s^3]$	1.92	4.67	18.9	10.12	40.6
$Tu_x \% = \overline{(u_x^2)}^{1/2} / U_x \times 100\%$	3.5	3.4	3.5	5.5	4.9
l_w/η	2	2.5	3.3	2.86	4.16

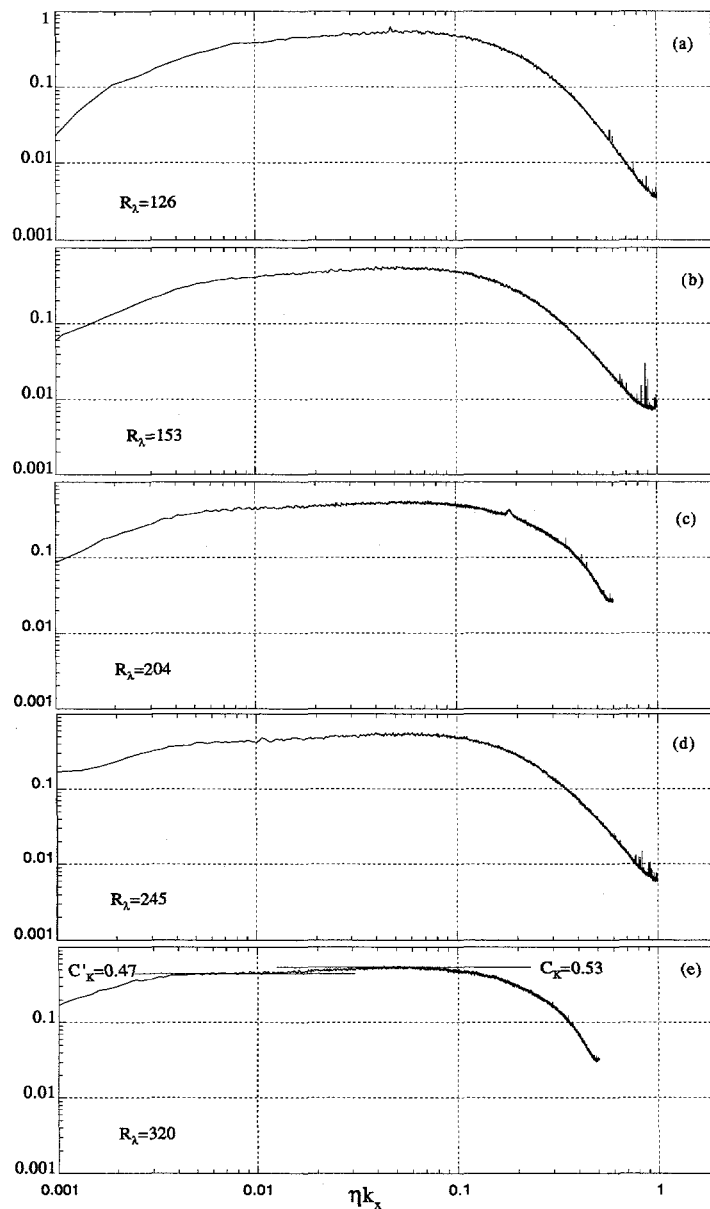
5.2.2 Dissipation rate

The dissipation rate (ε) was obtained from the inertial range of the streamwise power spectrum, such that

$$\varepsilon = \left\{ \frac{k_x^{5/3} E_{xx}(k_x)}{C_K} \right\}^{3/2}, \quad (5.24)$$

assuming $C_K = 0.53$, and also from the isotropic relation $15\nu \overline{(\partial u_x / \partial x)^2}$. On the pipe centre line the Reynolds stress tensor is near isotropic, which supports the assumption of isotropy in the dissipation range. This means that Eq. 3.15 should be a good measure of the dissipation rate. In other words, there should be good correspondence between Eq. 3.15 and Eq. 5.24 for the inertial range. Differences in the two methods were within 6%, as indicated in Tab 5.1. The largest deviation occurred in experiment (e), where the ratio of the hot-wire length (l_w) and the Kolmogorov length (η) was too large to capture the entire dissipation range. The difference was found consistent with the lack of small scale resolution, and therefore do not reflect

a non-universal behaviour of C_K . The probe resolution was still sufficient to capture the inertial scales. The structure function scaling was based on the dissipation rate obtained from Eq.5.24. The compensated streamwise power spectra $\{k_x^{5/3} E_{xx}(k_x) \varepsilon^{-2/3}\}$ are shown in Fig. 5.2. The smoothness of the spectra is due to the large time-series. Independent of R_λ , the spectra show a "crest" slightly below the wave number of maximum dissipation ($\eta k_x \simeq 0.1$). A similar observation was reported by Saddoughi and Veeravalli [54], for $R_\lambda \in [500, 1450]$, in a large scale wind tunnel boundary layer. They found no indication which supported that the "crest" was reduced with increasing R_λ . The range of wave numbers covering the "crest" does not seem to increase with increasing R_λ . For low turbulent Reynolds numbers this "crest" can be misinterpreted as a narrow inertial range, as described in the previous chapter. However the true inertial range appears below $\eta k_x \simeq 0.02$. The width of this plateau clearly increases with increasing R_λ , and is also separated sufficiently from the dissipative scales to fulfil the fundamental requirements for an inertial range. The results indicate that the "crest" does not represent an inertial range, but rather an intermediate range between the inertial scales and the dissipative scales. Due to the moderate values of R_λ , the inertial range occupied less than one decade. Figure 5.3 shows the integral function of the dissipation rate spectrum, defined in the previous chapter. The two curves represent $R_\lambda = 126$ and $R_\lambda = 320$. Theoretically, the inertial range must be located at wave numbers below $\eta k_x = 0.01$, to avoid interference of dissipation. No visible difference can be seen between the functions for the two values of R_λ , suggesting a universal behaviour of the dissipative range. Saddoughi and Veeravalli [54] defined the dissipation range for $\eta k_x > 0.1$. However, the present results indicate that more than 20% of the dissipation rate has occurred in the range $\eta k_x \in [0.01, 0.1]$. This range also collapses with the "crest" in the compensated spectrum, which strongly supports that this can not represent the "true" inertial range. If the Kolmogorov constant is inferred from the second plateau, a value of $C'_K = 0.47$ is obtained. This is slightly below the reported scatter of $C_K = 0.53 \pm 0.055$. Figure 5.4 shows a schematic picture of the compensated streamwise power spectra, for different values of R_λ , indicating the two different plateaus which are observed. As the turbulent Reynolds number increases, only the lower plateau extends into lower wave numbers, while the extent of the "crest" remains unchanged. Thus the lower plateau is consistent with increasing separation of scales as R_λ increases, giving a more pronounced inertial range.

Figure 5.2: Compensated streamwise power spectra, $k_x^{5/3} E_{xx}(k_x) \varepsilon^{-2/3}$.

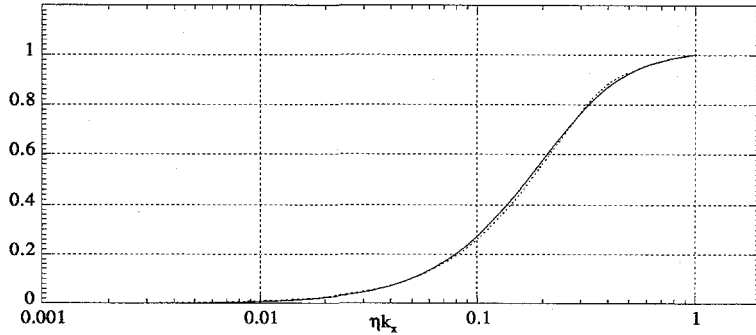


Figure 5.3: Integral function of dissipation rate spectrum: $\left\{ 15\nu\varepsilon^{-1} \int_0^{k_x} k_x^2 E_{xx}(k_x) dk_x \right\}$ for $R_\lambda = 126$ (solid) and $R_\lambda = 320$ (dotted).

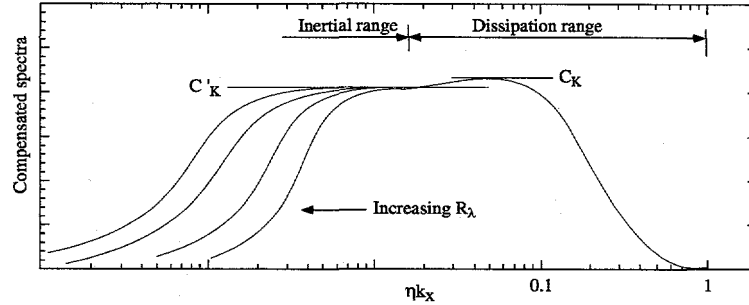


Figure 5.4: Schematic turbulent Reynolds number variation of compensated streamwise spectra, $\left\{ k_x^{5/3} E_{xx}(k_x) \varepsilon^{-2/3} \right\}$.

5.2.3 Second and third order longitudinal structure functions

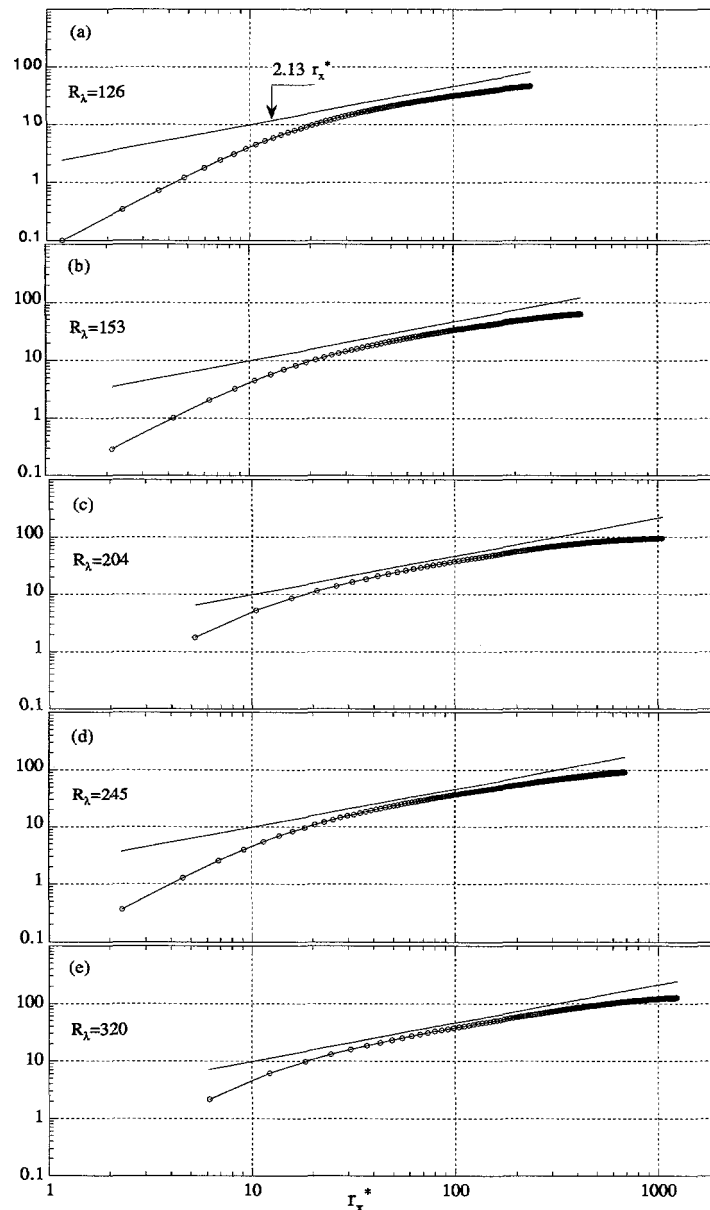
Dividing the second order longitudinal structure function,

$$B_{ll}(r_x) = (\delta u_x)^2 = \overline{[u_x(\mathbf{X} + r_x \mathbf{e}_x) - u_x(\mathbf{X})]^2} \quad (5.25)$$

by the square of the Kolmogorov velocity (ϑ), the non-dimensional form of the inertial range reads:

$$B_{ll}(r_x^*)/\vartheta^2 = C_2(r_x^*)^{2/3} ; \quad r_x^* = r_x/\eta \quad (5.26)$$

Figure 5.5 shows the measured second order structure function for different values of R_λ , compared to Eq. 5.26(solid line). The scaling constant was

Figure 5.5: Second order longitudinal structure function; $B_{ll}(r_x^*)/\delta^2$.

initially taken as $C_2 = 2.13$, which relates analytically to a Kolmogorov constant of $C_K = 0.53$. This corresponds to the maximum value of the "crest" in the compensated spectrum. In the previous section, it was argued that if the Kolmogorov constant was taken from the lower plateau, a value of $C'_K = 0.47$ was obtained, which corresponds to $C_2 = 1.86$. The author believes that this is a more correct representation of the inertial range, which will be argued further in the following text. The scaling exponents varies only slightly with the turbulent Reynolds number, and compares well with the theoretical value of $2/3$. For the lowest value of R_λ , only a narrow region applies to the $2/3$ range, located within $r_x^* \in (30, 70)$. This corresponds to a non-dimensional wave number of $\eta k_x \epsilon \langle 0.089, 0.21 \rangle$, which is in conflict with the maximum of the dissipation rate spectrum, since the inertial range must be separated from the dissipation range. A "true" inertial range is therefore not believed to exist in this case. The $2/3$ range extends into larger separations (r_x^*) as R_λ increases. For $R_\lambda = 320$ the inertial range covers $r_x^* \in (30, 400)$, corresponding to $\eta k_x \epsilon \langle 0.016, 0.21 \rangle$. At $\eta k_x = 0.016$, less than 4% of the total dissipation has occurred, which supports the existence of an inertial range. A similar trend can be seen in Fig. 5.6 for the third order longitudinal structure function,

$$B_{uu}(r_x^*)/\vartheta^3 = C_3 r_x^*, \quad (5.27)$$

which is compared to the theoretical form: $B_{uu}(r_x^*) = 4/5 r_x^*$. Deviation from the +1 scaling exponent is slightly more pronounced, compared to the second order function. The predicted scaling constant C_3 is significantly lower than the analytical value of $C_3 = 4/5$. It should be emphasized that the analytical value of C_3 requires that the inertial scales are isotropic. The scaling constant clearly increases with the turbulent Reynolds number, as pictured in Fig. 5.7. An important observation is that even for $R_\lambda = 320$, which is believed to be a sufficient R_λ for appearance of a universal inertial range, the experimentally deduced scaling constants are significantly lower than the theoretical values. For $R_\lambda = 126$, C_2 was underestimated by as much as 28%, and for $R_\lambda = 320$, the value of C_2 was still 17% too low. The corresponding scaling constant (C_3) for the third order longitudinal structure function was underestimated by 57% for $R_\lambda = 126$ and 35% for $R_\lambda = 320$, compared to the analytical value of $C_3 = 4/5$. The tendency towards $C_2 = 2.13$ and $C_3 = 0.8$ is not convincing. If the Kolmogorov constant is obtained from the second plateau, a value of $C'_K = 0.47$ was found. This corresponds to $C'_2 = 1.89$, which agrees better with the experimental scaling constants for the second order

structure functions. For $R_\lambda = 320$, the difference is then reduced from 17% to 7%. The difference in C_3 remains unchanged, since the measured dissipation rate is not altered. From the present results, it is not possible to conclude that the experimental values collapse with the theoretical ones for "infinite" Reynolds number. The inertial range is then expected to occur in the same wave number range (i.e. spatial separation) in the power spectrum as in the n'th order structure functions. Further experimental work should therefore be performed, to establish the R_λ dependency of the inertial scaling for higher values of R_λ .

5.3 Conclusions

Second and third order longitudinal structure functions are reported for fully developed pipe flow. The experimental data were obtained at the centre line and at the half radius of the pipe. The experiment was chosen due to its low turbulence intensity ($Tu_x < 6\%$), which justifies the application of the Taylor time-space conversion. The experiment also displayed close correspondence between the dissipation rate obtained from $\varepsilon = 15\nu \overline{(\partial u_x)^2} / (\partial x)$ and from the inertial range of the streamwise power spectrum (within 6%). The Kolmogorov constant was taken as $C_K = 0.53$, and the inertial plateau was taken from the maximum of the compensated streamwise spectrum. The range of turbulent Reynolds number was $R_\lambda = 126$ to $R_\lambda = 320$, for which an inertial range was expected to appear. The intention of the investigation was to examine universality of the relation between the inertial scaling of the streamwise power spectra and the second order longitudinal structure function, which relate analytically through a Fourier transform. The direct relation between C_K and C_2 , made it possible to determine C_2 , without interference of the dissipation rate. Since the present results do not depend on the accuracy of the dissipation rate, the only explanation for the differences between the theoretical and measured values must be related to the turbulent Reynolds number. In other words the energy containing and dissipative scales must be widely separated for the appearance of universal inertial range, which is consistent with both the power spectrum and the second order longitudinal structure function.

The compensated streamwise spectrum displayed two different plateaus, which both applied to the -5/3 scaling exponent. The first plateau appeared as a "crest" near the maximum of the dissipation spectrum, and can there-

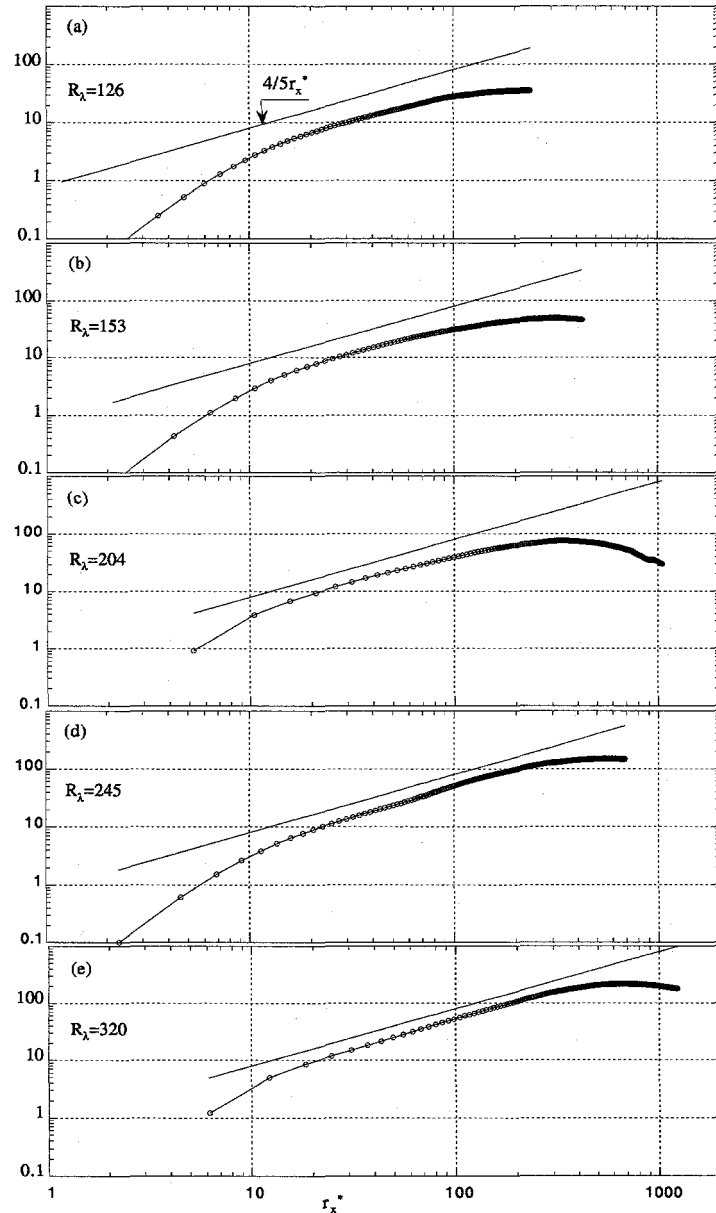


Figure 5.6: Third order longitudinal structure function; $B_{333}(r_x^*)/\theta^3$.

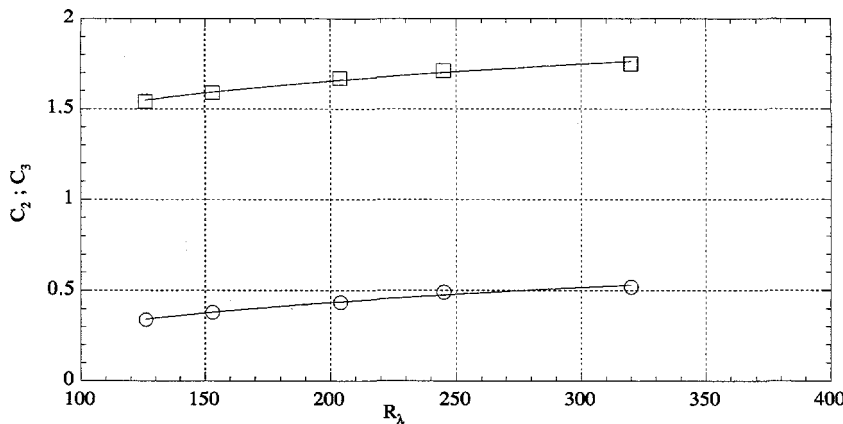


Figure 5.7: Inertial range scaling constants for second and third order longitudinal structure functions at different R_λ . C_2 (□) : C_3 (○)

fore not represent a "true" inertial range. The author believes that for low and moderate turbulent Reynolds numbers this range is frequently misinterpreted as an inertial range. However, when inferring the dissipation rate from the "crest", this seems to compare well with the isotropic formulation. The second plateau appeared below $\eta k_x \simeq 0.02$. The Kolmogorov constant was then reduced from $C_K = 0.53$ to $C_K = 0.47$, to give the same value of the dissipation rate. The corresponding second order structure function constant then reduces from $C_2 = 2.13$ to $C'_2 = 1.89$, which enhances the correspondence between the experimental and theoretical value of C_2 . An increasing correspondence between the theoretically and experimentally deduced scaling constants was observed with increasing turbulent Reynolds number. A question which is still not answered is limit of the scaling constants for infinite R_λ .

Further experimental work should be performed at higher values of R_λ , preferably in flow situation with low turbulence intensity, to avoid experimental error. The result should provide important information for the increasing amount of numerical experiments, concerning the spectral behaviour of turbulence. Both direct numerical simulations and subgrid scale models are still restricted to low and moderate R_λ , and it is important that model parameters are not tuned against false premises.

Chapter 6

Invariant Analysis

This chapter presents the classical method of describing the Reynolds stress anisotropy tensor in terms of invariants. A new derivation of invariants for the spectral anisotropy tensor is reported. Experimental results are presented for fully developed pipe flow.

6.1 Time Mean Invariants

Invariant representation of Reynolds stresses has proven to be a useful tool in studying departures from isotropy, axisymmetry and two-component turbulence. This theory has been extensively applied to deduction of realizable turbulence models [42]. The formulation of invariants in the following text, is taken from Lumley [42], and is included as a basis for the spectral invariant analysis presented in section 6.2.

The Reynolds stress tensor ($\tau_{ij} = \rho\bar{u}_i\bar{u}_j$) may be expressed in terms of an anisotropic (τ'_{ij}) and an isotropic (τ^o_{ij}) tensor, such that

$$\tau_{ij} = \tau'_{ij} + \tau^o_{ij}, \quad (6.1)$$

where i and j may equal 1, 2 or 3. In Cartesian and cylindrical coordinates, the indices refers to (x, y, z) and (x, r, θ) respectively. Introducing the Kronecker delta (δ_{ij}) and the standard notation of summation over repeated indices, the isotropic part may be written:

$$\tau^o_{ij} = \frac{1}{3}\tau_{kk}\delta_{ij} \quad (6.2)$$

The Reynolds stress anisotropy tensor then reads,

$$\tau'_{ij} = \tau_{ij} - \frac{\tau_{kk}}{3}\delta_{ij} = \begin{pmatrix} (\tau_{xx} - \frac{1}{3}\tau_{kk}) & \tau_{xr} & \tau_{x\theta} \\ \tau_{rx} & (\tau_{rr} - \frac{1}{3}\tau_{kk}) & \tau_{r\theta} \\ \tau_{\theta x} & \tau_{\theta r} & (\tau_{\theta\theta} - \frac{1}{3}\tau_{kk}) \end{pmatrix} \quad (6.3)$$

A non-dimensional anisotropy tensor can be defined as:

$$b_{ij} = \frac{\tau'_{ij}}{\tau_{kk}} = \frac{\tau_{ij}}{\tau_{kk}} - \frac{1}{3}\delta_{ij} \quad (6.4)$$

By definition $b_{kk} = 0$ for incompressible flows. In case of isotropic turbulence, all elements of the anisotropy tensor (b_{ij}) vanish, though it is clear that $b_{ij} = 0$ for all i and j is not a sufficient criteria for isotropy. The diagonal elements of b_{ij} are restricted to $-1/3 < b_{ij} < 2/3$. The three principal invariants of b_{ij} , are the coefficients of the characteristic equation for the tensor. These may be deduced by taking the determinant of the tensor when the principal anisotropy stress σ is subtracted, such that

$$\det(b_{ij} - \sigma\delta_{ij}) = 0. \quad (6.5)$$

This results in the characteristic equation,

$$\sigma^3 - I_1\sigma^2 + I_2\sigma + I_3 = 0 \quad (6.6)$$

which is a third order polynomial for the unknown principal anisotropy stress σ . From Eq. 6.6 it follows that the three coefficients are coordinate invariants, which means that they are scalar parameters. The Reynolds stress anisotropy tensor has zero trace, and the invariants become

$$\begin{aligned} I_1 &= b_{kk} \equiv 0 \\ I_2 &= -\frac{1}{2}b_{ij}b_{ji} \\ I_3 &= \det(b_{ij}) = e_{ijk}b_{i1}b_{j2}b_{k3}, \end{aligned} \quad (6.7)$$

where $\det(b_{ij})$ is the determinant of the tensor, and e_{ijk} is the permutation tensor. These expressions follow from the derivation of Eq. 6.6, and are identical to the definition presented by Lumley [42]. Another definition for the invariants is also frequently used, but these invariants relate directly to Eq. 6.7.

In case of two-dimensional mean flow, the anisotropy tensor, using cylindrical notation, reduces to

$$b_{ij} = \begin{pmatrix} b_{xx} & b_{xr} & 0 \\ b_{rx} & b_{rr} & 0 \\ 0 & 0 & b_{\theta\theta} \end{pmatrix}, \quad (6.8)$$

with the corresponding invariants

$$\begin{aligned} I_2 &= -\frac{1}{2}(b_{xx}^2 + b_{rr}^2 + b_{\theta\theta}^2 + 2b_{xr}^2) \\ I_3 &= (b_{xx}b_{rr} - b_{xr}^2)b_{\theta\theta} \end{aligned} \quad (6.9)$$

Thus I_2 must always be negative, while I_3 may take values of both sign.

In case of axisymmetric turbulence the two lateral normal stresses τ_{rr} and $\tau_{\theta\theta}$ must be equal, and the shear stress τ_{xr} must vanish. To satisfy the condition $I_1 = b_{kk} \equiv 0$, it follows that $b_{rr} = b_{\theta\theta} = -\frac{1}{2}b_{xx}$. The vanishing shear stress implies $b_{xr} = 0$. The two remaining invariants then reduce to

$$I_2 = -\frac{3}{4}b_{xx}^2 \quad ; \quad I_3 = \frac{1}{4}b_{xx}^3, \quad (6.10)$$

which gives the axisymmetric relations:

$$I_3 = \pm 2\left(\frac{-I_2}{3}\right)^{3/2} \quad \text{or} \quad I_2 = -3\left|\frac{I_3}{2}\right|^{2/3} \quad (6.11)$$

Lee and Reynolds [37] introduced the parameter A , defined as

$$A = \frac{I_3}{2(-I_2/3)^{3/2}}, \quad (6.12)$$

which follows directly from Eq. 6.11. For a realizable stress tensor, $A \in [-1, 1]$, and $A = \pm 1$ for axisymmetric turbulence. The parameter therefore indicates two different modes of axisymmetry, described by Lee and Reynolds [37] as "rod-like" ($A = -1$) and "disk-like" ($A = +1$) turbulence. The first one is represented by negative values of I_3 , which means that the two lateral normal stresses are larger than the streamwise component. The latter one represents a larger streamwise component. It was also suggested that A may be used as a measure of axisymmetry. If the Reynolds stress tensor develops towards an isotropic state, the parameter A may start to oscillate between between ± 1 , due to singularity.

Assuming two-component turbulence, one of the normal stresses vanishes. Since turbulence is three-dimensional in its nature, it is obvious that this represents a selection of special cases. The most common is the state of almost two-component turbulence near a wall, where the wall-normal fluctuations are suppressed. In Chapter 8 it will be shown that a similar situation occurs in a flow with secondary strain, causing attenuation of the component aligned with the strain. For two-component turbulence $b_{xx} = 0$, and putting $\tau_{xx} = 0$ gives $b_{xx} = -1/3$. The invariants then reduce to:

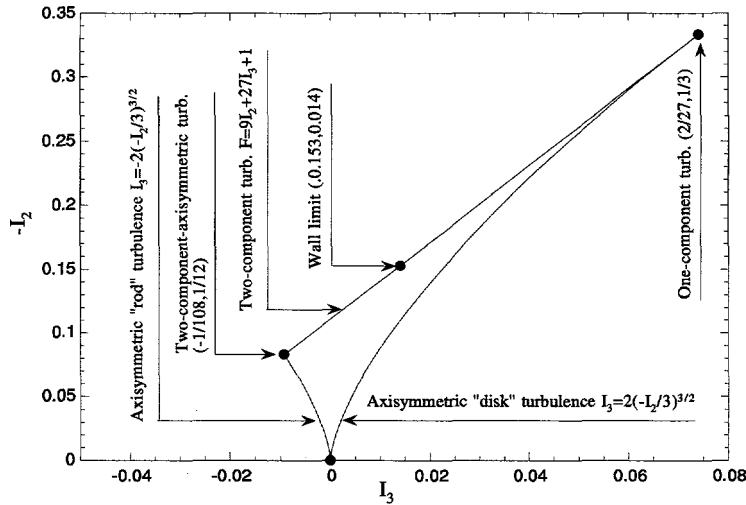
$$\begin{aligned} I_1 &= -\frac{1}{3} + b_{rr} + b_{\theta\theta} = 0 \\ I_2 &= -\frac{1}{2}\left(\frac{1}{9} + b_{rr}^2 + b_{\theta\theta}^2\right) \\ I_3 &= -\frac{1}{3}(b_{rr}b_{\theta\theta}) \end{aligned} \quad (6.13)$$

From these three equations, Lumley obtained the following relation between the two remaining invariants,

$$9I_2 + 27I_3 + 1 = 0. \quad (6.14)$$

Lumley suggested that the parameter $F = 9I_2 + 27I_3 + 1$ may be used as a measure of departure from isotropic and two-component turbulence. In this case $F \equiv 0$ for two-component turbulence, and $F \equiv 1$ for isotropic turbulence. In a plot of I_2 versus I_3 , presented in Fig. 6.1, the two lines of axisymmetry and the one for the two-component state, makes a closed triangle. This is usually called the Anisotropy Invariant Map (AIM)[42]. Limitations on the eigenvalues require that for a realizable Reynolds stress tensor, the combination of I_2 and I_3 must occur within the triangle. The three corners of the triangle represent isotropic, one-component and two-component-axisymmetric turbulence. Maximum anisotropy occurs at the state of one-component turbulence.

It is possible to estimate the limit of the invariants as the distance from the wall $y \rightarrow 0$. Introducing a Cartesian coordinate system (x, y, z) , with its origin at the wall, and y is the direction normal to the wall, it is possible to express the near wall fluctuations (u, v, w) in terms of the series

Figure 6.1: Anisotropy Invariant Map (AIM) of b_{ij} [42].

expansion[32]:

$$\begin{aligned} u &= a_1y + a_2y^2 + \dots \rightarrow u^2 = a_1^2y^2 + a_1a_2y^3 + a_2^2y^4 + \dots \\ v &= b_2y^2 + \dots \rightarrow v^2 = b_2^2y^4 + \dots \\ w &= c_1y + c_2y^2 + \dots \rightarrow w^2 = c_1^2y^2 + c_1c_2y^3 + c_2^2y^4 + \dots \\ uv &= a_1b_2y^3 + a_2b_2y^4 + \dots \end{aligned} \quad (6.15)$$

Including higher order terms, will not alter the present result. Introduced in Eq 6.4, the elements of b_{ij} , as $y \rightarrow 0$, then reduce to:

$$\begin{aligned} \lim_{y \rightarrow 0} b_{xx} &= \frac{a_1^2}{(a_1^2 + c_1^2)} - \frac{1}{3} \\ \lim_{y \rightarrow 0} b_{yy} &= -\frac{1}{3} \\ \lim_{y \rightarrow 0} b_{zz} &= \frac{c_1^2}{(a_1^2 + c_1^2)} - \frac{1}{3} \\ \lim_{y \rightarrow 0} b_{xy} &= 0 \end{aligned} \quad (6.16)$$

This simply suggests that the near wall behaviour of the streamwise and circumferential fluctuations, vary linearly with the wall distance. The wall

Table 6.1: Wall limit for the Invariants, based on DNS [32]

a_1	c_1	b_{xx}	b_{yy}	b_{zz}	b_{xy}	I_2	I_3	A
0.36	0.20	0.431	-0.333	0.0978	0	-0.153	0.014	0.608

limit is solely determined by the coefficients for the first order term of u and w . To obtain the wall limits for the invariants, numerical values for a_1 and c_1 are required. Karlsson and Johansson [30] reported $a_1 = 0.39$, based on LDV measurements in a channel flow. The data applied to the linear behaviour inside $y^+ \simeq 3$. Andersson and Kristoffersen [1] reported $a_1 = 0.41$ for DNS in channel flow. Table 6.1 gives an estimate based on DNS channel data by Kim et al. [32]. The wall limit of $(-I_2, I_3)$ is indicated in Fig. 6.1. It should be kept in mind however that this relies on the accuracy of a_1 and c_1 . Reservation must be taken with respect to e.g. Reynolds number variation. It is clear though that the wall limit occurs closer to the middle point of the two-component line than the edges.

6.1.1 Invariants in fully developed pipe flow

Fully developed pipe flow may be described by a core region and a near wall region. The core region is highly dominated by the axisymmetric confinement, and the wall region by the presence of the wall. At least on the centre line, the Reynolds stress tensor must relate to the state of axisymmetry. The interesting question is how far into the wall region this axisymmetric property persists, before it adapts to the state of near wall turbulence. The near wall region is expected to have a wide similarity with other wall bounded flows, such as flat plate boundary layer or channel flow. However Eggels et al. [21] found differences between pipe and channel flows, based on direct numerical simulations. The main discrepancy was found in the wall-normal component, and the deviation was attributed to the differences in wall impingement, caused by the curvature of the pipe wall. It is clear however that the pipe flow must adapt to the state of two-component turbulence, if the wall distance is sufficiently small. As described in the previous section, the anisotropy invariant map forms an absolute restriction to the Reynolds stress tensor. What makes it particularly useful to fully developed pipe flow, is the combination of axisymmetry and the state of two-component turbulence. The present results are obtained in the pipe rig facilities, described in Chapter 2.

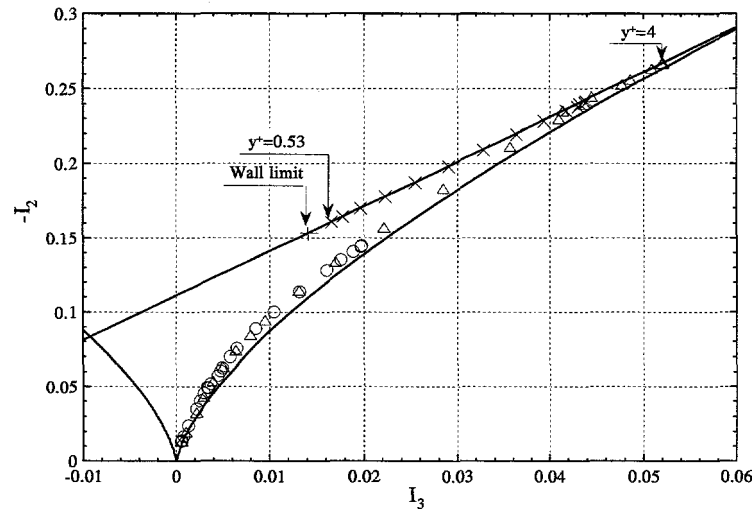


Figure 6.2: Anisotropy invariant map in low Reynolds number fully developed pipe flow.
 $Re=22.000$ (\circ) ; DNS Eggels (Δ), $Re=5.300$; DNS channel data of Kim (\times), $Re = 3.300$.

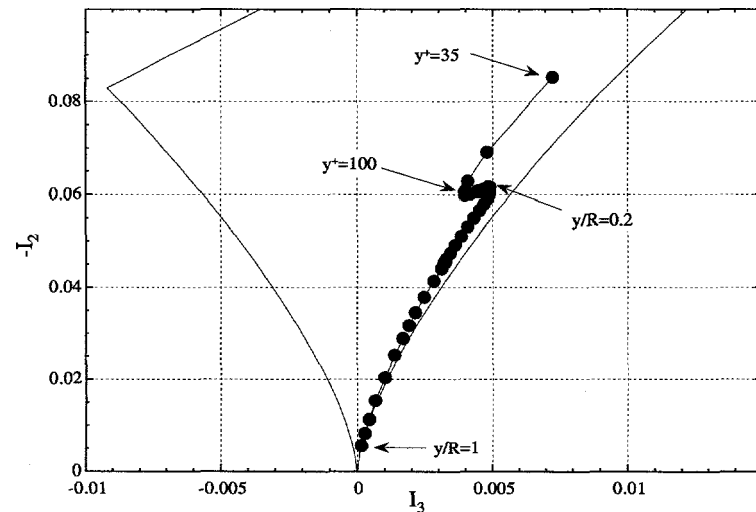


Figure 6.3: Anisotropy invariant map in fully developed pipe flow. $Re = 75.000$ (\bullet)

Figure 6.2 shows the anisotropy invariant map for $Re=22.000$, measured in pipe rig I. The results are compared to fully developed pipe flow DNS data by Eggels et al. [21] ($Re = 5300$). The near wall DNS channel data by Kim et al. [32] ($Re = 5600$) are shown for $0.53 < y^+ < 10$. On the pipe centre line both the present results and the DNS pipe data collapse on the right axisymmetric line, described by Lee and Reynolds as "disc-like" turbulence ($A = +1$). It is easy to argue that the data can not follow the left axisymmetric line, since the sign of A is directly controlled by the sign of I_3 . For the present situation, the streamwise component is everywhere larger than the two lateral components, such that b_{xx} is bound to be positive, and b_{rr} and $b_{\theta\theta}$ must be negative. From Eq. 6.9 it follows that I_3 is positive, thus the data can not relate to the left axisymmetric line. Theoretically, only the centre line location is allowed to apply exactly to the axisymmetric relation, since this situation require that the off-diagonal elements of b_{ij} are zero. The turbulent shear stress is known to vary linearly with the distance from the centre line, thus $b_{xr} \neq 0$. Despite this violation, the data closely follow the axisymmetric line, though it is clear that the Reynolds stress tensor is not truly axisymmetric. The data are squeezed between the axisymmetric and two-component restrictions, as the anisotropy increases towards the wall. The present results overlap the DNS pipe data of Eggels et al. [21]. The DNS data obtain a maximum of $(-I_2, I_3) = (0.267, 0.052)$ at $y^+ \approx 4$, and approaches the two component restriction inside this location. The near wall DNS channel data by Kim et al. [32] follows the two-component restriction inside $y^+ \approx 2$. Antonia et al. [3] presented invariant maps of the Reynolds stress, dissipation rate, and vorticity anisotropy tensor, based on the DNS data of Kim et al. [32]. The very near wall structure was found comparable with "rod-like" turbulence, and further away from the wall the structure shifted towards "disk-like" turbulence.

Figure 6.3 shows the anisotropy invariant map for fully developed pipe flow at $Re = 75.000$. The data were obtained in pipe rig II, which gave the best near-wall hot-wire resolution. In the core region the invariants closely follow the axisymmetric line ($A = +1$), similar to $Re = 22.000$. When moving towards the wall, the data gradually separates from this line, and then makes a distinct jump. The jump causes the invariants to separate from the axisymmetric line, before the data continues towards the two-component state. A similar effect can not be seen for $Re = 22.000$, or for the pipe DNS data, which is believed to be due to an insufficient Reynolds number. The jump starts at $y/R \approx 0.2$, corresponding to $y^+ = 300$, and end at

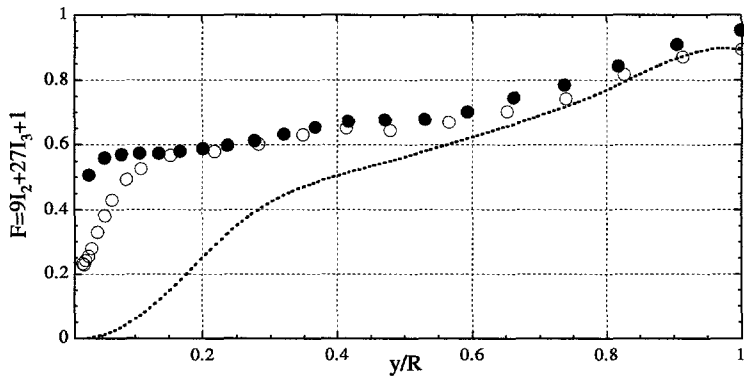


Figure 6.4: Anisotropy function in fully developed pipe flow - Outer scaling. $Re=22.000$ (\circ) ; $Re = 75.000$ (\bullet) ; DNS Eggels (dashed), $Re = 5300$

$y^+ \simeq 100$, corresponding to the outer part of the logarithmic wall region. The author believes that the sudden jump is related to the separation of a central core region from the near wall region. For the lower Reynolds numbers, the jump is much less pronounced. This suggests that the separation of the near wall region and the core region depends on the Reynolds number. The innermost point is located at $y^+ = 35$, which is barely inside the buffer region. However the tendency towards a two-component state is quite clear.

Figure 6.4 and Fig. 6.5 shows the anisotropy function, $F = 9I_2 + 27I_3 + 1$ for $Re = 22.000$, $Re = 75.000$ and for the DNS pipe data of Eggels et al. [21]. The two figures represent outer and inner scaling, respectively. Recall that $F = 1$ for isotropic turbulence, and $F = 0$ for two-component turbulence. The maximum value of F occurs at the pipe centre line, where $F = 0.95$ for $Re = 75.000$ and $F = 0.9$ for $Re = 22.000$. This indicates that the higher Reynolds number behaves closer to isotropy than the lower one, which may also be explained by a more pronounced separation of the core region and the near wall region. The centre line value for the DNS data collapse with the lower Reynolds number data. In outer scaling, the measured data follows the same trend towards the wall, although the values for the higher Reynolds number are somewhat larger. With inner scaling, the curves are seen to collapse inside $y^+ \simeq 100$, which corresponds to the inner part of the logarithmic wall region (see fig.). For $Re = 75.000$ a range of near constant F appears for $100 < y^+ < 300$. This corresponds to the same range of y^+

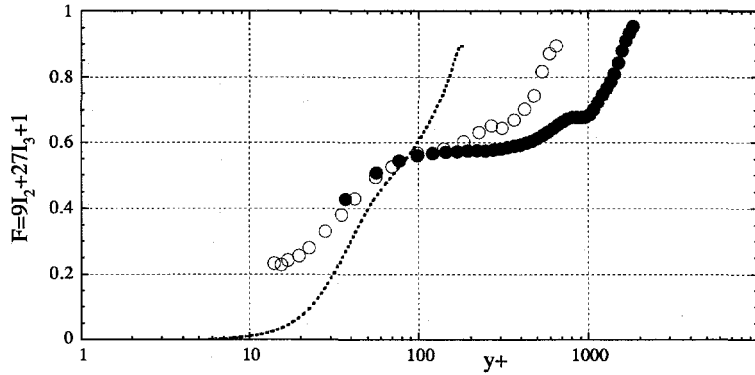


Figure 6.5: Anisotropy function in fully developed pipe flow - Inner scaling. $Re = 22.000$, (○); $Re = 75.000$ (●); DNS Eggels (dashed), $Re = 5300$

where the jump was observed in the anisotropy invariant map, indicating that the logarithmic region is a region of constant degree of anisotropy.

Although experimental data were not obtainable sufficiently close to the pipe wall, the tendency is clearly directed towards the two-component state. The DNS values drop steeper than the experimental values inside $y^+ \simeq 100$, possibly due to near wall measurement error, and shows a clear range of two-component turbulence inside $y^+ \simeq 4(F = 0.003)$.

In general the AIM reflects the behaviour of the large energy containing scales, since the Reynolds stress tensor is controlled mainly by the large scales. The picture of turbulence is commonly described by cascades of eddies, where the large scales are strained by the mean motion, and the smaller scales are strained by the turbulence. An interesting question is therefore the persistence of large scale characteristics into the smaller scales. In the following section a method for studying axisymmetric behaviour of the turbulence spectra is developed, and applied to turbulence spectra in fully developed pipe flow.

6.2 Spectral Invariant Analysis

A derivation of a new spectral anisotropy tensor is presented. The deduction has a general similarity with the invariant analysis for the Reynolds stress tensor, but also involves some fundamental differences.

The relation between the Reynolds stresses and the one-dimensional spectra $E_{ij}(k_x)$, where k_x is the streamwise wave number, was previously given as:

$$\tau_{ij} = \rho \int_0^\infty E_{ij}(k_x) dk_x \quad (6.17)$$

Based on the same idea as the anisotropy tensor τ'_{ij} , the spectral anisotropy tensor, $E'_{ij}(k_x)$, may be defined as,

$$E'_{ij}(k_x) = E_{ij}(k_x) - E^o_{ij}(k_x), \quad (6.18)$$

where $E^o_{ij}(k_x)$ is the isotropic part of the spectrum, which is zero for all $i \neq j$. The elements of the spectral anisotropy tensor for a two-dimensional mean flow then reads:

$$E'_{ij}(k_x) = \begin{pmatrix} E_{xx} - E^o_{xx} & E_{xr} & 0 \\ E_{rx} & E_{rr} - E^o_{rr} & 0 \\ 0 & 0 & E_{\theta\theta} - E^o_{\theta\theta} \end{pmatrix} \quad (6.19)$$

The cross correlation spectra $E_{x\theta}(k_x) = E_{\theta x}(k_x)$ and $E_{r\theta}(k_x) = E_{\theta r}(k_x)$ vanish, since integration of these over all wave numbers is zero. It is difficult to imagine a spectral distribution which is different from zero, and which at the same time always integrates to zero. It is important to note that the definition of the spectral anisotropy tensor deviates from the Reynolds stress anisotropy tensor (b_{ij}), since the isotropic form of the streamwise spectrum differs from the one for the two lateral components. Thus the isotropic spectra can not be expressed in the simple form $E^o_{ij}(k_x) = 1/3\delta_{ij}E_{kk}$, which causes the basic difference compared to the definition of b_{ij} ¹. From $\tau'_{kk} = 0$ it follows that $E'_{kk} = 0$, thus

$$E'_{kk}(k_x) = E_{kk}(k_x) - E^o_{kk}(k_x) = 0 \quad (6.20)$$

The isotropic relation between the two lateral and streamwise one-dimensional spectra is given by (see Hinze [25]):

$$E^o_{rr}(k_x) = E^o_{\theta\theta}(k_x) = \frac{1}{2} \left[E^o_{xx}(k_x) - k_x \frac{\partial E^o_{xx}(k_x)}{\partial k_x} \right] \quad (6.21)$$

¹Yeung and Brasseur [66] defined the spectral anisotropy tensor $A_{ij} = [E_{ij}(k)/E_{ii}(k)] - 1/3\delta_{ij}$, which has the identical form as b_{ij} . This definition was applied to direct numerical simulations, where k was taken as the norm of the wave number vector, which must not be confused with the wave number component k_x .

Combining Eq. 6.20 and Eq. 6.21, a differential equation for the streamwise isotropic spectrum $E_{xx}^o(k_x)$ is obtained as,

$$k_x \frac{\partial E_{xx}^o(k_x)}{\partial k_x} - 2E_{xx}^o(k_x) + E_{kk}(k_x) = 0 \quad (6.22)$$

This first order differential equation for $E_{xx}^o(k_x)$ may be solved using the measured $E_{kk}(k_x)$ once an initial value for $E_{xx}^o(k_x)$ has been defined. Applying the classical hypothesis of a universal isotropic region at high wave number, the solution is subjected to the condition,

$$\lim_{k_x \rightarrow \infty} E_{xx}^o(k_x) = \lim_{k_x \rightarrow \infty} E_{xx}(k_x) \quad (6.23)$$

Due to the small values of the spectra in this region, an error in the initial value, will cause only a small bias to the solution at lower wave number, and should therefore not be crucial for the calculation of $E_{xx}^o(k_x)$ at larger scales. A review of small scale turbulence by Sreenivasan & Antonia [58], states that shortcomings of small scale turbulence research, is due to lack of high enough Reynolds number data. In the literature one may find results which both support and contradict local isotropy. Since there exists no conclusive results on small scale anisotropy, the classical hypothesis of a universal isotropic range is assumed valid. Departure from local isotropy may be estimated by comparing the measured spectrum $E_{rr}(k_x)$ and the calculated isotropic spectrum $E_{rr}^o(k_x)$ in the high wave number range. If the large scales are near isotropic, e.g. on the centre line of fully developed pipe flow, it should be of interest to consider isotropy also in the inertial range. The Kolmogorov inertial range of the streamwise spectrum reads

$$E_{xx}(k_x) \sim k^{-5/3} \quad (6.24)$$

Introduced in the isotropic expression (Eq. 6.21) for the two lateral spectra, the isotropic expression for the inertial range becomes:

$$E_{rr}(k_x) = E_{\theta\theta}(k_x) = \frac{4}{3} E_{xx}(k_x), \quad (6.25)$$

which may be used to describe the degree of isotropy. In chapter 4 and 5, it was found that for moderate turbulent Reynolds numbers no inertial range appeared in the lateral spectra. The inertial range test on isotropy is therefore at least restricted to higher turbulent Reynolds numbers. Even if the

inertial range is not isotropic, it is still reasonable to believe that the dissipation range is near isotropic. At least sufficient to provide an acceptable boundary condition for $E_{xx}^o(k_x)$. Proceeding with a numerical solution of Eq. 6.22, the isotropic spectrum $E_{xx}^o(k_x)$ is obtained, and $E_{rr}^o(k_x) = E_{\theta\theta}^o(k_x)$ can then be derived from Eq. 6.21. From the measured spectra and the calculated isotropic spectra, the spectral anisotropy tensor follows from the definition given by Eq. 6.18. Similar to the analysis of Lumley [42], a normalized spectral anisotropy tensor $c_{ij}(k_x)$ may be defined by a proper scaling of $E'_{ij}(k_x)$,

$$c_{ij}(k_x) = \frac{1}{\bar{u}_k u_k} E'_{ij}(k_x) \quad (6.26)$$

This scaling is chosen such that the definition of $c_{ij}(k_x)$ relates directly to the anisotropy tensor b_{ij} . It may easily be verified that

$$\int_o^\infty E_{xx}^o(k_x) dk_x = \int_o^\infty E_{rr}^o(k_x) dk_x = \int_o^\infty E_{\theta\theta}^o(k_x) dk_x = \frac{\bar{u}_k u_k}{3}, \quad (6.27)$$

hence the time averaged and spectral anisotropy elements relates as:

$$\int_o^\infty c_{ij}(k_x) dk_x = b_{ij} \quad (6.28)$$

The restrictions which are related to b_{ij} must therefore also apply to the integral of c_{ij} , such that,

$$\int_o^\infty c_{ij}(k_x) dk_x \in [-1/3, 2/3] \quad (6.29)$$

Similar to the time mean values it is possible to deduce the invariants for c_{ij} . To save some writing $c_{ij}(k_x)$ is replaced by c_{ij} and $E_{ij}(k_x)$ by E_{ij} . Using the notation of Lumley, the corresponding invariants \hat{I}_2 and \hat{I}_3 read:

$$\hat{I}_2 = -\frac{1}{2} (c_{xx}^2 + c_{rr}^2 + c_{\theta\theta}^2 + 2(c_{xr}^2 + c_{x\theta}^2 + c_{r\theta}^2)) \quad (6.30)$$

$$\hat{I}_3 = c_{xx} c_{rr} c_{\theta\theta} + 2c_{xr} c_{x\theta} c_{r\theta} - (c_{xx} c_{r\theta}^2 + c_{rr} c_{x\theta}^2 + c_{\theta\theta} c_{rx}^2) \quad (6.31)$$

For a two-dimensional mean flow this reduces to:

$$\hat{I}_2 = -\frac{1}{2} (c_{xx}^2 + c_{rr}^2 + c_{\theta\theta}^2 + 2c_{xr}) \quad (6.32)$$

$$\hat{I}_3 = c_{xx} c_{rr} c_{\theta\theta} - c_{\theta\theta} c_{rx}^2 \quad (6.33)$$

Axisymmetry implies

$$c_{rr} = c_{\theta\theta} = -\frac{1}{2}c_{xx} \quad ; \quad c_{xr} = 0, \quad (6.34)$$

such that the invariants reduce to

$$\hat{I}_2 = -\frac{3}{4}c_{xx}^2 \quad ; \quad \hat{I}_3 = \frac{c_{xx}^3}{4} \quad (6.35)$$

This gives the axisymmetric relation:

$$\hat{I}_2 = -3\left(\frac{\hat{I}_3}{2}\right)^{2/3}, \quad (6.36)$$

which is identical to Eq. 6.11. The corresponding axisymmetric parameter \hat{A} , then reads:

$$\hat{A} = \frac{\hat{I}_3}{2(-\hat{I}_2/3)^{3/2}} \quad (6.37)$$

The state of two-component turbulence does not take the similar simple form as Eq. 6.14. Assuming that the wall-normal component is zero, the anisotropy element c_{rr} will not be constant, but a function of the wave number. The two-component limit takes the more complex form,

$$\beta I_2 - I_3 + \beta^2 = 0 \quad ; \quad \beta = \frac{E_{rr}^o(n)}{\bar{u}_k u_k} \quad (6.38)$$

For each wave number this represents a straight line, as in the AIM ($\beta = -1/3$), but the slope and zero-intercept must be different for each turbulent scale. Energy containing scales are restricted by a larger triangle, and less energy containing scales are restricted by a smaller triangle. It is therefore clear that the spectral invariant map does not represent the similarly well defined restrictions as the AIM, since the triangle is different for each turbulent scale. The method may however be used to describe the different elements of the anisotropy tensor, and provides information on axisymmetry.

6.2.1 Solution algorithm

Calculation of the spectral anisotropy tensor involves the measured spectra $E_{ij}(k_x)$. The present procedure involves both integration and differentiation.

The spectra are subjected to local scatter, which causes undesirable local gradients. To avoid scattered results the spectra were fitted to the polynomial form:

$$\ln [E_{ij}(k_x)] = c_0 + c_1(\ln k_x) + c_2(\ln k_x)^2 + \dots + c_7(\ln k_x)^7, \quad (6.39)$$

which matched the data very well for the whole wave number range. The calculation procedure was also performed by using the measured spectra directly. The same result was obtained, however with a larger scatter. The solution algorithm is pictured schematically in Fig. 6.6. The numerical procedure for calculating the streamwise isotropic spectra may be expressed as:

$$E_{xx,i}^o = \left\{ \frac{E_{xx,i+1}^o + \alpha E_{kk,i}}{1 + 2\alpha} \right\}; \quad \alpha = \frac{k_{x,i+1} - k_{x,i}}{k_{x,i}}, \quad (6.40)$$

which is a simple forward Euler iteration. The calculation was repeated with different increment size (Δk_i), to ensure an accurate solution. The accuracy of the isotropic spectrum E_{xx}^o is therefore believed to follow the accuracy of the measured power spectra. The iteration was performed from the right to the left boundary, since the boundary condition is decided from the highest wave number (assumption of isotropy). The isotropic lateral spectra are calculated from:

$$E_{rr,i}^o = \frac{1}{2} \left\{ E_{xx,i}^o - \frac{E_{xx,i+1}^o - E_{xx,i}^o}{\alpha} \right\}, \quad (6.41)$$

which is a straight forward discretization of Eq. 6.21, with a first order accuracy of the differential term.

6.3 Measured Spectral Invariants

The method described in the previous section is applied to turbulence spectra obtained in the fully developed pipe flow. The measured spectra are presented in chapter 4, where the reader may also find a description of the experimental procedure. The bulk Reynolds number was $Re = 75.000$. Table 6.2 shows some control parameters which indicate the accuracy of the procedure. For all locations examined, the integrated isotropic spectra were within 4% of $\overline{u_k u_k}/3$. The integral of the anisotropy elements $c_{ij}(k_x)$ compared within 8% of the corresponding b_{ij} . The trace of $c_{ij}(k_x)$ was close to zero for all

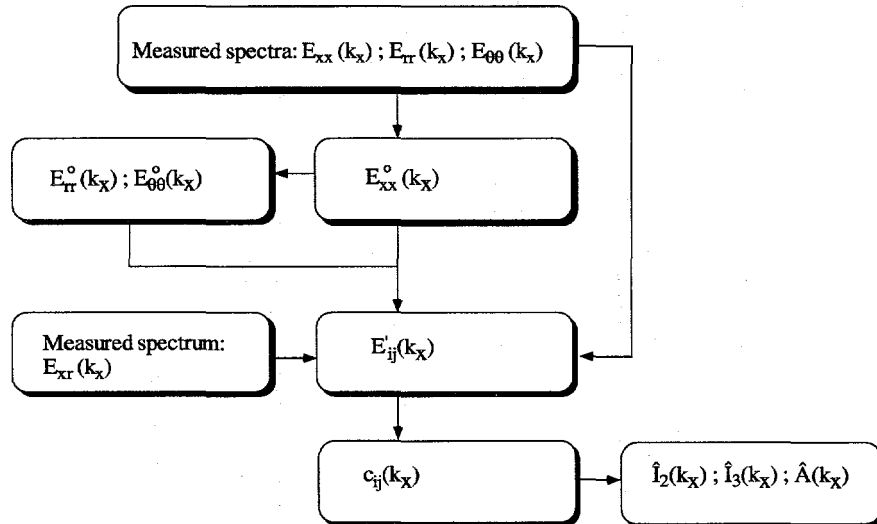


Figure 6.6: Numerical procedure for calculating anisotropy spectra.

wave numbers, which confirms Eq. 6.20. Figure 6.7 shows the calculated isotropic streamwise and radial power spectra, compared to $E_{kk}(k_x)/3$. Recall that the isotropic circumferential and radial spectra are identical. The spectra are multiplied with the wave number, such that the area under each graph corresponds to $\overline{u_k u_k}/3$. The result shows why $E_{kk}(k_x)/3$, as used by Yeung and Brasseur [66], does not represent the isotropic part of the spectra. The isotropic lateral spectrum conserves energy at larger wave numbers compared to the streamwise spectrum. It is essential to include this effect when calculating the anisotropy spectra.

6.3.1 Elements of the spectral anisotropy tensor

Figure 6.8 and 6.9 show the elements of the spectral anisotropy tensor $c_{ij}(k_x)$, for various locations from near the wall to the core region. Figure 6.8 (a) represents $y/R = 0.09$, corresponding to $y^+ = 160$. The result clearly shows that the circumferential anisotropy element $c_{\theta\theta}(k_x)$ tend towards isotropy

Table 6.2: Check parameters for the spectral analysis in fully developed pipe flow.

y/R	$\frac{\int_o^\infty E_{xx}^o(k_x)}{\bar{u}_k \bar{u}_k / 3}$	$\frac{\int_o^\infty E_{rr}^o(k_x)}{\bar{u}_k \bar{u}_k / 3}$	$\frac{\int_o^\infty c_{xx}(k_x)}{b_{xx}}$	$\frac{\int_o^\infty c_{rr}(k_x)}{b_{rr}}$	$\frac{\int_o^\infty c_{\theta\theta}(k_x)}{b_{\theta\theta}}$
0.087	0.98	1.01	0.97	1.01	1.04
0.30	0.96	0.99	0.97	0.97	0.98
0.43	0.99	1.02	1.02	1.01	1.04
0.65	0.97	0.99	1.03	1.06	1.03
0.87	0.98	1.00	1.02	1.06	0.96
0.92	0.98	0.99	1.05	1.08	1.02

($c_{\theta\theta}(k_x) = 0$) at lower wave numbers than $c_{rr}(k_x)$ for all positions y/R . For the present flow situation, turbulence production only enter the streamwise component, which is why the streamwise spectral anisotropy element ($c_{xx}(k_x)$) is expected to be positive for all wave numbers, at least in the range of significant production. This is seen to be supported by the present results. The explanation for the difference in the two lateral components must be related to the redistribution of energy from the streamwise component. The redistribution process is controlled by the pressure-strain interaction, normally assumed to have the property of making turbulence more isotropic. Most Reynolds stress turbulence models are based on the linear "return to isotropy" model by Rotta [51] (See Aronson and Löfdal [6]), at least for the slow part of the pressure strain. The present result indicate that the pressure-strain transfers more energy to the circumferential than the radial component, due to the restriction of the wall on the radial motion at this location. The result indicate that there is a stronger connection between the streamwise and circumferential fluctuations than the streamwise and radial fluctuations. This observation is supported by the near wall behaviour of the turbulent fluctuations, where the radial fluctuations are described by higher order terms in the series expansion, compared to the other two. Figure 6.8 (b) represents $y/R = 0.30$, corresponding to $y^+ = 552$, which is at the outer edge of the logarithmic region. At this position the largest scales ($Rk_x < 1$) appear to be axisymmetric, since the two lateral anisotropy elements collapse. However it is clear that since the turbulence production is not zero, which is indicated by $c_{xx}(k_x) \neq 0$, this state can not be truly axisymmetric (note that

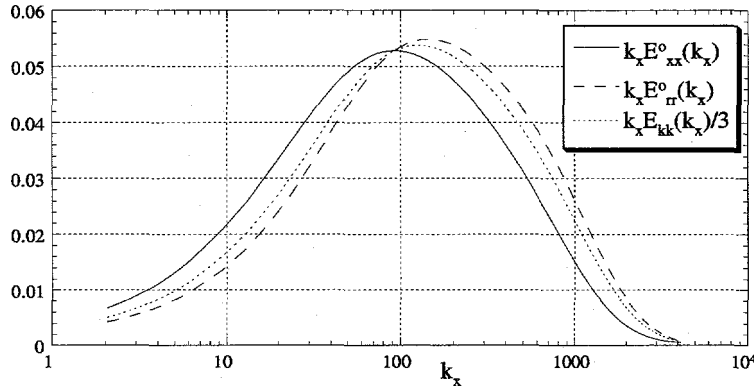


Figure 6.7: Compensated isotropic streamwise and lateral spectrum $k_x E_{xx}^o(k_x)$ (solid) $k_x E_{rr}^o(k_x)$ (dashed), compared to $E_{kk}(k_x)/3$ (dotted): $y/R=0.92$.

$c_{xr}(k_x) > 0$ due to the cylindrical coordinate notation). The same argument was used for the time averaged statistics. Even if the two lateral anisotropy spectra closely follow each other in the low wave number range, significant differences are found for $Rk_x > 1$, for which the main part of the production occurs. Moving further towards the core region, $c_{xr}(k_x)$ is reduced and the two lateral elements $c_{rr}(k_x)$ and $c_{\theta\theta}(k_x)$ approach each other. At $y/R = 0.92$ (Fig. 6.9 (f)) $c_{rr}(k_x) \simeq c_{\theta\theta}(k_x)$ for entire wave number range, and $c_{xr}(k_x)$ is about to vanish. The latter is truncated at $Rk_x = 15$, since the fluctuations in the cross correlation spectrum was too large for an accurate polynomial fit. For the centre line location, which is not shown here, $c_{rr}(k_x)$ collapsed with $c_{\theta\theta}(k_x)$ and $c_{xr}(k_x)$ vanished by definition. The results indicate that only for the centre line location are all scales axisymmetric. At a location only slightly away from the centre line, deviation from axisymmetry is found in the intermediate scales. However for wave numbers less than $Rk_x \simeq 1$, which corresponds to length scales larger than the pipe radius, the turbulence spectra remain axisymmetric, except very near the wall, where the flow is mainly controlled by events originating from the nearest wall.

6.3.2 Spectral axisymmetry

For the classical invariant analysis of the Reynolds stress tensor, Lee and Reynolds [37] suggested that the parameter A , given by Eq. 6.12, may be

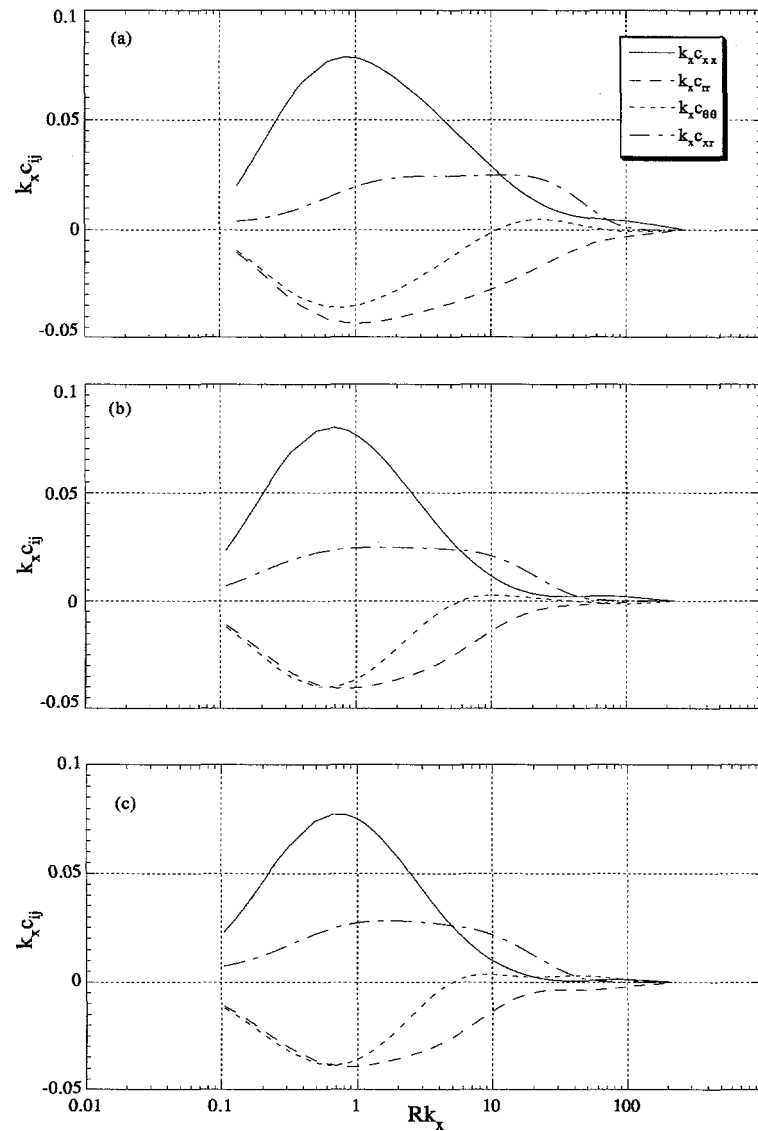


Figure 6.8: Elements of spectral anisotropy tensor: (a) $y/R=0.09$; (b) $y/R=0.30$; (c) $y/R=0.43$.

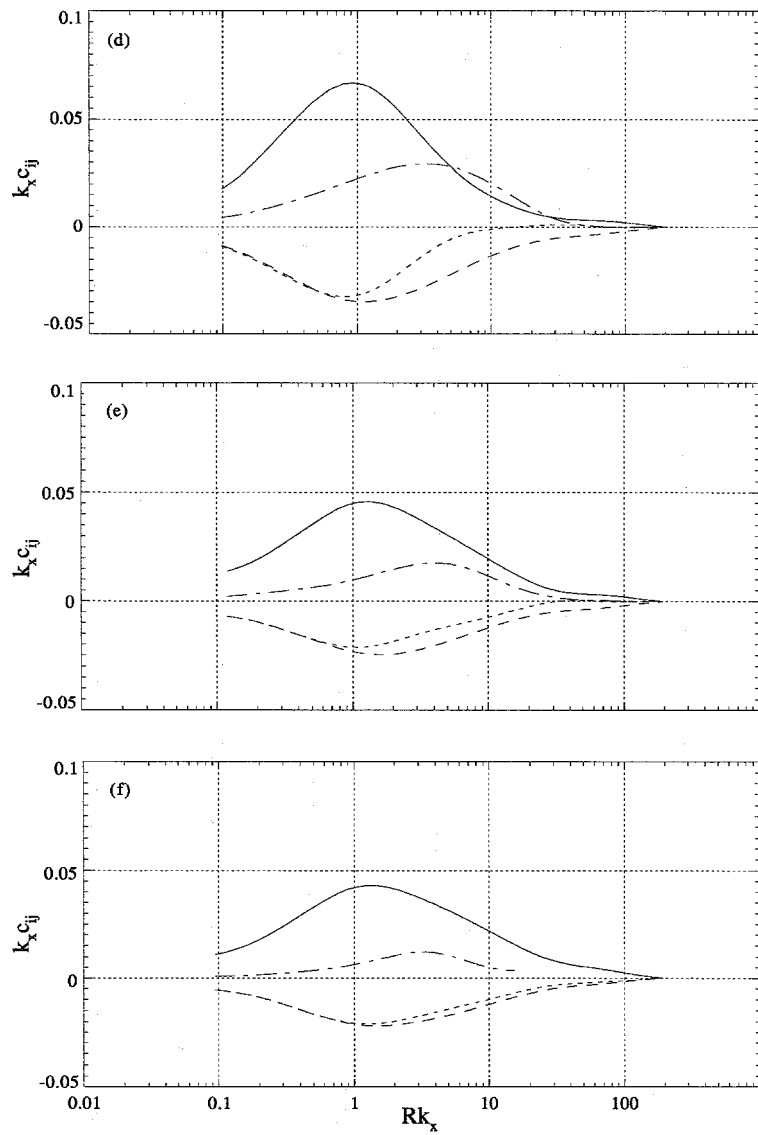


Figure 6.9: Elements of spectral anisotropy tensor: (d) $y/R=0.65$; (e) $y/R=0.87$; (f) $y/R=0.92$. For caption see Fig 6.8.

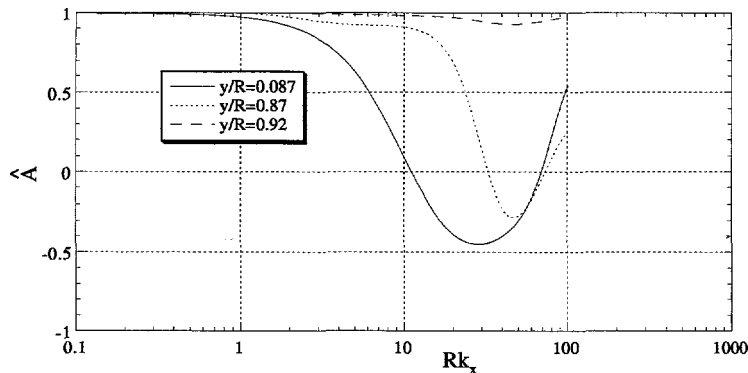


Figure 6.10: Parameter \hat{A} describing axisymmetry, at three different locations.

used to separate the two different modes of axisymmetry. Figure 6.10 shows the spectral equivalent \hat{A} , obtained from the anisotropy spectra presented in the previous section, for the locations $y/R = 0.087, 0.87$ and 0.92 . The results indicate that when approaching the core region, the spectra remain axisymmetric into gradually higher wave numbers. The result has been truncated at $Rk_x = 100$, due to large oscillations between ± 1 in the high wave number range. The oscillations are due to the approach towards isotropy, for which the parameter \hat{A} becomes singular. The parameter is therefore not found convenient for examining the high wave number range, but still provide information on deviation from axisymmetry in the larger scales. It can be seen that for the location close to the wall, the parameter \hat{A} obtains negative values over a wide range of wave numbers. This indicates a deviation from the "disc-like" structure. However it is too ambiguous to conclude that these scales are closer to a "rod-like" structure ($A = -1$).

6.4 Conclusions

The second (I_2) and third (I_3) invariants of the Reynolds stress anisotropy tensor (b_{ij}) have been examined for fully developed pipe flow. The combination of I_2 and I_3 in the core region of the flow is found to closely follow the right axisymmetric line in the anisotropy invariant map. The centre line location deviates only marginally from a state of isotropic turbulence. When approaching the wall the invariants separate slowly from the axisymmetric

line, and then makes a distinct jump away from this near $y/R = 0.2$. This "jump" is believed to represent a separation between the core region and the near wall region. The "jump" becomes less clear as the Reynolds number decrease, and is barely visible for the lowest Reynolds number of $Re = 22.000$. Mansour et al. [43] reported an anisotropy invariant map based on the DNS channel data of Kim et al. [32]. These results show a similar effect, however not as pronounced as the present results. The present low Reynolds number data closely follow the DNS pipe flow data of Eggels et al. [21].

A spectral anisotropy analysis is suggested. The method is based on the same idea as the anisotropy tensor for the Reynolds stress tensor (b_{ij}). However the definition of the spectral anisotropy tensor $c_{ij}(k_x)$ is different from b_{ij} , since the isotropic streamwise spectrum is different from the two isotropic lateral spectra. The invariants of $c_{ij}(k_x)$ have been derived in the same way as for the classical theory of Lumley [42]. The spectral anisotropy tensor does not however relate to the same well defined anisotropy invariant map as b_{ij} , since the limits of two-component turbulence depend on the wave number.

The method is applied to turbulence spectra obtained in fully developed pipe flow. The four non-zero elements of the spectral anisotropy tensor are reported for different locations from near the pipe wall towards the centre line. A significant difference in the wave number dependence was found in the anisotropy of the circumferential and radial spectra, except at the centre line. This difference must be related to the difference in redistribution of energy from the streamwise to the two lateral spectra. The circumferential spectra adapts to a near isotropic state at significantly lower wave numbers than the radial spectra. Another important observation is that even quite close to the pipe wall, the largest scales ($Rk_x < 1$) still remain axisymmetric.

The second and third invariants for the spectral anisotropy tensor are expressed in terms of the parameter \hat{A} , introduced by Lee and Reynolds [37] for the invariants of b_{ij} . The parameter was suggested to distinguish between the two different modes of axisymmetry, denoted as "rod" and "disk" like turbulence. For the spectral invariants, the parameter \hat{A} displays at which wave number the turbulence spectra deviate from axisymmetry. The parameter describes the persistence of axisymmetry from the large scales into the smaller scales. However the parameter is found not convenient for describing the high wave number range of the spectra, since the approach towards isotropy tend to make \hat{A} unstable.

Chapter 7

Quadrant Analysis

Turbulence is a stochastic phenomenon, though not random. It is a common belief that turbulence may be described by dominating coherent structures, superimposed on random turbulence. The non-random part is assumed to be responsible for the transfer of energy from the mean flow to the turbulence, which is commonly referred to as turbulence production. The coherent motions are therefore believed to carry important information on the turbulence structure. As stated by Hussain [26]: "The interaction between coherent structures and incoherent turbulence, is the most critical and least understood aspect of turbulent shear flows". Another important aspect, is the influence on coherent structures on heat and mass transfer. Coherent structures also play an important role in e.g. sediment accumulation in pipe systems. Strong events will influence on the transport of particles between the low speed wall region and the high speed core region.

One of the basic challenges is the three-dimensional character of the structures, which is difficult to capture with the available experimental techniques. Direct numerical simulations have supplied important information, although these results are limited to low Reynolds numbers. This problem also arises in different visualisation techniques.

A number of experimental and numerical results are reported for turbulent boundary layers and channel flows. Different techniques have been applied, which has provided important information on characteristic strength, duration and time between events. For fully developed pipe flow, results are available from Sabot and Comte-Bellot [52]. These results were obtained with hot-wire anemometry, using analogue procedures to calculate conditional averages and characteristic time scales. Advances in computer technology, has

opened new opportunities. It is now possible to store large numbers of data, and then perform the post-processing. The same set of data may be analysed in different ways and with variable sets of parameters. In turbulent shear layers, the dominating coherent motions are found to initiate near the wall, and are commonly described as "low-speed fluid ejecting outward from the wall". Turbulent pipe flow is expected to reflect a similar near wall behavior as e.g. boundary layers. However, the characteristic time scales are expected to behave differently, due to the totally wall-bounded nature of the flow. The intermittent character of the outer part of a boundary layer does not appear in the core region of the pipe flow. The flow has a focus on the pipe center line. A fluid "package" which is ejected away from the wall is restricted to an increasingly smaller area when approaching the center line. The core region is established from the integrated history of different events, originating from arbitrary positions on the periphery. Sabot and Comte-Bellot [52] found that the strongest events persisted to $y/R = 1.3$ into the opposite half of the cross section.

7.1 Quadrant Decomposition

Since the time averaged shear stress $\overline{u_x u_r}$ in fully developed pipe flow is everywhere positive, the dominating events must be related to positive correlations of $u_x u_r$. This means that the instantaneous streamwise and radial velocity fluctuations must appear with the same sign, but may be both positive and negative. These motions are commonly described as sweeps and ejections respectively.

One of the most common methods used to detect characteristic events, is the quadrant decomposition which was first suggested by Lu and Willmarth [39]. The instantaneous u_x and u_r signal are sorted into four different classes of events, described in cylindrical coordinates in Table 7.1. A detection is said to occur when the instantaneous $u_x u_r$ correlation exceeds a specified level, H , such that

$$|u_x u_r| > H(\overline{u_x^2})^{1/2}(\overline{u_r^2})^{1/2} \quad (7.1)$$

Contribution to the shear stress from the different quadrants may then be calculated from,

$$\overline{u_x u_r}|_n = \overline{u_x u_r F_n} \quad (7.2)$$

Table 7.1: Quadrant decomposition of Lu and Willmarth [39].

Q_1	$u_x > 0$	$u_r < 0$	"outward interaction"
Q_2	$u_x < 0$	$u_r < 0$	"Ejection"
Q_3	$u_x < 0$	$u_r > 0$	"Inward interaction"
Q_4	$u_x > 0$	$u_r > 0$	"Sweep"

were $F_n = 1$ if the event is in quadrant Q_n , and $F_n(t) = 0$ otherwise.

Contribution to the streamwise and wall normal Reynolds stresses from the four different quadrants of the shear stress signal, can be expressed as

$$\overline{u_x^2}|_n = \overline{u_x u_x F_n} \quad (7.3)$$

$$\overline{u_r^2}|_n = \overline{u_r u_r F_n} \quad (7.4)$$

This provides information on which quadrants that contribute most to the two normal stresses.

7.2 Results

7.2.1 Decomposition of the $\overline{u_x u_r}$ -signal

Figure 7.1 shows the contribution to $\overline{u_x u_r}$ from the four different classes of events, for $Re = 35.000$ and $Re = 75.000$ respectively. The two experiments are addressed as (C) and (D) in Table 3.1. The results are scaled with the friction velocity and the threshold is $H=0$, thus a summation of all four quadrants equals $\overline{u_x u_r}^+$. No significant difference can be observed between the two Reynolds numbers. The contribution from the second quadrant is everywhere the largest, however closely followed by the fourth quadrant. The contribution from the outward (Q_1) and inward (Q_3) interactions are approximately equal over the entire cross section. On the pipe center line axisymmetry implies $\overline{u_x u_r}|_1 = \overline{u_x u_r}|_4$, and $\overline{u_x u_r}|_2 = \overline{u_x u_r}|_3$, which is seen to be satisfied at both Reynolds numbers.

Figure 7.2 compares the relative contribution to the shear stress in fully developed pipe flow with zero pressure gradient (ZPG) boundary layer data.

The results are presented as function of y^+ . Inside the logarithmic wall region, the two experiments give the same quadrant distributions. This suggests that the near wall behaviour of the shear stress is mainly controlled by the nearest wall, and in less extent influenced by events originating from the outer region.

Figure 7.3 shows the contribution from the four quadrants at $y/R = 1$ and $y/R = 0.4$, for different threshold level. On the pipe center line the strongest events ($H > 4$) appear in the second and third quadrant. The strong events in the third quadrant is due to second quadrant events originating from the opposite wall, thus reflects the axisymmetry. At $y/R = 0.4$ the most violent events ($H > 4$) are restricted to the second quadrant. The results confirm the findings of Sabot and Comte-Bellot [52], who suggested that $H = 4 - 4.5$ should be taken as appropriate threshold level for the most violent events. The two Reynolds numbers show no significant difference.

7.2.2 Conditional average of $\overline{u_x^2}$ and $\overline{u_r^2}$

Figure 7.4 and 7.5 show the conditional contribution to the streamwise and radial turbulence intensity respectively, for $Re = 35.000$ and $Re = 75.000$. The threshold level is $H = 0$.

Similar to the shear stress, the main contribution to both normal stresses come from the second and fourth quadrant. The contribution from the inactive motions (Q_1 and Q_3) collapse in most of the cross section. When approaching the center line ($y/R > 0.7$) the contribution from the first and third quadrant increase, due to second and fourth quadrant events originating from the opposite half of the cross section. This supports the findings of Sabot and Comte-Bellot [52], suggesting that the strongest events persisted to $y/R = 1.3$ into the opposite half of the cross section.

7.3 Conclusions

The quadrant decomposition of Lu and Willmarth has been applied to the shear stress signal, obtained in fully developed pipe flow.

Results are reported for $Re=35.000$ and $Re=75.000$. No significant Reynolds number effect was found.

Contribution to the shear stress is dominated by the second quadrant, closely followed by the fourth quadrant. Contribution from the first and the

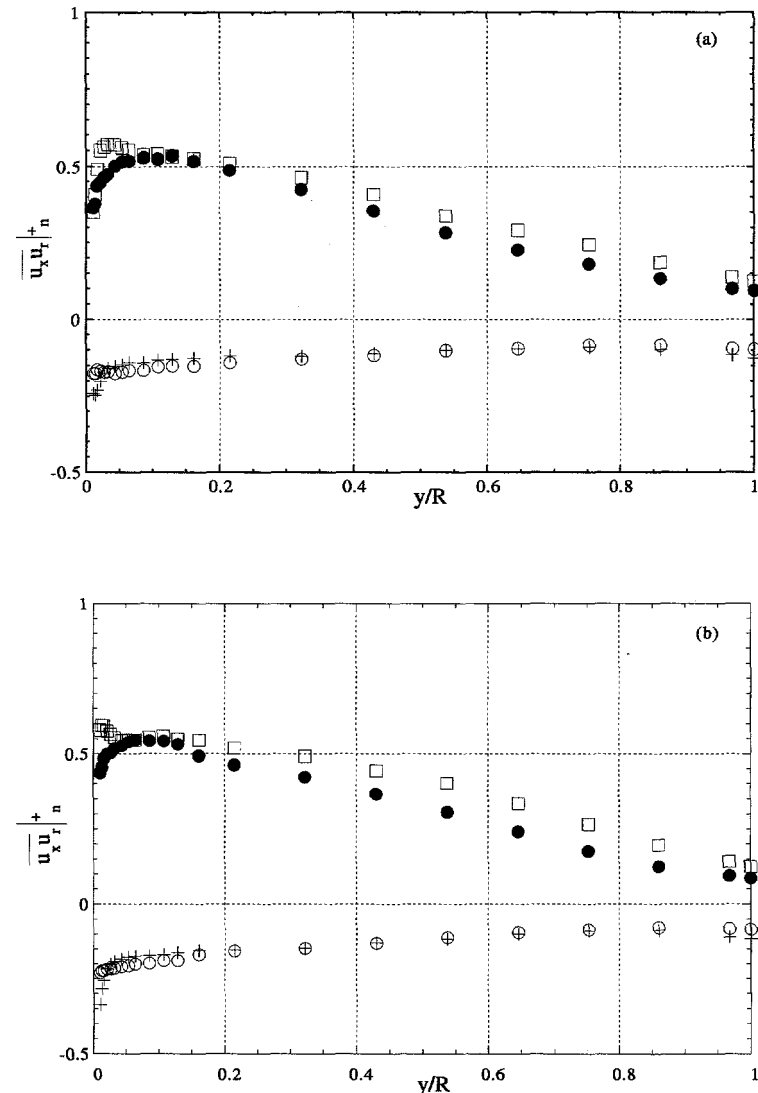


Figure 7.1: Quadrant decomposition ; $\bar{u}_x \bar{u}_r|_1^+$ (\circ), $\bar{u}_x \bar{u}_r|_2^+$ (\square), $\bar{u}_x \bar{u}_r|_3^+$ (+), $\bar{u}_x \bar{u}_r|_4^+$ (\bullet) : Threshold $H = 0$: $Re = 35.000$ (a), $Re = 75.000$ (b)

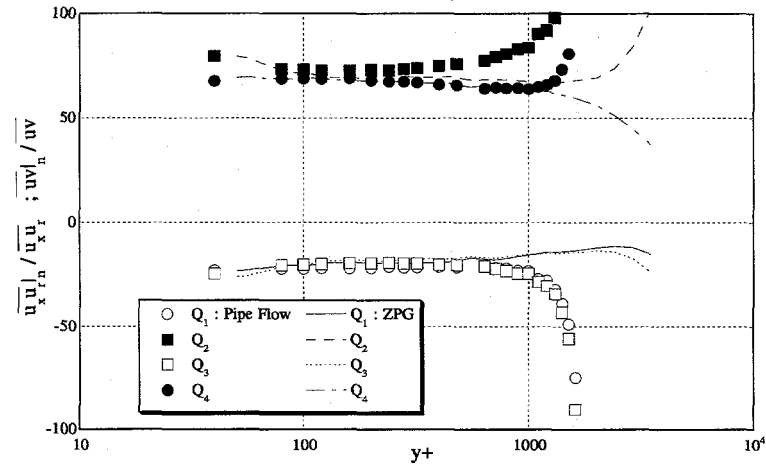


Figure 7.2: Relative contribution to the shear stress in fully developed pipe flow, compared to zero pressure gradient (ZPG) boundary layer data ($R_\theta = 12600$).

third quadrant collapse, except very close to the wall.

Near the wall the relative contribution to the shear stress from the different quadrants compare with zero pressure gradient boundary layer data. This suggests that the region is mainly controlled by events originating from the nearest wall, almost unaffected by the core region.

Contribution to the streamwise and radial normal stresses from the different quadrants are reported. Both normal stresses are dominated by the second and fourth quadrant.

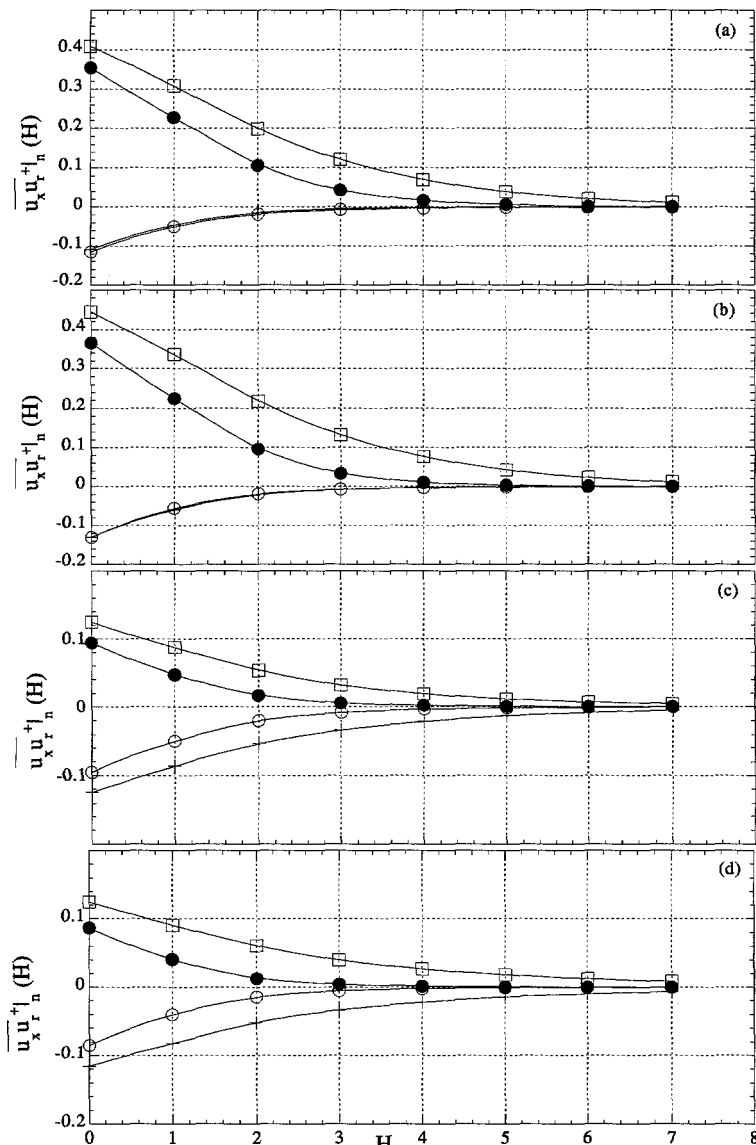


Figure 7.3: Quadrant decomposition with various threshold (H) ; $\overline{u_x u_r}^+_1$ (●), $\overline{u_x u_r}^+_2$ (+), $\overline{u_x u_r}^+_3$ (□), $\overline{u_x u_r}^+_4$ (○) : $Re = 35.000$ (a,c), $Re = 75.000$ (b,d): $y/R = 0.4$ (a,b), $y/R = 1.0$ (c,d)

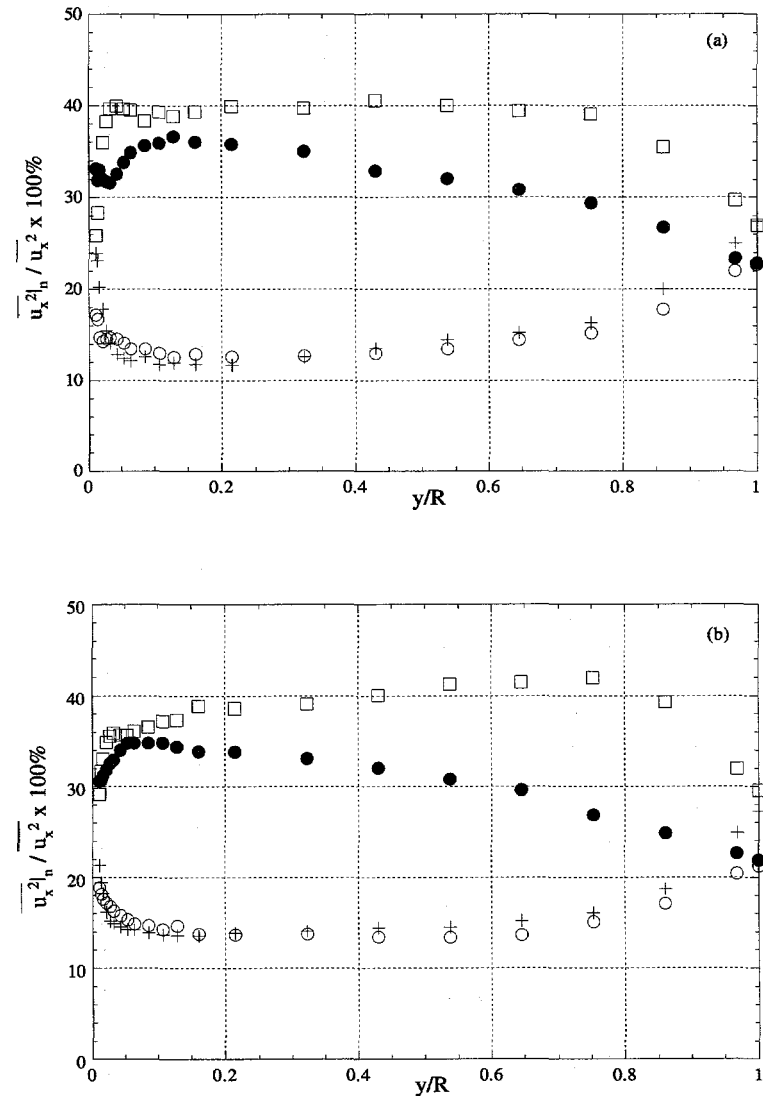


Figure 7.4: Quadrant decomposition ; $\overline{u_x^2}|_1$ (o), $\overline{u_x^2}|_2$ (□), $\overline{u_x^2}|_3$ (+), $\overline{u_x^2}|_4$ (●) : Threshold $H = 0$: $Re = 35.000$ (a), $Re = 75.000$ (b)

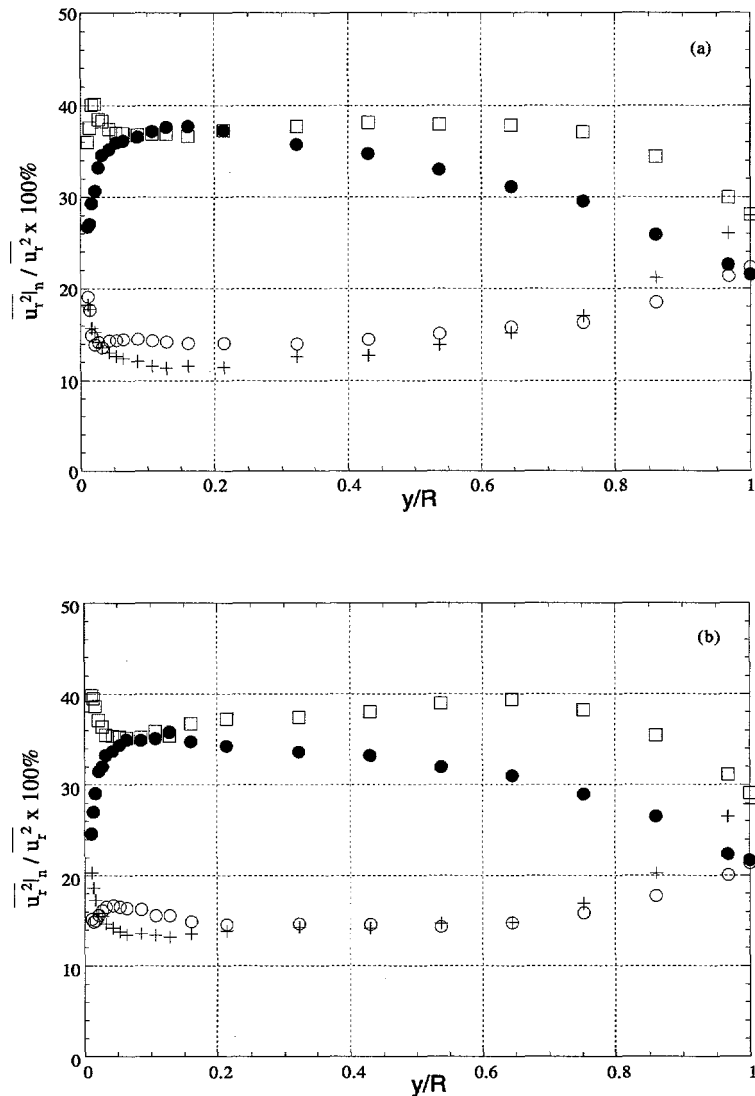


Figure 7.5: Quadrant decomposition ; $\overline{u_r^2}|_1$ (o), $\overline{u_r^2}|_2$ (□), $\overline{u_r^2}|_3$ (+), $\overline{u_r^2}|_4$ (•) : Threshold $H = 0$: $Re = 35.000$ (a), $Re = 75.000$ (b)

Chapter 8

Axisymmetric Contraction

8.1 Motivation

A renowned phenomenon of turbulence is that a mean flow acceleration reduces the streamwise normal stress more than the two lateral. This property has been extensively applied to e.g. wind tunnel design, to reduce the turbulence level and make it more isotropic. Comte-Bellot and Corrsin [18] reported isotropisation of grid turbulence after a 1.27 area ratio contraction. Recent experiments by Sjögren [55], downstream of a 9:1 area wind tunnel contraction, produced a state of axisymmetric and near two-dimensional turbulence. Obviously this implies strong anisotropy, due to the dominating cross-stream fluctuations. Tennekes and Lumley [60] presented a visual picture of streamwise vortex stretching, which increases the vortex angular velocity, thus suppressing streamwise fluctuations in favour of cross-stream fluctuations. The phenomenon is clearly connected to the influences of redistribution (pressure-strain) and secondary production terms, caused by the streamwise acceleration. A study of axisymmetric contraction shapes has been reported by Hussain and Ramjee [27]. In these experiments the different contractions were mounted 0.53 diameters downstream of a screen. The present study addresses the effect of axisymmetric contraction of an initially fully developed pipe flow¹, which means that the flow entering the contraction is slightly different from the investigation by Hussain and Ramjee. The contraction was designed to produce a constant acceleration, thus a constant

¹The essence of this chapter is accepted to: The 13th Australasian Fluid Mechanics Conference, Melbourne, Australia, Dec.1998 [62]

streamwise strain. Changes to the Reynolds stress tensor are reported and related to some of the terms in the Reynolds stress transport equations. The behaviour of the turbulence spectra inside the contraction are particularly interesting, since secondary production terms, which appear in all three normal components, should cause significant changes to the energy distribution. To examine the spectral inter-component exchange of energy, detailed turbulence spectra were obtained. These results are also presented in terms of the spectral anisotropy tensor introduced in chapter 6. One of the intentions of this work was to establish an experimental basis for a geometrically simple flow situation, which still remains a challenge to turbulence modelling. The present results on the spectral behaviour should provide important information for Large Eddy and Direct Numerical simulations.

8.2 Contraction Design

In most practical flow situations, involving internal area reduction, the confining geometry is decided from "best performance" criteria. E.g. a wind tunnel contraction is normally designed to produce a uniform mean velocity field, with a minimum turbulence intensity. In pipe flow systems, area reductions are normally designed to give a minimum pressure loss. The purpose of the present investigation was to examine the effect of the straining process itself, and not to produce a predefined exit condition. The contraction was therefore designed to give a constant flow acceleration, thus a constant streamwise strain. To achieve an entrance curvature from the pipe to the contraction that would not disturb the upstream fully developed flow, the geometry of the entrance region was made with a curvature equal to the pipe diameter. This means that the constant streamwise strain rate will be present only in the last 72% of the contraction. The total length of the contraction is $L = 600$ mm. The non-dimensional distance from the contraction entrance is defined as $\eta = x/L$. The contraction ratio (ξ) is defined as the ratio of the inlet area to the local area. The inlet diameter of $D = 186$ mm and the outlet diameter equal to $D_e = 65.8$ mm gives a maximum contraction ratio of $\xi = 8$. The geometry of the contraction is shown in Fig. 8.1 and 8.2, and given in tabular form in Tab. 8.1. The position of the pressure tappings are given in Tab. 8.2. Figure 8.3 pictures the definition of the coordinate systems used. A cylindrical system (x, r, θ) is fixed to the symmetry line, with x pointing in the streamwise direction, and r in the radial direction. A Cartesian system

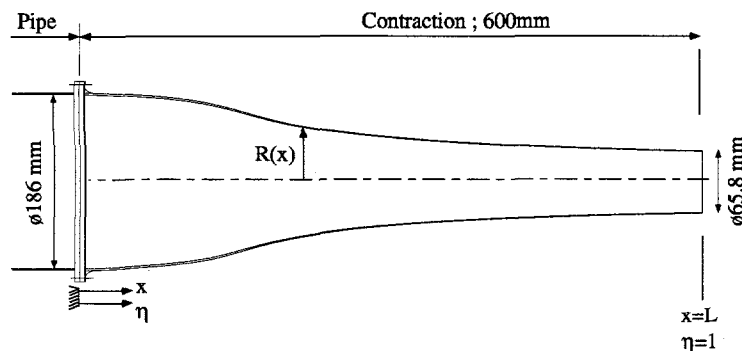


Figure 8.1: Contraction design.

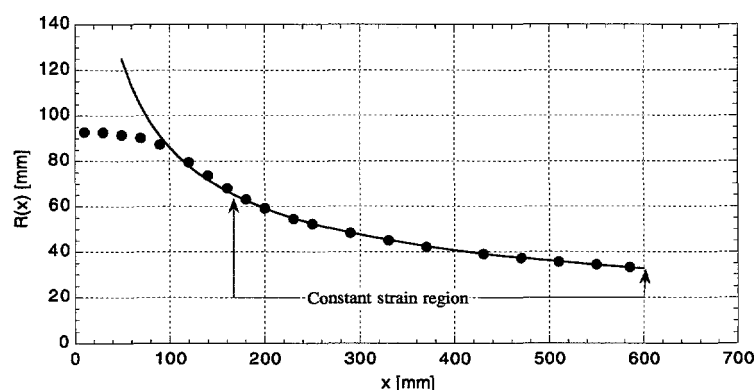
Figure 8.2: Contraction radius as function of distance from the entrance: Actual radius $R(x)$ (●), Radius for constant strain (solid line).

Table 8.1: Contraction coordinates in [mm] (see Fig. 8.1).

x	R(x)	x	R(x)	x	R(x)	x	R(x)
0.0	92.85	110.0	82.50	220.0	56.00	410.0	40.10
10.0	92.85	120.0	79.60	230.0	54.65	430.0	39.20
20.0	92.85	130.0	76.55	240.0	53.40	450.0	38.25
30.0	92.75	140.0	73.60	250.0	52.25	470.0	37.30
40.0	92.30	150.0	70.75	270.0	50.20	490.0	36.45
50.0	91.65	160.0	68.05	290.0	48.35	510.0	35.70
60.0	90.95	170.0	65.50	310.0	46.55	530.0	35.05
70.0	90.25	180.0	63.15	330.0	44.95	550.0	34.45
80.0	89.10	190.0	61.10	350.0	43.55	570.0	33.80
90.0	87.40	200.0	59.25	370.0	42.25	585.0	33.30
100.0	85.15	210.0	57.55	390.0	41.15	600.0	32.88

Table 8.2: Position of pressure tappings, and wall angle (α).

ξ	1	2	3	4	5	6	7	8
$x[mm]$	10	170	243	320	390	460	530	600
$R[mm]$	92.89	65.50	53.06	45.75	41.15	37.77	35.05	32.84
$\alpha[^{\circ}]$	2.8	12.5	6.6	4.3	3.2	2.6	2.0	1.7

(x,y,z) is fixed on the contraction wall, where x is parallel to the symmetry axis, and y is parallel to r, pointing in the opposite direction. In the later part of the contraction, these coordinate systems differ only marginally from the (x',y') system (see Fig. 8.3), where x' is perpendicular and y' is parallel to the streamline.

8.3 Experimental Details

The contraction was mounted at the end of a 80 diameter fetch of smooth straight pipe (Rig II), where the flow has been shown to be fully developed. The pipe diameter was $D = 186$ mm and the bulk velocity $U_o = 2.83$ m/s, giving $Re = \frac{DU_o}{\nu} = 34.000$. A detailed description of the fully developed flow situation may be found in Chapter 3, addressed as experiment (C). At the exit of the contraction the streamwise turbulence intensity was as low as

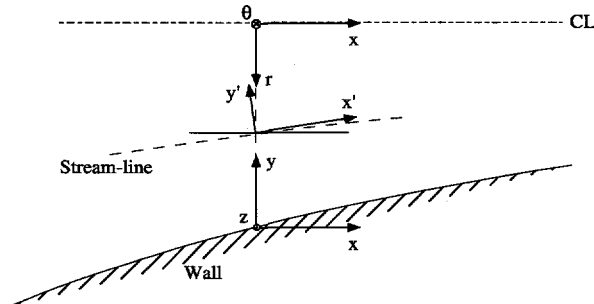


Figure 8.3: Coordinate system.

$Tu_x = (\overline{u_x^2})^{1/2} \cdot 100\% = 0.2\%$. Noise reduction was therefore offered great attention. To remove pressure fluctuations and mechanical vibrations caused by the fan, a stagnation chamber was mounted between the fan and the pipe. The stagnation chamber was supplied with screens and wall damping material. Without the stagnation chamber, pressure waves could be observed as distinct peaks in the streamwise spectrum obtained inside the contraction. By adding the stagnation chamber these peaks were completely eliminated.

The contraction was equipped with static wall pressure tappings at $\xi = 1, 2, \dots, 8$. Assuming that the radial pressure gradient is small, the static wall pressure should give a reasonable approximation of the bulk velocity $\{U_o(\xi)\}$ at each stage, such that

$$U_o(\xi) = \left[\frac{2[P(1) - P(\xi)]}{\rho[1 - (1/\xi)^2]} \right]^{1/2}, \quad (8.1)$$

where P denotes the static wall pressure, and ρ is the fluid density. Figure 8.4 shows that the streamwise acceleration, calculated from the measured static wall pressure, was near constant beyond $x = 170$ mm, with a strain rate of $\partial U_x / \partial x \simeq 40 [1/s]$. Velocity fluctuations were measured by means of hot-wire anemometry. Cross-wire probes were used to cover all non-zero elements of the Reynolds stress tensor $(\overline{u_i u_j})$. Probes were manufactured from $2.5 \mu\text{m}$ diameter Pt-10% Rhodium wire, with a length to diameter ratio of $l_w/d_w = 180$.

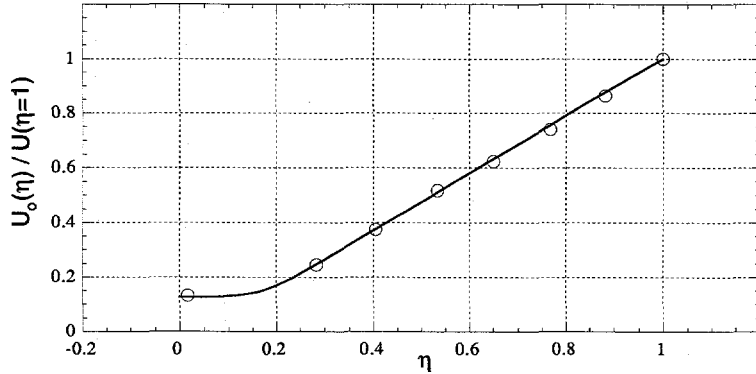


Figure 8.4: Flow acceleration, calculated from the measured wall pressure (\circ), From continuity (solid line).

8.4 Results

8.4.1 Mean velocity

The mean velocity vector reduces to $\mathbf{U} = [U_x(r, x), U_r(r, x), 0]$. Due to homogeneity in the circumferential direction, the mean strain tensor reads:

$$S_{ij} = \begin{pmatrix} 2\partial U_x / \partial x & \partial U_x / \partial r + \partial U_r / \partial x & 0 \\ \partial U_r / \partial x + \partial U_x / \partial r & 2\partial U_r / \partial r & 0 \\ 0 & 0 & 0 \end{pmatrix}, \quad (8.2)$$

and the continuity equation reads:

$$\frac{\partial U_x(x, r)}{\partial x} = - \left(\frac{\partial U_r(x, r)}{\partial r} + \frac{U_r(x, r)}{r} \right) \quad (8.3)$$

The average streamwise strain may then be expressed as

$$\frac{1}{R} \int_o^R \frac{\partial U_x(r, x)}{\partial x} dr = - \frac{1}{R} \int_o^R \left(\frac{\partial U_r(r, x)}{\partial r} + \frac{U_r(r, x)}{r} \right) dr \quad (8.4)$$

The mean streamwise velocity is presented in Fig. 8.5. At the contraction exit, the mean radial velocity, not presented here, increased from approximately zero value on the centre line to 3.5% of the streamwise velocity near the wall. This corresponds to a streamwise flow angle of $\alpha = 2.0^\circ$ in the wall

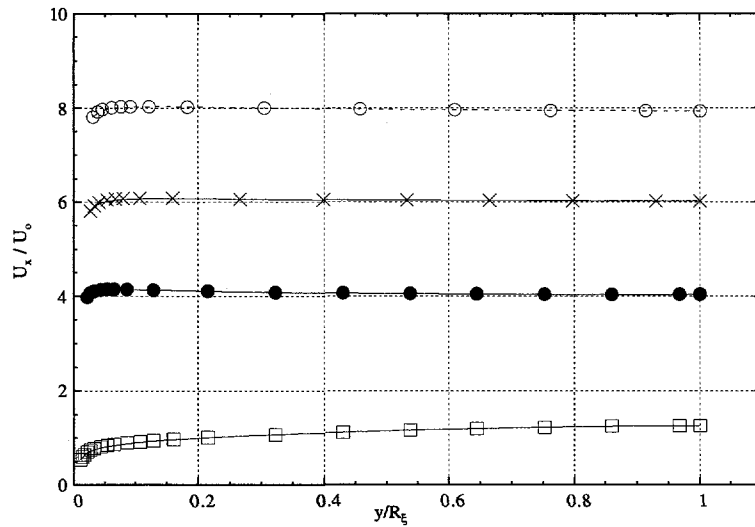


Figure 8.5: Mean streamwise velocity at different locations in the contraction: $\xi = 1$ (\square), $\xi = 4$ (\bullet), $\xi = 6$ (\times), $\xi = 8$ (\circ).

region. For comparison, the angle of the wall at this position is $\alpha = 1.7^\circ$. At $\xi = 8$ the measured mean velocity U_θ was below 0.5% of U_x in the range $0.06 < y/R < 1$. Measurement of the circumferential velocity is sensitive to radial variations of the streamwise velocity, due to the separation of the two hot-wires. If the two wires do not experience the same mean streamwise velocity, this will cause a fictive non-zero circumferential velocity. This phenomenon is obvious close to the wall where U_θ obtains high negative values. In the very near wall region this error was almost eliminated, when correcting for the radial gradient of the streamwise mean velocity. Thus the mean circumferential velocity was found negligible.

8.4.2 Second order moments

Figure 8.6 shows the measured normal stresses, $\overline{u_i^2}$, as function of the distance from the wall, scaled with the pipe bulk velocity (U_o). The wall coordinate is normalized with the local radius (R_ξ). This indicates the total change from one position to the next. The results are presented on a logarithmic scale on both axes, to properly display the variations. The streamwise compo-

ment is very quickly affected by the acceleration, from being the dominant stress at $\xi = 1$, to becoming the smallest in the outer region at $\xi = 4$, where it has been reduced by almost an order of magnitude. Significant streamwise fluctuations are restricted to the region very near the wall. The core region is quickly dominated by the two cross-stream fluctuations, which have become approximately equal. Figure 8.7 shows the total turbulent kinetic energy, $2k = [\overline{u_x^2} + \overline{u_r^2} + \overline{u_\theta^2}]$, which from $\xi = 1$ to $\xi = 4$ has changed only marginally outside the wall layer. This indicates that the loss of energy in the streamwise component has been compensated by a gain in the two cross-stream components. The shear stress, shown in Fig. 8.8, is virtually unaffected in the core region up to $\xi = 6$. Thus the correlation is conserved, despite the strong redistribution of the velocity components. With further contraction to $\xi = 8$, $\overline{u_x^2}$ continues to decrease in the core region, though at a lower rate, and increases in the near wall region, as the production rate here increases downstream. The increase in total kinetic energy downstream indicates that the two cross-stream components increase more than the attenuation of the streamwise component. The core region develops towards a situation of strong anisotropy, where the cross-stream components are dominant and approximately equal. At $\xi = 8$ the shear stress is considerably reduced for $y/R_\xi > 0.1$, compared to the other stations. This indicates a sudden loss in correlation between u_x and u_r .

In context of e.g. wind tunnel contractions, one of the main design parameters is the turbulence intensity. Figure 8.9 shows the local turbulence intensity along the contraction centre line, estimated from the streamwise normal stress: $Tu_x = (\overline{u_x^2})^{1/2}/U_x \times 100\%$ and from all three normal stresses: $Tu_k = (\overline{u_i u_i}/3)^{1/2}/U_x \times 100\%$. In fully developed pipe flow, these two methods differ only marginally. However as the flow accelerates, Tu_x becomes a naive measure of the turbulence level. At $\xi = 8$, $Tu_k \simeq 6 \times Tu_x$. A reliable estimate of the turbulence intensity should therefore be based on the total kinetic energy, and not only the streamwise stress. For the present flow geometry the values of Tu_k is reduced from $\xi = 1$ to $\xi = 6$, but increases with further contraction. This increase is due to secondary production term, as argued for the increase in turbulent kinetic energy. Figure 8.10 shows the the normal stress and turbulent kinetic energy, normalized with the corresponding entrance value, along the contraction centre line. The results indicate that the kinetic energy remain almost constant in the initial stage of the contraction, but then increases with further acceleration. At $\xi = 6$ the kinetic energy is up by 50%, and at $\xi = 8$, the kinetic energy is approximately

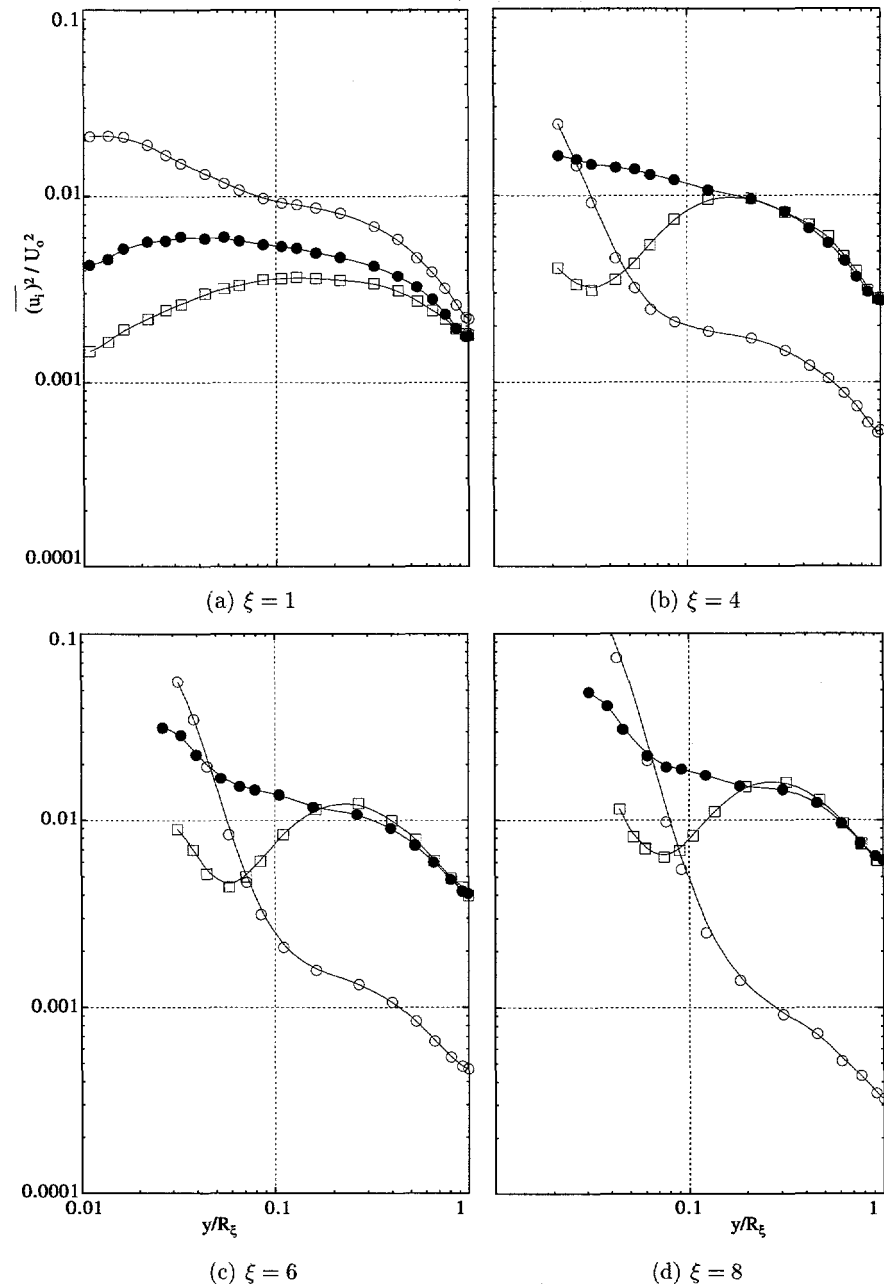


Figure 8.6: Normal stresses : $\overline{u_x^2}$ (\circ) ; $\overline{u_r^2}$ (\square) ; $\overline{u_\theta^2}$ (\bullet).

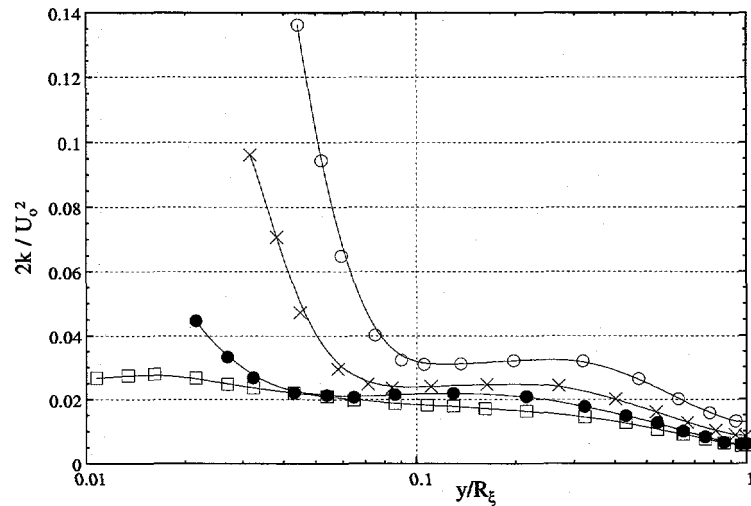


Figure 8.7: Turbulent kinetic energy; $2k/U_o^2$; $\xi = 1$ (\square); $\xi = 4$ (\bullet); $\xi = 6$ (\times); $\xi = 8$ (\circ).

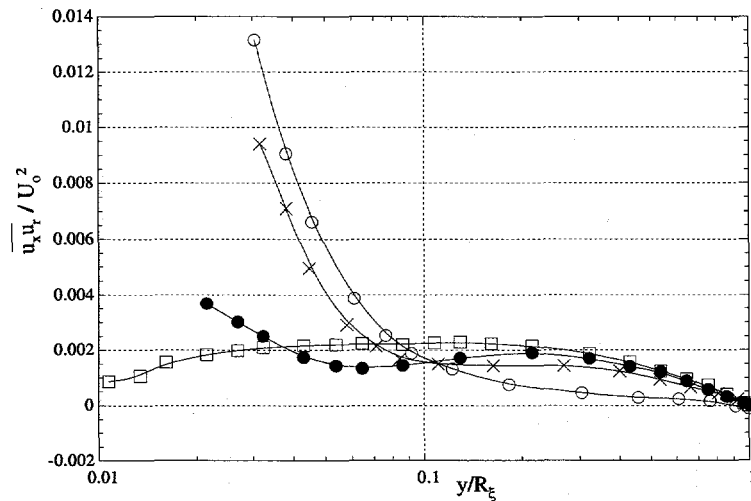


Figure 8.8: Turbulent shear stress; $\bar{u}_x \bar{u}_r / U_o^2$; $\xi = 1$ (\square); $\xi = 4$ (\bullet) ; $\xi = 6$ (\times); $\xi = 8$ (\circ).

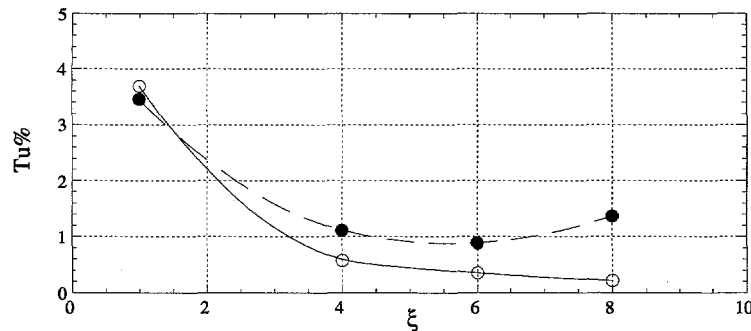


Figure 8.9: Turbulence intensity along the contraction centre line; $Tu_x = (\overline{u_x^2})^{1/2} / U_x \cdot 100\%$ (\circ), $Tu_k = (\overline{u_i u_i} / 3)^{1/2} / U_x \cdot 100\%$ (\bullet).

twice the value of the incoming flow. These results support the findings of Hussain and Ramjee [27]. They obtained $k(\xi = 6)/k(\xi = 1) \simeq 1.5$ and $k(\xi = 8)/k(\xi = 1) \simeq 2.0$, independent of the contraction shape. The relative increase in the lateral intensity, and reduction of the streamwise component also supports the findings of Hussain and Ramjee. Figure 8.11 shows the quadrant decomposition of the shear stress signal $u_x u_r$ for $\xi = 1, 4, 6$ and 8 (The method was described in Chapter 7). The wall coordinate has been scaled with the local radius (R_ξ), and the shear stress has been scaled with the pipe bulk velocity (U_o), such that a summation of all four quadrants relates directly to Fig. 8.8. For fully developed pipe flow ($\xi = 1$), the shear stress is always dominated by the second and fourth quadrant. In the later stage of the contraction the contribution to the shear stress from the inward and outward interactions is of the same magnitude as from the ejections and sweeps. This suggests that strong events originating from one side of the cross section, persist into the opposite half more extensively than for the fully developed pipe flow. This causes a core region of almost absent shear stress, as indicated in Fig. 8.8. When approaching the wall a narrow shear layer appears, which is dominated by events in the second quadrant (ejections).

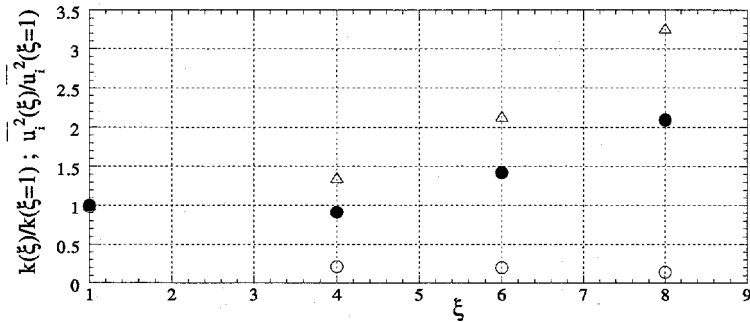


Figure 8.10: Variation in relative streamwise and lateral normal stresses along the contraction centre line, compared to the variation in turbulent kinetic. $k(\xi)/k(\xi = 1)$ (●), $\overline{u_x^2}(\xi)/\overline{u_x^2}(\xi = 1)$ (○), $\overline{u_r^2}(\xi)/\overline{u_r^2}(\xi = 1)$ (△)

8.5 Turbulence Production

To explain the redistribution of energy, it should be appropriate to examine some of the terms in the Reynolds stress transport equations for the individual components, introduced in Chapter 3. The production terms for $\overline{u_x^2}$ are:

$$P_{xx} = -\frac{\partial U_x}{\partial r} \overline{u_r u_x} - \frac{\partial U_x}{\partial x} \overline{u_x^2} \quad (8.5)$$

The first term on the right hand side is everywhere positive and increases the amount of $\overline{u_x^2}$. This term will always be dominant in the near wall region, with presence of turbulent shear stress and a strong mean velocity gradient. The second term is negative and will tend to suppress $\overline{u_x^2}$. This term is believed to be partly responsible for the abrupt reduction in the streamwise component. On the pipe centre line the first term vanishes by definition, and only the negative production term will be present.

For $\overline{u_r^2}$ the turbulence production reads:

$$P_{rr} = -\frac{\partial U_r}{\partial r} \overline{u_r^2} - \frac{\partial U_r}{\partial x} \overline{u_r u_x} \quad (8.6)$$

The first term on the right hand side, which is caused by a non-zero gradient of the wall normal mean velocity, becomes one of the main contributors to the increase in turbulent kinetic energy. This term is always positive and

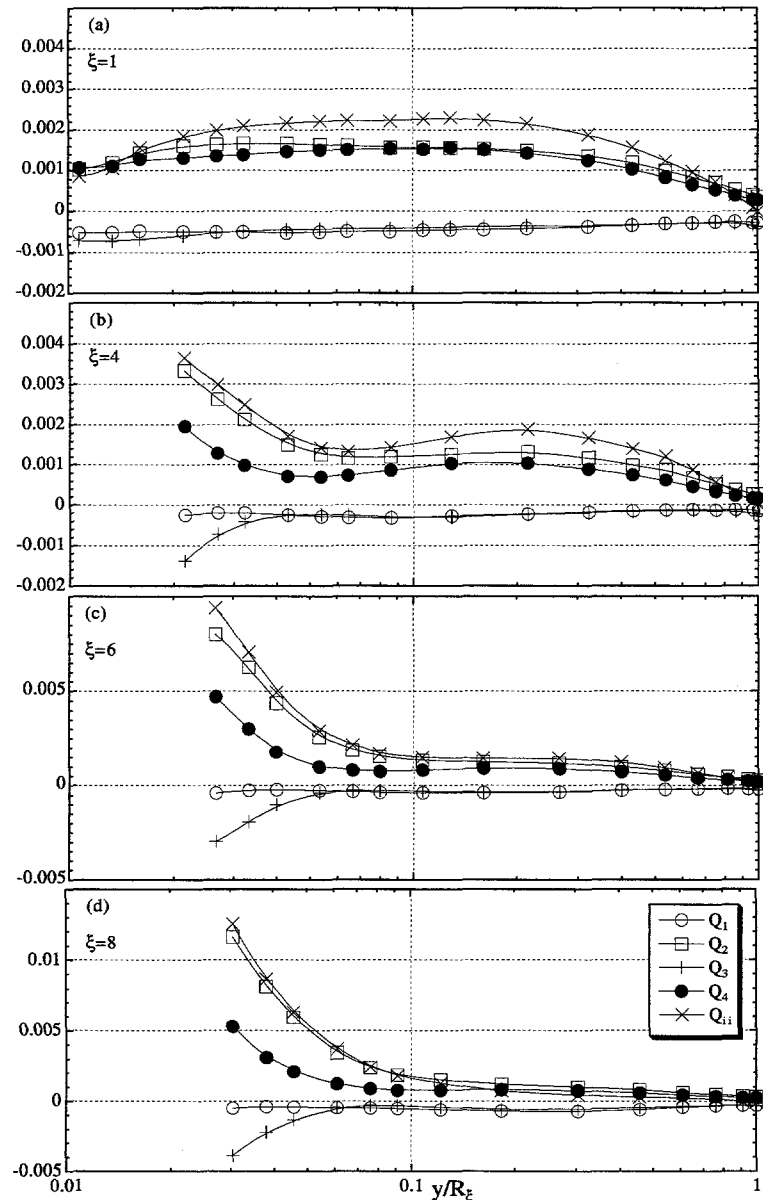


Figure 8.11: Quadrant decomposition of the shear stress signal: $Q_n = \overline{u_x u_r}|_n / U_o^2$.

proportional to \bar{u}_r^2 itself. The last term is small away from the wall, due to the vanishing shear stress, and the fact that U_r tend towards zero at the centre line. Note that the radial derivative of U_r can still be non-zero on the centre line. Hence there is production of \bar{u}_r^2 also on the centre line.

The only direct production term for \bar{u}_θ^2 takes the simple form:

$$P_{\theta\theta} = -\frac{U_r}{r}\bar{u}_\theta^2 \quad (8.7)$$

Since U_r is everywhere negative, this term is positive and contributes to a positive input of energy. A series expansion of U_r near the symmetry line yields that $\frac{U_r(r)}{r} \rightarrow \frac{\partial U_r}{\partial r}$, such that $P_{\theta\theta} \rightarrow P_{rr}$. On the centre line of the fully developed pipe flow, the Reynolds stresses are axisymmetric and near isotropic, which implies $P_{xx} = -2P_{\theta\theta} = -2P_{rr}$, such that the total production is zero. This is reflected in the very small change in total kinetic energy between $\xi = 1$ and $\xi = 4$. As \bar{u}_x^2 vanishes, the total turbulence production is everywhere positive, which also causes the increase in kinetic energy in the later part of the contraction.

The total production of turbulent kinetic energy reads:

$$\begin{aligned} P_k &= -\left(\frac{\partial U_x}{\partial r} + \frac{\partial U_r}{\partial x}\right)\bar{u}_r\bar{u}_x \\ &+ \left(\frac{\partial U_r}{\partial r} + \frac{U_r}{r}\right)\bar{u}_x^2 - \frac{\partial U_r}{\partial r}\bar{u}_r^2 - \frac{U_r}{r}\bar{u}_\theta^2 \end{aligned} \quad (8.8)$$

The production terms obviously favour the two cross-stream components, and will tend to suppress the streamwise component. It is clear however that this is not a sufficient explanation for the changes among the components. It appears plausible to claim that the effect of the dissipation rate, diffusion and advection are of minor importance in this context. Since the dissipative scales are believed to be near isotropic, it is not likely that this should cause large scale anisotropy. When integrating the transport equations with respect to r , the radial diffusion and advection must vanish. The centre line streamwise diffusion in the equation for \bar{u}_r^2 and \bar{u}_θ^2 are found to be small compared to the production terms. The only remaining term, which has the capability of redistributing energy, is then the pressure-strain term. It is commonly stated that the pressure strain has the property of making turbulence more isotropic, suggesting that the energy flow is always directed towards the least energetic components. This means that, for the latter part

of the contraction, the pressure-strain terms should cause an energy transfer from the two cross-stream components to the streamwise component. However, as we have shown, this increase in $\overline{u_x^2}$ will be suppressed by the negative production caused by the last term in Eq.8.5.

8.6 Dissipation Rate

The isotropic approximation to the dissipation rate is normally based on the streamwise dissipation spectrum, such that

$$\varepsilon_{iso} = 15\nu \int_0^\infty D_{xx}(k_x)dk_x = 15\nu \int_0^\infty k_x^2 E_{xx}(k_x)dk_x \quad (8.9)$$

It is clear however that if the streamwise dissipation spectrum is small compared to the cross-stream spectrum, this must be a poor approximation. In the present experiment, the straining process reduces the streamwise spectrum, though mainly at larger scales. However it is difficult to argue for isotropy in the dissipative scales when the large scale turbulence is near two-dimensional. The turbulent Reynolds number is definitely too low for existence of an inertial subrange, which makes it meaningless to extract the dissipation rate from this. A possible improvement may be achieved by using the alternative formulation of Ould-Rouis [47], described in Chapter 3, however this only applies to the centre line location. Results are therefore not included for the dissipation rate, since its accuracy can not be properly documented.

8.7 Turbulence Spectra

The Reynolds stresses are mainly dominated by the large energy containing scales, and to less extent reflect changes in the smaller scales. It should therefore be of interest to examine the turbulence spectra, to determine which scales are affected by the flow acceleration inside the contraction.

In section 8.5 it was shown that the turbulence production, which mainly affects the large scales, played an important role in changing the Reynolds stress tensor. Lindborg [38] stated that redistribution of energy, due to pressure strain interaction, was also dominated by the large scales. This statement is supported by the presence of an inertial range in the one-dimensional

power spectra, where non-zero pressure strain would violate the second hypothesis of Kolmogorov. From these arguments, the large scales are expected to be more affected by the straining than the smaller scales.

Figure 8.12 shows the power spectra, located on the axis of symmetry, for $\xi = 4, 6$, and 8 . The spectra are scaled with the pipe bulk velocity (U_o) and the local radius (R_ξ), and the area under the curve represents $\overline{u_i^2}/U_o^2$, such that

$$\int_0^\infty (R_\xi k_x) \frac{\phi_{ij}(R_\xi k_x)}{U_o^2} d[\ln(R_\xi k_x)] = \frac{\overline{u_i^2}}{U_o^2}. \quad (8.10)$$

The radial and the circumferential spectra should be identical, due to the centre line location, which is seen to compare well with the measured spectra. From $\xi = 4$ to $\xi = 8$, the flow develops in the region of constant strain. Figure 8.13 shows the same streamwise spectra as Fig. 8.12, plotted with an expanded scale. The streamwise spectrum remains virtually unchanged, at least within the spectral scatter. The main differences occur in the two lateral spectra. Figure 8.14 shows the radial spectra only, which more clearly indicates the shift in the most energetic scales, towards lower non-dimensional wave numbers. This suggests that the relative size of the energetic eddies compared to the local radius (R_ξ) increase as the flow accelerates.

The streamwise and radial power spectra are presented in Fig. 8.15 for the centre line at contraction rates $\xi = 4$ and 8 . Note that the spectra are shifted two decades for $\xi = 4$ and four decades for $\xi = 8$, and have been scaled with the pipe diameter (D), not to be confused with the local diameter, and the bulk velocity (U_o). The spectra are compared to the fully developed pipe flow, and relate to the normal stresses as:

$$\int_o^\infty \frac{\Phi_{ii}(Dk_x)}{U_o^2} d(Dk_x) = \frac{\overline{u_i^2}}{U_o^2}, \quad (8.11)$$

(no summation over repeated indices). Thus the spectra represent the total normalized energy distribution. For comparison at the high wave number range, the isotropic spectrum

$$E_{rr}^o(k_x) = \frac{1}{2} \left[E_{xx}(k_x) - k_x \frac{\partial E_{xx}(k_x)}{\partial k_x} \right] \rightarrow \Phi_{rr}^o(Dk_x) \quad (8.12)$$

is included. In fully developed pipe flow the energy containing scales are dominated by the streamwise fluctuations, but the radial spectra intercept

the streamwise spectrum at $Dk_x \simeq 10$, and remain dominant in the high wave number range. This is consistent with the hypothesis of local isotropy. Due to the low Reynolds number, no pronounced inertial range is present. At $\xi = 4$, a severe large scale reduction in $E_{xx}(k_x)$ has occurred, while the small scales are related in a similar way as in the fully developed pipe flow. The radial spectrum is larger than the streamwise spectrum for all wave numbers. If the interaction between eddies of same size is local in wave number space, this suggests that the large scale straining should have a decreasing influence with increasing wave number. This is supported by the present results, where the small scales are less affected by the straining, than the large scale events. Contracting further to $\xi = 8$ contributes mainly to an increase in the cross-stream spectra at large scales. Only minor changes are observed in the streamwise spectrum for the smallest scales.

8.8 Invariants

The invariant analysis of Lumley [42], described in Chapter 6, is applied to the Reynolds stress tensor for the three locations inside the contraction. Figure 8.16 shows the three diagonal elements of the Reynolds stress anisotropy tensor (b_{ij}), along the axis of symmetry, where the off-diagonal elements of b_{ij} are zero. The first point ($\xi = 1$), represents the fully developed pipe flow entering the contraction. At this stage the streamwise component is the dominant one. When exposed to the streamwise acceleration, this situation changes quickly. At $\xi = 4$, the streamwise component is significantly suppressed, in favour of the two lateral components. Comte-Bellot and Corrsin [18] reported that for grid-generated turbulence a contraction rate of $\xi = 1.27$ was needed to generate an intersection of b_{xx} and $b_{rr} = b_{\theta\theta}$. The present results clearly pictures the sensitivity of the Reynolds stress tensor to streamwise strain. With further contraction to $\xi = 6$ and $\xi = 8$, the elements of b_{ij} tend monotonously towards a state of two-component-axisymmetric turbulence. At $\xi = 8$, the streamwise anisotropy equals $b_{xx} = -0.30$, corresponding to 90% of the limit of the two-component state. The Reynolds stress anisotropy invariant map (AIM) is shown in Fig. 8.17 for the same centre line locations as in Fig. 8.16. Again, $\xi = 1$, represents fully developed pipe flow, which is close to but not truly isotropic. Note that the fully developed flow is located on the right axisymmetric line of the AIM. The locations inside the contraction closely follows the left axisymmetric line, de-

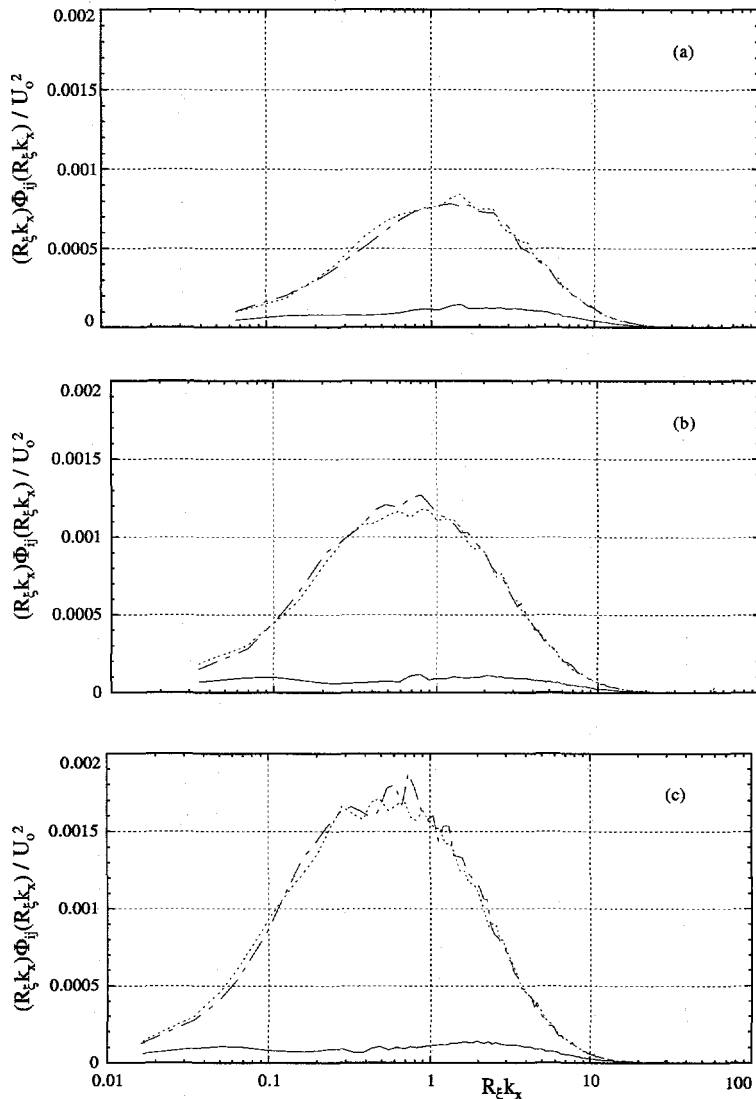


Figure 8.12: Power spectra, $(R_\xi k_x) \Phi_{ij}(R_\xi k_x) / U_o^2$ along the contraction centre line. Streamwise (solid), radial (dotted), circumferential (dashed-dotted) for $\xi = 4$ (a), $\xi = 6$ (b), $\xi = 8$ (c). The area under each curve represents each normal stress component, \bar{u}_i^2 / U_o^2 .

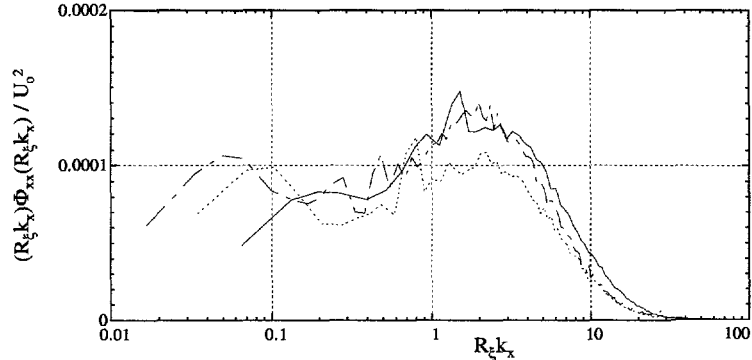


Figure 8.13: Streamwise power spectra, $(R_\xi k_x)\Phi_{xx}(R_\xi k_x)/U_o^2$ along the contraction centre line (same as Fig 8.12 with expanded scale). $\xi = 4$ (solid), $\xi = 6$ (dotted), $\xi = 8$ (dashed-dotted). The area under each curve represents the normal stress component, \bar{u}_x^2/U_o^2 .

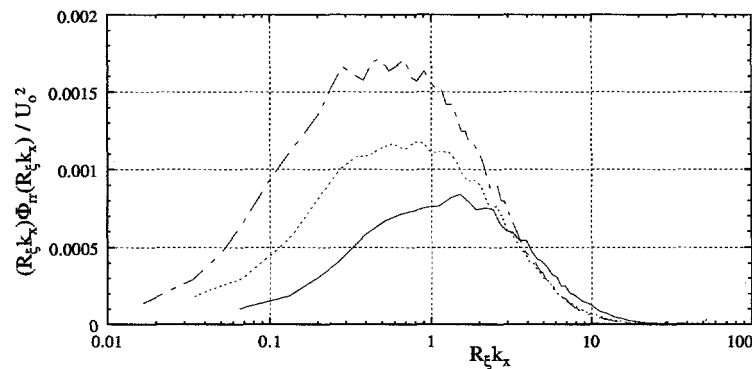


Figure 8.14: Radial power spectra, $(R_\xi k_x)\Phi_{rr}(R_\xi k_x)/U_o^2$ along the contraction centre line. $\xi = 4$ (solid), $\xi = 6$ (dashed), $\xi = 8$ (dashed-dot). The area under each curve represents the normal stress component, \bar{u}_r^2/U_o^2 .

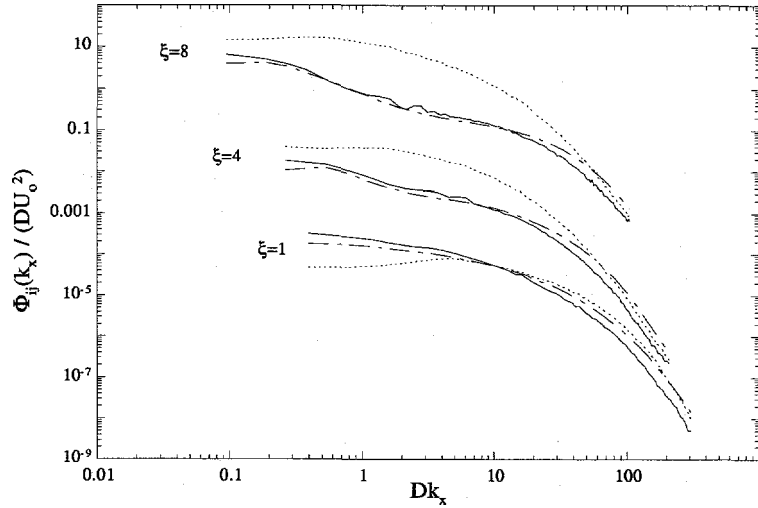
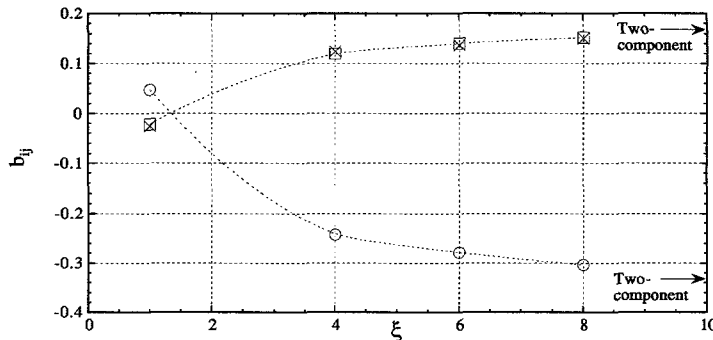
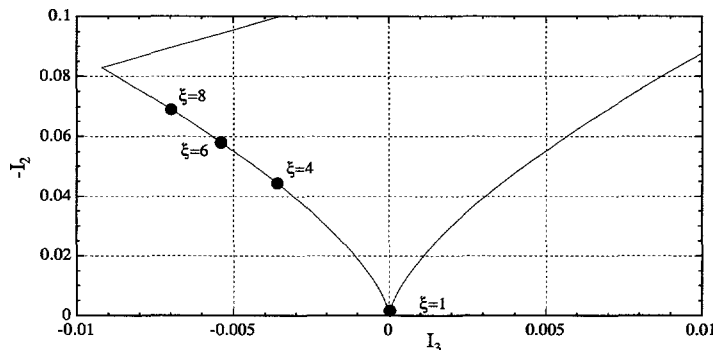
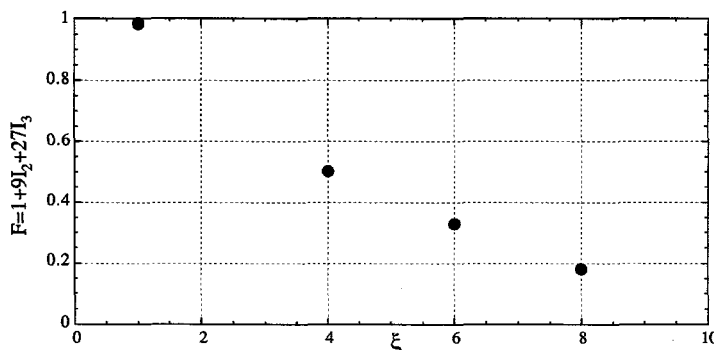


Figure 8.15: Turbulence spectra; centre line; $\Phi_{xx}(Dk_x)$ (solid) ; $\Phi_{rr}(Dk_x)$ (dashed); $\Phi_{rr}^o(Dk_x)$ (dashed-dot). Note that the spectra have been shifted vertically two decades for $\xi = 4$ and four decades for $\xi = 8$.

scribed by Lee and Reynolds [37] as “rod-like” turbulence. The turbulence structure is almost entirely dominated by the two cross-stream components. The trend towards a state of two-component axisymmetric turbulence (upper left corner) is quite clear. However, since turbulence is three-dimensional in its nature, it is difficult to picture an absolute two-component-axisymmetric state. In Chapter 6 it was shown that the near wall DNS data of Kim et al. [32] applied so to say exactly to the two-component state. This result is easy to accept, since the wall normal component is physically restricted by the wall. For the present flow situation in the core region, the relation between the Reynolds stresses are determined by the flow itself, and not by any physical restriction. As described in the discussion of the production terms, the streamwise component is forced to stay small in the core region. Since the suppression (negative production) of the streamwise component is proportional to \bar{u}_x^2 itself, the suppression decreases as \bar{u}_x^2 decreases. Still as the anisotropy increases, interaction of pressure strain is expected to increase in favour of the streamwise component. It is therefore plausible to argue that some sort of balance will be established, preventing the streamwise

Figure 8.16: Elements of the anisotropy tensor b_{ij} ; b_{xx} (\circ); b_{rr} (\times); $b_{\theta\theta}$ (\blacksquare).Figure 8.17: Anisotropy invariant map, (I_2, I_3) , along the contraction centre line.Figure 8.18: Anisotropy function, $F = 9I_2 + 27I_3 + 1$, along the contraction centre line.

component to disappear entirely. This suggests that the two-component-axisymmetric state is less likely to occur than the near wall two-component state. Figure 8.18 shows the anisotropy function $F = 9I_2 + 27I_3 + 1$, indicating the tendency from near isotropic turbulence ($F=1$) at $\xi = 1$, towards near two-component-axisymmetric turbulence ($F=0$ and $A=-1$) at $\xi = 8$.

8.9 Spectral Axisymmetry

Figure 8.19 shows the elements of the spectral anisotropy tensor $c_{ij}(k_x)$, introduced in Chapter 6, at $\xi = 8$ for $y/R_\xi = 1.0$ and 0.18 . The spectra have been multiplied with the wave number, such that the area under each curve relates to the corresponding elements of the Reynolds stress anisotropy tensor b_{ij} . For the centre line $c_{ij}(k_x)$ satisfies the criteria of axisymmetry for all wave numbers. This result is equivalent to the results obtained on the centre line of the fully developed pipe flow. Note that in contradiction to the fully developed pipe flow, the streamwise element $c_{xx}(k_x)$ is everywhere negative, and the two lateral elements are positive and equal. This suggests that all scales are dominated by the lateral fluctuations. In other words, the large scale axisymmetric characteristics is preserved into the smaller scales.

The second location ($y/R_\xi = 0.18$) is chosen on basis of the Reynolds stress tensor, since at this point the two lateral normal stresses are equal (see Fig. 8.6(d)), and therefore indicate axisymmetry. It was of interest to examine the spectral behaviour, to see if only the dominating scales controlling the Reynolds stresses were axisymmetric. Figure 8.19 (b) reflects that $b_{rr} \simeq b_{\theta\theta}$, since the area under the two lateral anisotropy spectra is near identical. However these two do not collapse, which means that local (in scale) axisymmetry is not present. Local axisymmetry also requires that $c_{xr}(k_x)$ is zero. At $y/R_\xi = 0.18$ this is not completely fulfilled, even if $c_{xr}(k_x)$ is small compared to the diagonal elements of $c_{ij}(k_x)$. Figure 8.19 (c) shows the anisotropy spectra at $y/R_\xi = 0.06$, which is sufficiently close to the wall for the streamwise normal stress to become the largest one. The circumferential anisotropy is negative at intermediate scales, but still positive at large scales. The streamwise anisotropy has now switched to the positive side, except for the largest scales. The result clearly pictures how the radial component is suppressed at all scales, when approaching the wall. At this location also the off-diagonal element $c_{xr}(k_x)$ obtains significant values.

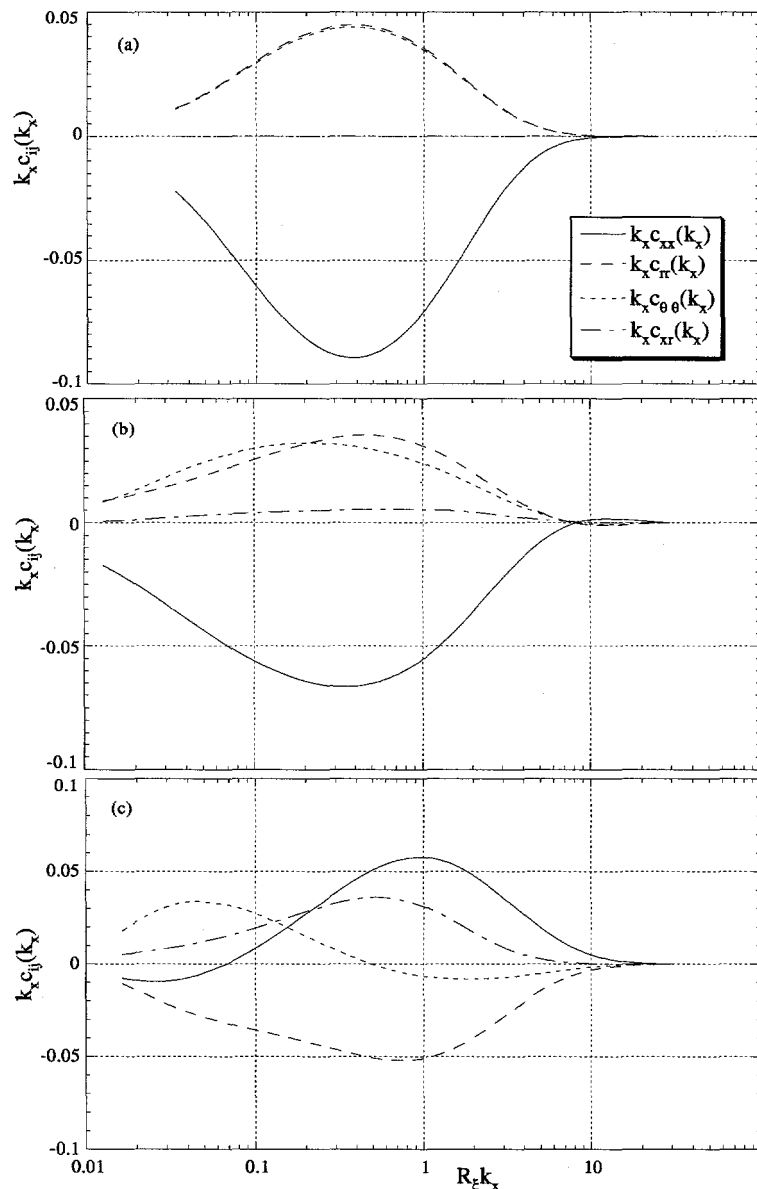


Figure 8.19: Elements of spectral anisotropy tensor at $\xi = 8$: $y/R_\xi = 1.0$ (a), $y/R_\xi = 0.18$ (b), $y/R_\xi = 0.06$ (c).

8.10 Implications on turbulence modelling

In the previous sections it was stated that the streamwise component ($\overline{u_x^2}$) in the contraction core region was mainly controlled by a balance between production and pressure strain. On the symmetry axis the streamwise production is bound to be negative or zero. If an isotropic turbulence model is applied to the problem, all secondary production terms vanish. This clearly indicates the restrictions of e.g. a standard $k-\varepsilon$ turbulence model, since the total production will be strongly underestimated.

In context of Reynolds stress closures, the pressure strain is normally divided into a "slow" and a "rapid" term [6], such that,

$$\Pi_{ij} = \Pi_{ij}^s + \Pi_{ij}^r \quad (8.13)$$

The "slow" term is normally described by the linear return to isotropy model of Rotta [51], which takes the simple form:

$$\Pi_{ij}^s = -C_1 \varepsilon a_{ij} \quad (8.14)$$

where ε is the dissipation rate, and $a_{ij} = \frac{\overline{u_i u_j}}{k} - \frac{2}{3} \delta_{ij}$ is the Reynolds stress anisotropy tensor. The Rotta constant has been found to increase with increasing turbulent Reynolds number. A value of $C_1 = 1.8$ is commonly accepted (see Sjögren [55]). Since the trace of a_{ij} is zero, the trace of Π_{ij}^s must also be zero. Since the least energetic components always has negative value of a_{ij} , the redistribution is always directed from the most energetic to the least energetic component. The rapid term is commonly modelled in terms of the production anisotropy:

$$\Pi_{ij}^r = -C_2 (P_{ij} - \frac{1}{3} \delta_{ij} P_{kk}) \quad (8.15)$$

Sjögren [55] reported experimental results for both the "slow" and the "rapid" pressure strain, obtained in an axisymmetric wind tunnel contraction. The pressure strain was calculated from multiple-point time-space measurements, using the method of Lindborg [38] for axisymmetric turbulence. In the early stage of the contraction the "rapid" term was found to be dominant, though in the latter part the "slow" term was the most important. Sjögren attributed these observations to the triple correlations, which needed more time to develop compared to the second order moments. For the present results it is plausible to argue a similar effect, assuming that the "slow" and the "rapid"

terms may be properly described by the suggested models. The flow entering the contraction has been shown to be close to but not truly isotropic. This implies that the contribution from Π_{ij} should be small, whereas in the latter part of the contraction, the streamwise element of a_{ij} approaches the two-component limit, causing a large degree of anisotropy. The negative production, which occurs in the streamwise direction, is at its peak in the early stage of the contraction, where $\bar{u_x^2}$ is still significant. This causes a wider separation of the elements of the production anisotropy tensor, which is in favour of the "rapid" term.

8.11 Conclusions

A rapid redistribution of energy between the normal components was found as the flow accelerated. In the initial stage of the contraction, the level of turbulent kinetic energy remained constant in the core region, which is caused by a negative production term in the streamwise direction, closely balanced by a corresponding positive production term for the cross-stream components. In the downstream part of the contraction, the streamwise component almost vanished in the bulk part of the cross section, and the total production was everywhere positive. This resulted in a gradual increase in the turbulent kinetic energy. The relative variation in the turbulent kinetic energy: $k(\xi)/k(\xi = 1)$ along the contraction centre line was found consistent with results reported by Hussain and Ramjee [27]. The results support that the contraction ratio, rather than the contraction shape determines the relative variation of the Reynolds stresses.

The flow develops towards a situation of two-component-axisymmetric turbulence, dominated by cross-stream fluctuations. The streamwise normal stress is dominant only in a narrow layer near the wall. The rapid changes in the Reynolds normal stresses are believed to be controlled mainly by secondary production and pressure-strain.

By examining the turbulence spectra, the inter-component transfer of energy is found to be restricted to the large energy containing scales. The spectral anisotropy tensor, introduced in Chapter 6, was calculated at three different locations at the contraction exit. On the centre line the anisotropy spectra corresponded to what Lee and Reynolds [37] denoted as "rod-like" axisymmetry. The streamwise anisotropy element $c_{xx}(k_x)$ was negative for all scales, and the two lateral elements $c_{rr}(k_x)$ and $c_{\theta\theta}(k_x)$ were positive and

equal. Closer to the contraction wall ($y/R_\xi = 0.18$) the normal components of the Reynolds stress anisotropy tensor still corresponded to axisymmetry ($b_{rr} = b_{\theta\theta}$). However this axisymmetric behaviour was not completely satisfied at all turbulent scales. The streamwise element $c_{xx}(k_x)$ was negative for all scales, and the two lateral elements were positive but not equal. The off-diagonal element $c_{xr}(k_x)$ was slightly different from zero, which contradicts absolute axisymmetry. In a narrow wall region the streamwise normal stress becomes the larger one. At $y/R_\xi = 0.06$ the streamwise anisotropy becomes positive for almost the entire range of scales, except for the very largest scales. At this location the radial component is suppressed at all scales, due to the presence of the wall.

The results indicate that the core region ($y/R > 0.2$) is strongly affected by the axisymmetric confinement.

Chapter 9

Summary

Detailed time series of the turbulent velocity signal were obtained in two straight pipe sections. The mean velocity distribution and turbulence statistics were shown to correspond to a state of fully developed pipe flow.

From the velocity time series, one-dimensional turbulence wave number spectra were obtained, assuming validity of the Taylor hypothesis. Special interest was paid to the Kolmogorov -5/3 inertial subrange. In the pipe core region a narrow wave number range in the streamwise power spectrum applied to the -5/3 range for $R_\lambda = 112$. However it was shown that this wave number range was influenced by both turbulence production and viscous dissipation. Thus what appeared as an inertial range, contradicted the basic assumptions posed by Kolmogorov. The results indicate how the "crest" in the compensated streamwise power spectrum near the dissipative scales, can be misinterpreted as an inertial range for low and moderate turbulent Reynolds numbers (R_λ).

To further examine the inertial range scaling, the streamwise power spectra were compared with second order longitudinal velocity structure functions. The power spectrum and the structure function are related by a Fourier transform, which gives a direct relation between the corresponding inertial range scaling constants. The ratio of the scaling constants could therefore be calculated from the ratio of the inertial plateau of the spectrum and the structure function. Increasing correspondence between the scaling constants was observed as R_λ increased. The results support the findings of Bowman [9], suggesting that the production scales and dissipative scales must be separated by several decades for the appearance of a "true" inertial range. A disadvantage of fully developed pipe flow in this respect is that it does not

produce high turbulent Reynolds numbers in laboratory scale experiments. However the flow situation was chosen due to the advantage of low turbulence intensity, which makes the application of the Taylor hypothesis very reliable. The results provide important information as to when to expect an inertial range. It should be of interest to obtain similar results for a wider range of R_λ , preferably in low intensity flows. Basically this implies that the geometric scales of the experiment must be large. Increasing amount of results from direct numerical simulations and sub-grid scale modelling has provided new information on space-time resolved turbulence. It is important that the spectral results from numerical simulations are not tuned against false premises.

A method for calculating the one-dimensional spectral anisotropy tensor from the measured one-dimensional turbulence spectra is derived. The method is applied to the spectra obtained in the fully developed pipe flow. The four non-zero elements of the anisotropy tensor is reported. When comparing the circumferential and radial anisotropy spectra a significant difference was observed when moving away from the centre line. The circumferential component approaches isotropy at much larger scales than the radial component. The results suggest that energy is more easily redistributed to the circumferential component than the radial component. This is because the radial component is forced to stay anisotropic in the large scales due to the wall restriction. The present results also indicate that the large scale axisymmetric properties are conserved into the smaller scales.

The final part of this thesis investigated the effects of an axisymmetric contraction of the fully developed pipe flow. It is a well known property of turbulence that a mean flow acceleration reduces the streamwise normal stress in favour of the two lateral components. In the present experiment, the flow was subjected to a constant streamwise acceleration. A rapid redistribution of energy between the three normal components was observed as the flow accelerated. The Reynolds stress tensor developed towards a state of near two-component turbulence, with a core region dominated by lateral fluctuations. Only in a narrow wall region could significant streamwise fluctuation be observed. By examining the turbulence spectra, the inter-component transfer of energy was found to be restricted to the large scales. The redistribution between the normal components is believed to be controlled mainly by secondary production and pressure-strain interaction.

The flow configuration is simple in its geometry, but still offer difficulties in context of turbulence modelling. Due to homogeneity in the circumfer-

tial direction, it is possible to resolve the flow in a 2D numerical simulation. Since the pressure gradient term in the equation for the mean streamwise velocity is dominating, the correct mean velocity field should be relatively easy to achieve. The interesting question is to what extent different second moment closures are able to predict the changes in the Reynolds stress tensor. It would also be of interest to see the performance of sub-grid scale models when it comes to changes in the spectral distributions. The present experiment should therefore serve as a relevant test case in turbulence modelling.

Bibliography

- [1] H.I. Andersson and R. Kristoffersen. Statistics of numerically generated turbulence. *Acta Applicandae Mathematicae*, 26:293–314, 1992.
- [2] F. Anselmet, Y. Gagne, E.J. Hopfinger, and R.A. Antonia. High-order velocity structure functions in turbulent shear flows. *J. Fluid Mech.*, 140:63–89, 1984.
- [3] R.A. Antonia, J. Kim, and L.W.B. Browne. Some characteristics of small-scale turbulence in a turbulent duct flow. *J. Fluid Mech.*, 233:369–388, 1991.
- [4] R.A. Antonia, M. Ould-Rouis, F. Anselmet, and Y. Zhu. Analogy between predictions of Kolmogorov and Yaglom. *J. Fluid Mech.*, 332:395–409, 1997.
- [5] R.A. Antonia, Y. Zhu, and H.S. Shafii. Lateral vorticity measurements in a turbulent wake. *J. Fluid Mech.*, 323:173–200, 1996.
- [6] D. Aronson and L. Löfdal. The plane wake of a cylinder: An estimate of the pressure-strain rate tensor. *Phys. Fluids*, 6:2716–2721, 1994.
- [7] R.S. Azad and S.Z. Kassab. New method of obtaining dissipation. *Exp. in Fluids*, 7:81–87, 1989.
- [8] G.K. Batchelor. The theory of axisymmetric turbulence. *Proc. Roy. Soc.A.*, 186:480–502, 1946.
- [9] J.C. Bowman. On inertial-range scaling laws. *J. Fluid Mech.*, 306:167–181, 1996.
- [10] L.W.B. Browne, R.A. Antonia, and L.P. Chua. Calibration of x-probes for turbulent flow measurements. *Exp. in Fluids*, 7:201–208, 1989.

- [11] L.W.B. Browne, R.A. Antonia, and L.P. Chua. Velocity vector cone angle in turbulent flows. *Exp. in Fluids*, 8:13–16, 1989.
- [12] L.W.B. Browne, R.A. Antonia, and S. Rajagopalan. The spatial derivative of temperature in turbulent flow and Taylor's hypothesis. *Phys. Fluids*, 26:1222–1227, 1983.
- [13] L.W.B. Browne, R.A. Antonia, and D.A. Shah. Selection of wires and wire spacing for x-wires. *Exp. in Fluids*, 6:286–288, 1988.
- [14] L.W.B. Browne and A. Dinkelacker. Turbulent pipe flow: pressures and velocities. *Fluid Dynamics Research*, 15:177–204, 1995.
- [15] F.H. Champagne. The fine-scale structure of the turbulent velocity field. *J. Fluid Mech.*, 86:67–108, 1978.
- [16] S. Chandreskhar. The theory of axisymmetric turbulence. *Philos. Trans.A.*, 242:557–577, 1950.
- [17] J.R. Chasnov. Simulation of the Kolmogorov inertial subrange using an improved subgrid model. *Phys. Fluids*, A3(1):188–199, 1991.
- [18] G. Comte-Bellot and S. Corrsin. The use of a contraction to improve the isotropy of grid-generated turbulence. *J. Fluid Mech.*, 25:657–682, 1966.
- [19] F. Durst, J. Jovanovic, and J. Sender. LDA measurements in the near-wall region of a turbulent pipe flow. *J. Fluid Mech.*, 295:305–335, 1995.
- [20] F. Durst, H. Kikura, I. Lekakis, J. Jovanovic, and Q. Ye. Wall shear stress determination from near-wall mean velocity data in turbulent pipe and channel flows. *Exp. in Fluids*, 20:417–428, 1996.
- [21] J.G.M. Eggels, F. Unger, M.H. Weiss, J. Westerweel, R.J. Adrian, R. Friedrich, and F.T.M. Nieuwstadt. Fully developed turbulent pipe flow: a comparison between direct numerical simulation and experiment. *J. Fluid Mech.*, 268:175–209, 1994.
- [22] A.A. Fontaine and S. Deutsch. Three-component, time-resolved velocity statistics in the wall region of a turbulent pipe flow. *Exp. in Fluids*, 18:168–173, 1995.

- [23] W. Frost and T.H. Moulden. *Handbook of Turbulence*. Plenum Press, New York, 1977.
- [24] W.K. George and H.J. Hussein. Locally axisymmetric turbulence. *J. Fluid Mech.*, 233:1–23, 1991.
- [25] J.O. Hinze. *Turbulence*. MacGraw-Hill series in mechanical engineering, 1975.
- [26] A.K. M.F. Hussain. Coherent structures and turbulence. *J. Fluid Mech.*, 173:303–356, 1986.
- [27] A.K.M.F. Hussain and V. Ramjee. Effects of the axisymmetric contraction shape on incompressible turbulent flow. *J. Fluids Eng.*, 98:58–69, 1976.
- [28] ISO5167. International standard: Measurement of fluid flow by means of pressure differential devices, 1991.
- [29] H. Kahalerras, Y. Malecot, and Y. Gagne. Intermittency and Reynolds number. *Phys. of Fluids.*, 10:910–921, 1998.
- [30] R.I. Karlsson and T.G. Johansson. LDV measurements of higher order moments of velocity fluctuations in a turbulent boundary layer. In *Laser Anemometry in Fluid Mechanics III* (ed. R.J. Adrian et al.), Ladoan-Instituto Superior Tecnico, Lisbon, Portugal, 1989.
- [31] J. Kim and R.A. Antonia. Isotropy of the small scales of turbulence at low Reynolds number. *J. Fluid Mech.*, 251:219–238, 1993.
- [32] J. Kim, P. Mion, and R. Moser. Turbulence statistics in fully developed channel flow at low Reynolds number. *J. Fluid Mech.*, 177:133–166, 1987.
- [33] A. Klein. Review: Turbulent developing pipe flow. *J. Fluid Eng.*, 103:243–249, 1981.
- [34] P.-Å. Krogstad, J.H. Kaspersen, and S. Rimestad. Convection velocities in a turbulent boundary layer. *Phys. Fluids*, 10:949–957, 1998.

- [35] J.C.S. Lai, K.J. Bullock, and P.G. Hollis. Turbulence wavenumber spectra in fully developed smooth pipe flow. *Exp. in Fluids*, 12:369–376, 1992.
- [36] C.J. Lawn. The determination of the rate of dissipation in turbulent pipe flow. *J. Fluid Mech.*, 48:477–505, 1971.
- [37] M.J. Lee and W.C. Reynolds. *Numerical experiments on the structure of homogenous turbulence*, Rep. TF-24. Thermoscientific Division, Stanford University, 1985.
- [38] E. Lindborg. *Studies in classical turbulence theory*. PhD thesis, Royal Institute of Technology, Sweden, 1996.
- [39] S.S. Lu and W.W. Willmarth. Measurement of the structure of the Reynolds stress in a turbulent boundary layer. *J. Fluid Mech.*, 60:481–511, 1973.
- [40] R.M. Lueptow, K.S. Breuer, and J.H. Haritonidis. Computer aided calibration of x-probes using a look-up table. *Exp. in Fluids*, 6:115–118, 1988.
- [41] J.L. Lumley. Interpretation of time spectra measured in high-intensity shear flows. *Phys. Fluids*, 8:1056–1062, 1965.
- [42] J.L. Lumley. Computational modeling of turbulent flows. *Adv. Appl. Mech.*, 18:123–176, 1978.
- [43] N.N. Mansour, J. Kim, and P. Moin. Reynolds-stress and dissipation-rate budgets in a turbulent channel flow. *J. Fluid Mech.*, 194:15–44, 1988.
- [44] S. Mochizuki and F.T.M. Nieuwstadt. Reynolds-number-dependence of the maximum in the streamwise velocity fluctuations in wall turbulence. *Exp. in Fluids*, 21:218–226, 1996.
- [45] J.F. Nash and V.A. Patel. *Three-Dimensional Turbulent Boundary Layers*. SBS Technical Books, Iowa Institute of Hydraulic Research, 1972.
- [46] A. Noullez, G. Wallace, W. Lempert, R.B. Miles, and U. Frisch. Transverse velocity increments in turbulent flow using the relief technique. *J. Fluid Mech.*, 339:287–307, 1997.

- [47] M. Ould-Rouis, R.A. Antonia, Y. Zhu, and F. Anselmet. Relation between third-order and second order velocity structure functions for axisymmetric turbulence. In *11 Turb. Shear Flows, Grenoble*, 1997.
- [48] B.R. Pearson and R.A. Antonia. Velocity structure functions in a turbulent plane jet. In *11 Turb. Shear Flows, Grenoble*, 1997.
- [49] A.E. Perry and C.J. Abell. Asymptotic similarity of turbulence structures in smooth- and rough-walled pipes. *J. Fluid Mech.*, 79:785–799, 1977.
- [50] A. Praskovsky and S. Oncley. Measurements of the Kolmogorov constant and intermittency exponent at very high Reynolds numbers. *Phys. Fluids*, 6:2886–2888, 1994.
- [51] J.C. Rotta. Statistiche theorie nichthomogener turbulenz. *Z. Phys.*, 131, 1951.
- [52] J. Sabot and G. Comte-Bellot. Intermittency of coherent structures in the core region of fully developed turbulent pipe flow. *J. Fluid Mech.*, 74:767–796, 1976.
- [53] S.G. Saddoughi. Local isotropy in complex turbulent boundary layers at high Reynolds number. *J. Fluid Mech.*, 348:201–245, 1997.
- [54] S.G. Saddoughi and S.V. Veeravalli. Local isotropy in turbulent boundary layers at high Reynolds number. *J. Fluid Mech.*, 268:333–372, 1994.
- [55] T. Sjögren. *Development and Validation of Turbulence Models Through Experiment and Computation*. PhD thesis, Royal Institute of Technology, Sweeden, 1997.
- [56] P.E. Skåre. *Experimental investigation of an equilibrium boundary layer in strong adverse pressure gradient*. PhD thesis, Norwegian Institute of Technology, 1994.
- [57] G. Sovran and E. Klomp. Experimentally determined optimum geometries for rectilinear diffusers with rectangular, conical or annular cross section. In *Fluid Mechanics of Internal Flows, Elsiver, Amsterdam*, 1967.

- [58] K.R. Sreenivasan. On the universality of the Kolmogorov constant. *Phys. Fluids*, 7:2778–2784, 1995.
- [59] M. Tagawa, T. Tsuji, and Y. Nagano. Evaluation of x-probe response to wire separation for wall turbulence measurements. *Exp. in Fluids*, 12:413–421, 1992.
- [60] H. Tennekes and J.L. Lumley. *A First Course in Turbulence*. MIT Press, 1971.
- [61] J.M.J. Toonder and F.T.M. Nieuwstadt. Reynolds number effects in a turbulent pipe flow for low to moderate Re. *Phys. Fluids*, 9:3398–3409, 1997.
- [62] L.E. Torbergson and P.-Å. Krogstad. Axisymmetric contraction of fully developed pipe flow. Accepted to *13th Australasian fluid mechanics conference*, Melbourne, Australia, Dec. 1998.
- [63] J. Westerweel, A.A. Draad, J.G.Th. van der Hoeven, and J. van Oord. Measurement of fully-developed turbulent pipe flow with digital particle image velocimetry. *Exp. in Fluids*, 20:165–177, 1996.
- [64] F.M. White. *Fluid Mechanics*. Mc-Graw-Hill, 1994.
- [65] J.C. Wyngaard and S.F. Clifford. Taylor's hypothesis and high-frequency turbulence spectra. *J. of the Atmospheric Sci.*, 34:922–929, 1977.
- [66] P.K. Yeung and G. Brasseur. The response of isotropic turbulence to isotropic and anisotropic forcing at the large scales. *Phys. Fluids*, 5:884–897, 1991.
- [67] M.V. Zagarola, A.E. Perry, and A.J. Smits. Log laws or power laws: The scaling in the overlap region. *Phys. Fluids*, 9:2094–2100, 1997.